AUTOMATED MICROFLUIDIC PLATFORMS FOR HIGH-THROUGHPUT *IN VIVO* FUNCTIONAL IMAGING AND INDIVIDUALIZED LONG-TERM HEALTH AND LONGEVITY TRACKING OF *C. ELEGANS*

A Dissertation
Presented to
The Academic Faculty

by

Yongmin Cho

In Partial Fulfillment
of the Requirements for the Degree
Doctor of Philosophy in the
School of Chemical and Biomolecular Engineering

Georgia Institute of Technology
May 2017

AUTOMATED MICROFLUIDIC PLATFORMS FOR HIGH-THROUGHPUT *IN VIVO* FUNCTIONAL IMAGING AND INDIVIDUALIZED LONG-TERM HEALTH AND LONGEVITY TRACKING OF *C. ELEGANS*

Approved by:

Dr. Hang Lu, Advisor
School of Chemical and Biomolecular Engineering
Georgia Institute of Technology

Dr. Patrick McGrath
School of Biological Sciences
Georgia Institute of Technology

Dr. Victor Breedveld
School of Chemical and Biomolecular Engineering
Georgia Institute of Technology

Dr. QueeLim Ch'ng
Department of Developmental Neurobiology
King's College London

Dr. Mark P. Styczynski
School of Chemical and Biomolecular Engineering
Georgia Institute of Technology

Date Approved: [March 22, 2017]

[To my dad, mom, sister, and life partner]

ACKNOWLEDGEMENTS

I would like to foremost thank my advisor, Dr. Hang Lu, for her advice, mentoring, support, encouragement, and dedication. She always provided valuable guidance throughout my studies. I have truly enjoyed my experience as her graduate student and this work would not have been possible without her support. I would further like to thank my committee members, Dr. Victor Breedveld, Dr. Mark Styczynski, Dr. Patrick McGrath, and Dr. QueeLim Ch'ng, for providing me with constructive feedback and advice to improve this work. Moreover, I express my great gratitude to my collaborator, Dr. William Schafer for his advice and our constant communication.

I wish to thank all my current and past members of the Lu lab. In particular, I make special note of same-year friends, Daniel Porto, Weipeng Zhuo, and Tel Rouse for their intellectual and emotional support. I would like to thank our previous lab member, Dr. Mei Zhan for training me when I join the lab and giving many intellectual inputs to me. Additionally, I would like to thank my undergraduate students, David N. Oakland and Kirby G. Broderick for their help and dedication to my research.

I would also like to express my great gratitude and love to my parents and sister for their support and cheering me on throughout my entire life. Finally, I would like to express my greatest love and gratitude to my fiancée, Sol-Ah Lee, who has given me love and made my life brighter than it could have ever been without her.

TABLE OF CONTENTS

LIST OF TABLES

LIST OF FIGURES

LIST OF SYMBOLS AND ABBREVIATIONS

C. elegans	*Caenorhabditis elegans*
CGC	Caenorhabditis Genetics Center
E. coli	*Escherichia coli*
GFP/RFP	Green/Red Fluorescent Protein
M9	Buffer suitable for washing off *C. elegans* individuals
NGM	Nematode Growth Medium
OP50	Strain of *E. coli* used as feedstock for *C. elegans*
PDMS	Polydimethylsiloxane, used for microfluidic devices

SUMMARY

One of big questions in neuroscience is how animals modulate behavior in response to external stimuli and environmental cues, and how this changes with age. Over the last few decades, many molecules and signaling pathways involved in sensory transduction in the nervous system, as well as a diverse array of genetic and environmental modulators of the aging process have been found to be conserved between humans and many model organisms. Due to its relatively simple nervous system and short lifespan, *Caenorhabditis elegans* is an important model organism for the study of sensory perception and aging. This thesis explores the use of microfluidic techniques in conjunction with automation technology, and its application to the functional neural imaging and longitudinal imaging of *C. elegans*.

Mechanosensation is an important sensory modality, relevant to hearing, touch, and balance in humans and other animals. However, an extensive understanding of how animals encode mechanical stimuli through their nervous system is still lacking. In the first and second aims, I developed a series of automated microfluidic systems for high-throughput *in vivo* functional imaging of *C. elegans* from larvae to adults for the study of mechanotrandsuction. Compared to previously described assay systems, these microsystems greatly improve experimental throughput and operational robustness. As a result of these technological advances, I tested a variety of neuronal responses in mechanosensory circuits to highly-controlled mechanical stimuli across stages of development and various physiological stages, including sleep-like states. I also

demonstrated the ability to perform a drug screen based on neuronal activity and examined sensory integration in interneurons in response to multimodal sensory input.

In the third aim, I developed an automated microfluidic platform for individualized long-term health and longevity tracking and investigation of genetic and environmental effects on aging under highly controlled environmental conditions. With this platform, I monitored both individual longevity and behavioral information of *C. elegans* with sub-hourly experimental time resolution at a variety of temperatures and food levels. Moreover, I developed an automatic behavior analysis algorithm and statistical methods to assess behavior-based healthspan metrics and the relation between environmental, stochastic factors, health, and lifespan. Together, the newly developed microsystems for high-throughput functional imaging and the long-term imaging platform permit the investigation of sensory integration in the nervous system and the large-scale investigation of long-term behavioral and health metrics during the aging process of *C. elegans*.

CHAPTER 1. INTRODUCTION

The term sensory integration refers to the way animals use information provided by the senses. Animal sensation integrates to form a complete understanding of the environment, and this understanding modulates behavior to react to changes. Specifically, mechanosensation is an important sensory modality for interaction with surroundings: it is responsible for hearing in mammals, and diverse mechanoreceptors in our skin transduce pressure to give rise to tactile sensations[1,2]. Although molecular mechanisms for mechanotransduction have been discovered using a variety of model organisms[3-9], the neuronal mechanism underlying mechanosensation is not well understood.

Aging has important consequences for human health and is complex, affected by genetic, environmental, and stochastic factors. Advances in understanding the processes responsible for aging and their consequences might lead to the development of therapies to slow them or mitigate their effects. However, due to the difficulty of controlling environmental and genetic factors in humans, much of our understanding has been discovered from studies in simple model organisms. Many genetic underpinnings of aging and environmental modulators, such as diet and temperature, have been found to be conserved across a diverse group of model organisms[10,11].

To begin to understand how animals sense external mechanical stimulation and how genetic and environmental factors interact in aging process, a model organism is required. This organism must sense mechanical stimulation, and its lifespan must be significantly affected by genetic and environmental factors. In particular, the nematode *Caenorhabditis elegans* serves as a convenient multicellular model for the study of mechanosensation and

aging. First, its ease of culture and amenability to many genetic and genomic tools, including a vast collection of mutants, reverse genetic tools like RNAi, and genome editing tools like CRISPR, permit a high degree of control over both environmental and genetic factors[12]. Second, it has been used to discover several genes, including mechano-electrical transduction channels formed via DEG/ENaC or TRP channel proteins[1,3-9,13,14]. Third, its optical transparency permits noninvasive *in vivo* functional neural imaging via genetically encoded calcium indictors such as GCaMP[15,16]. Lastly, it is the first model system to have its entire neuronal connectome mapped out[17].

Yet, despite the many advantages of *C. elegans*, its millimeter body size is not compatible with many existing commercial toolsets and poses experimental challenges such as difficult handling and manipulation. This requires the development of new platforms to serve some of the same experimental functions. The work presented here is aimed to advance a systemic perspective of mechanotransduction and the aging process by providing experimental tools for monitoring neuronal responses to controlled external stimulation and dissecting the connection between environmental input, long-term health metrics, and longevity. To address previously stated experimental challenges, I utilize existing microfluidic technology for precise control over animals, stimulus delivery, and environmental regulation, as well as computer-aided automation for high-throughput data collection and processing.

This work demonstrates the application of a collection of microfluidic devices for high-throughput functional neural imaging to mechanical stimulation. In addition, this thesis shows the validation of an integrated microsystem for long-term imaging of individual worms with highly controlled environmental conditions. The following sections

serve as a brief review of prior research on mechanosensation and aging in *C. elegans*, present the limitations of previous methods of investigation, and introduce the objectives of this work.

1.1 *C. elegans* as a model organism

C. elegans is a good model organism because of its ease of handling, short reproductive cycle, and small transparent body. The first two properties allow for shorter experimental protocols with higher sample sizes, while optical transparency allows for straightforward *in vivo* imaging of features that would otherwise require dissection. *C. elegans* has exactly 302 neurons, the anatomy and development of which are stereotyped from the zygote to mature adult, and it has therefore served as a valuable model for researchers seeking a detailed understanding of the neural circuitry of a simple, familiar organism. This combination of unique experimental properties provided by *C. elegans* allows for the collection of valuable neurological data with sample sizes of dozens or even hundreds of animals involved in most experiments. Another advantage is the ease of genetics, in terms of forward (e.g. mutagenesis) and reverse genetics (RNAi), and direct engineering of mutations or knock-ins (e.g. by CRISPR). All of these techniques have pushed the frontier of a mechanistic understanding of neurobiology.

1.1.1 For the study of mechanotransduction

Mechanosensation involves the transduction of mechanical stimuli to neuronal activity, enabling living organisms to detect these stimuli. In contrast to chemosensation, which is responsible for smell in humans, relatively little is known about the mechanisms underpinning mechanosensation. It is clear, however, that mechanosensation is an important modality for living organisms, and it is conserved between *C. elegans* and humans. Indeed, *C. elegans* has been used to study mechanosensation since the 1970's. For example, when it encounters an object while locomoting, *C. elegans* will modulate its behaviors by reversing or accelerating[18,19]. In addition, several genes connected to mechanosensation have been discovered, including mechano-electrical transduction channels formed via DEG/ENaC or TRP channel proteins, which have strong homology to human genes[1,3-9,13,14]. These advantages lead it to be a good model for the study of mechanosensation and the neuronal circuits that drive behavior.

1.1.2 For the study of longevity and healthspan

Aging is a complex process by which a combination of genetic, environmental, and stochastic factors modify organ or tissue function to ultimately alter physiological processes over an organism's life. *C. elegans* is an important model organism for the investigation of this process, because the longevity of a worm population subjected to different genetic or environmental regulations can be easily assessed over relatively short lifespans. Specifically, studies in several organisms, including *C. elegans*, have identified many genes involved in aging, including an insulin-like signaling pathway that affects

longevity conserved between invertebrates and humans[10,20,21]. Reduction of insulin signaling, for example in *daf-2* loss-of-function mutants, was first found to increase longevity in *C. elegans*[20], but has since been shown to influence lifespan in flies, mice, and humans[10,22]. Environmental factors such as diet and temperature also influence lifespan and aging; dietary restriction extends lifespan in invertebrates and mammals[23], and environmental stress can increase lifespan via hormesis[24]. Additionally, since isogenic populations show lifespan variation and thermal noise can lead to differences in biological outcomes even among genetically identical individuals, stochastic effects in biological processes have also been proposed as lifespan determinants[25].

Although aging studies have found that the evolutionarily conserved genes and signaling pathways could extend lifespans of many organisms[10,20], it is still unknown how healthy genetically extended lives are, and whether they suffer increased incidence of age-related diseases. One of the advantages of using *C. elegans* as a model organism is that it exhibits complex phenotypes that are related to functional aspects of human health. Thus, studies of *C. elegans* can provide insight into the relationship between health and age through longitudinal assessment of health and longevity.

1.2 Conventional approaches for experimental investigation of *C. elegans*

C. elegans' small size and transparency confer substantial advantages to neurological studies, in particular by permitting large scales in culturing, examination, and analysis. Its short lifespan allows a high turnover, further increasing the data available for any given study. However, the micron-scale worm is smaller than the limits of effective human

manipulation, and the large scale of experiments often inhibits individualized human intervention at any phase of a study. To address these fundamental limitations, experimental platforms based in microfluidics have gained popularity. I will review the trend of this technology in Chapter 1.3.

1.2.1 For the study of mechanotransduction

C. elegans sense various mechanical stimuli through different sensory neurons, most significantly, harsh and gentle touches. Several assays have been developed to differentiate the roles of individual neurons. Chalfie and Sulston developed an eyebrow hair assay to test for gentle touch sensitivity[18]. Animals are touched by stroking a hair across the body: behind the pharynx for the anterior touch response or in front of the anus for the posterior touch response. Chalfie *et al*. mapped out several touch receptor neurons using eye lash assay with laser ablation: AVM and ALML/R respond to anterior body touch, and PVM and PLML/R respond to posterior body touch[19]. A platinum wire is often used to stimulate harsh touch sensitivity[26]. Although it is a good tool to identify the role of individual neurons and the molecular mechanisms underlying mechanosensation, these now-standard mechanosensation experiments are qualitatively controlled and the results of these assay would vary largely depending on experimenter and probe, as well as from day to day; the behavior assessment is subjective, as only obvious acceleration and reversal can be consistently recognized, leading to large variations in the data depending on scoring of subtler, more ambiguous behaviour changes; lastly, this assay is incredibly labor-intensive,

as every worm must be individually picked onto a plate and manually touched for every behavior assay.

To record neuronal responses to mechanical stimulus, Suzuki *et al*. have developed a method using a piezo-driven micro stylus that can move a specific distance under computer control[27]. This greatly enhances the quantitative nature of the assay and allows the experimenters to apply repetitive, well-controlled mechanical stimuli to an immobilized worm while performing functional neural imaging via calcium indicators. However, since immobilization is usually accomplished by gluing, no worms can be recovered after the assay, and throughput is very low. For assaying moving animals, Park *et al.* also developed an piezoresistive cantilever-based approach, where a motor-driven stage tracks and follows a worm while the cantilever applies forces to the animal[28]. This approach also suffers from low throughput, as well as an inability to integrate calcium imaging.

1.2.2 For the study of longevity and healthspan

The implicit technological challenges of working with a large number of microscopic animals for the time required for a longitudinal study have historically made it difficult to establish fine control at the scale needed to establish significance. In the conventional lifespan assay, populations of worms are maintained and scored as dead by experimenters. Specifically, animals were scored based on movement after gentle prodding with a wire pick; failure of response was scored as death. Since this assay is labor-intensive and operated by hand, it is hard to scale up or guarantee robustness.

Although dietary restriction and temperature have been identified as important factors affecting aging in *C. elegans*[11,23,29,30], the ability to precisely control these inputs is fundamentally limited by using standard solid media in plates. As a food source, NGM plates with *Escherischia coli* OP50 have been used. However, the concentrations of bacteria on plates may be uneven due to inconsistent drying of plates and continual depletion of the food source with time. To control temperature, standard incubators have been used to maintain culture plates at set temperatures typically ranging from 15 °C to 25 °C. However, lifespan assays mandate that plates be moved from an incubator to a microscope, leading to constant variations in temperature that are difficult to account for. The requirement that populations be transferred between plates to maintain food concentration introduces additional error in food level and temperature, and therefore age. As a result of these limitations, *C. elegans* longevity study data is often small and collected infrequently, often daily.

1.3 Microfluidic approaches for experimental investigation of *C. elegans*

Miniaturization of experimental systems using standard photolithographic processes allows us to easily handle small volume of liquids and control flow at the micron scale. In particular, in biological applications, the soft elastomer polydimethylsiloxane (PDMS) has been widely used as a microfluidic material due to its biocompatibility and tunable mechanical properties[31-34]. Furthermore, the ease of producing features at the micron-scale allows for the design of experimental platforms at the same size scales as the biological species or phenomenon of interest. Microfluidic techniques allow for active manipulation

of flow and specimens on chips with highly controlled environmental conditions or lower consumption of reagent.

1.3.1 For functional neural imaging

In order to understand how animals sense their external environment to modulate behavior patterns, it is important to monitor neural activity under the application of well-controlled stimuli. Compared to macroscale systems, it is much easier to control environmental conditions such as temperature, nutrients, and chemical cues[35-39] in microfluidic devices due to laminar flow conditions, which enable simple control of concentrations in space and time[40]. This gives microfluidic techniques a higher degree of experimental control, often with much lower reagent consumption. In addition, recent studies demonstrate that the power of microfluidic toolsets also lies in facilitating automated, large-scale, and high-throughput experiments at high resolution when coupled with software and other hardware[40-42].

Specifically for *C. elegans*, many microfluidic platforms have been developed to monitor neural activity and behavior under spatially or temporally controlled stimuli, which had not been possible on standard agar plates (Figure 1.1)[37,38,43,44]. For high-resolution neural imaging, one of the important technical challenges is to immobilize the worms inside the field of view of a microscopy system. While paralytic drugs can be used, these drugs may have deleterious effects, potentially influencing the phenotypes observed and limiting further experimentation, or lowering experimental throughput because of the slow recovery of the animals from drugs and the long sample preparation time. In contrast,

the use of these drugs can be avoided on a microfluidic chip using non-anesthetic techniques on the worms such as cooling, compression and physical restriction, carbon dioxide, and gelation in microfluidic devices [35]. The effects of controlled stimuli such as chemical or oxygen on the neural and behavioral responses of either freely moving or partially immobilized worms is observed in the microfluidic devices (Figure 1.1b-e)[36,38,39,44]. In addition, this technology has been applied to neural regeneration studies, high-throughput imaging, and high-throughput screening based on phenotyping(Figure 1.1a)[35,42,45] However, there are currently no microfluidic devices able to deliver mechanical stimuli to *C. elegans* for functional imaging.

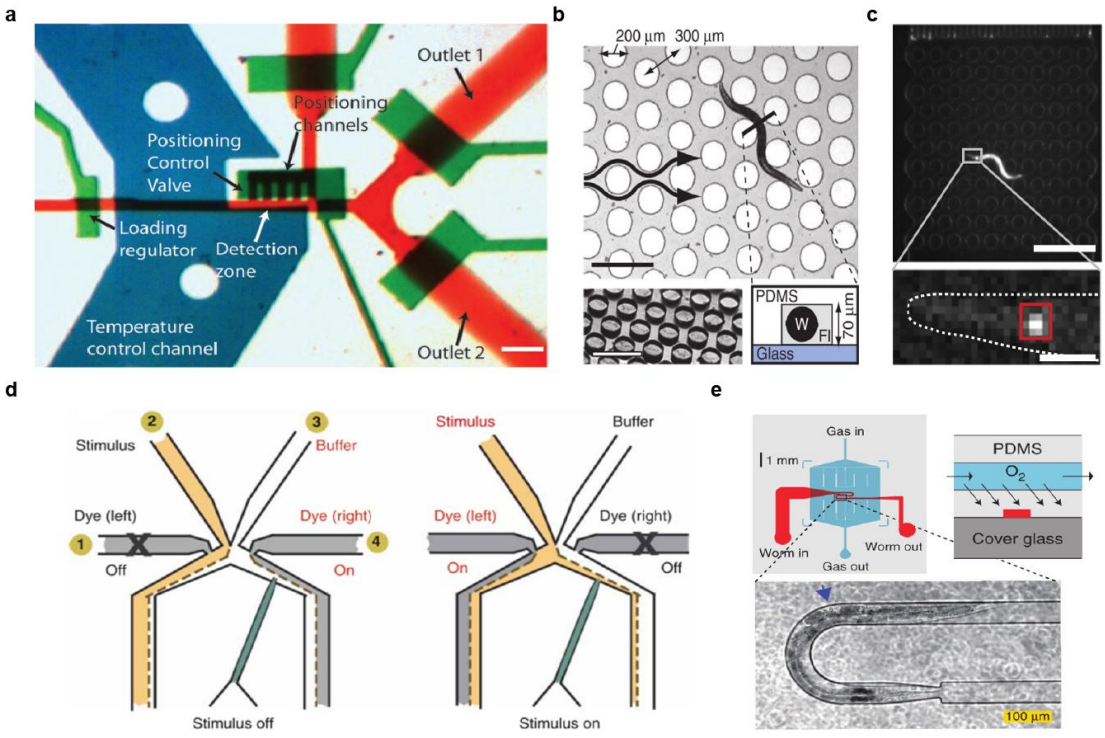

Figure 1. 1 Examples of microfluidic platforms for neural imaging in *C. elegans* **a**) The functional part of a microfluidic device for high-throughput imaging, phenotyping, and sorting of *C. elegans*. It can apply flow of a cooling fluid in a channel (blue) on top of the

worm imaging channel (red) to immobilize worms. Valves can be pneumatically actuated to handle worms (green). Two outlets can be used for worm sorting based on phenotypes; scale bar is 100 μm.[35] **b**) The microfluidic arenas that enable young adult worms to perform crawling locomotion through fluid-filled channels (gray) between cylindrical microposts (white). Arrows indicate flow direction. Also shown is an oblique view of the micropost array before device assembly (bottom left) and a cross-section schematic, indicating the glass substrate, polydimethylsiloxane (PDMS) top surface and posts, worm (W) and stimulus fluid (Fl); scale bars, 500 μm.[36] **c**) A microfluidic platform allows recording functional calcium imaging of AWA neuron in multiple freely moving animals under controlled chemical stimulation; scale bar (top), 1mm, scale bar (bottom), 50 μm.[38] **d**) A microfluidic device for the delivery of chemicals to the worm's nose while performing functional calcium imaging in *C. elegans*. Chemical stimulations can be precisely controlled by alternating with buffer flows.[37] **e**) A microfluidic device for temporal delivery of oxygen. Gas can be delivered through blue channel on top of worm immobilizing channel (red).[39]

1.3.2 For the study of longevity and healthspan

For *C. elegans*, there are several platforms to produce survival curves by using microfluidic techniques[46,47] or other methods, such as hydrogel pads, multi-well plates, or commercial scanners[48-50], but neither combines the live and dead assay with imaging of behavior responses at high resolution during their whole lifetime. Furthermore, these platforms do not provide precisely controlled environmental conditions such as dietary level. To achieve a higher degree of environmental control, microfluidic systems with liquid culture method have been validated for developmental and lifespan assays[46,47,51]. These systems have the advantage of accommodating food exchange in microfluidic devices. However, these platforms do not have a temperature control system and are difficult to integrate with commercial incubators. Moreover, scalable and automated systems for operating many experiments simultaneously have not been validated. As a result, the data derived from these systems have been limited to proof-of-concept demonstrations.

As discussed previously, lifespan results vary widely, even among isogenic individuals, due to stochastic effects. In addition, there is a significant heterogeneity in behaviors of same-age individuals in aging populations. Thus, in order to elucidate the mechanistic explanations for variability of animal responses to stimulus during aging, we need a longitudinal study method to track changes in individual animals' response at different time points. However, there is no platform that can record individual behavior in sufficient quantities to obtain more information about heterogeneity across individuals during aging process.

1.4 Automatic approaches for experimental investigation of *C. elegans*

For easy and robust operation and high-throughput experiment in microsystems, autonomous or semi-autonomous systemic components are necessary. It requires microfluidic devices to be integrated with off-chip components such as computer controls and imaging processes[35,45,52-54]. Typically, it entails electronically controlled pressure regulators and off-chip solenoid valves actuated by a digital signal board, and a computer-controlled image acquisition and analysis system. For example, Chung *et al*. developed an automated microfluidic system coupled with customized software that enabled high-throughput, high-resolution microscopy, phenotyping, and sorting of *C. elegans* without manual intervention (Figure 1.1a)[35]. Crane *et al*. performed an autonomous forward screen based on high-content quantitative morphometric features in *C. elegans* with a computer-vision method[54].

Although several automatic microsystems have been developed, most microfluidic devices are currently created and operated in engineering labs where the difficulty of

setting up devices is secondary to creating novel designs. Most microfluidic platforms are painstakingly difficult to set up for new experimenters, which limits the ability of biologists and other non-engineers to use standard lab equipment. Therefore, one of the goals in this thesis is to develop easy-to-use microfluidic platforms that meet the needs and standards of biologists.

1.4.1 Software – Image analysis

As discussed above, one of the key aspects for automation is the analysis of images generated in the course of experimentation. For many applications, a qualitative assessment of the image is insufficient—quantitative measurements are necessary for rigor in explanation, or for statistical analysis. In many experiments, particularly in high-throughput ones, it is prohibitively impractical for image quantification and analysis to be done solely by hand, and it is here that the use of image analysis software becomes critically important.

The simplest software tools are those used to aid or facilitate manual image analysis. Commercial microscopy software, ImageJ, LabVIEW, and MATLAB all provide a wide array of image analysis and manipulation tools to carry out common image processing tasks. These manually assisted techniques, however, become extremely laborious for datasets that grow into the hundreds or thousands, on video footage, or on images that require high-density, detailed quantification. Below, we discuss some common techniques for the most common image-processing task, image segmentation, and functional neural imaging.

Technique	Training Data?	Runtime	Implementation Difficulty	Best for
Thresholding	No	Negligible	Trivial	Basic Image Segmentation
Filtering (Median, Gaussian, Sharpening, etc.)	No	Low	Easy	Noise Removal, Background Removal, Improving Segmentation, Edge Detection
Transform Methods (Fourier, Wavelet, Hough, Watershed, etc.)	No	Low	Easy to Moderate	Noise Removal, Image Analysis, Image Segmentation, Edge Detection
Machine Learning Methods (Support Vector Machines, shape models, etc.)	Yes	High (for training)	Moderate to Challenging	Image and Data Analysis, Image Segmentation, Object Detection
Deep Neural Networks	Yes	High (for training)	Challenging	Object Detection, Image Classification, Image and Data Analysis

Table 1. 1 Summary of Image Processing Techniques. A detailed exploration of the topic is beyond the scope of this paper, but this table summarizes the properties of the most common types of image processing methods. Note that these categories frequently overlap and most practical algorithms use a combination of methods, frequently with manual correction[55].

1.4.1.1 Image segmentation

Image segmentation, the identification of meaningful objects in images, is the most important problem that must be solved for rapid and effective processing of imaging data. The most straightforward methods involve thresholding, wherein parts of the image that are brighter than a certain, specified intensity are classified as objects. Basic variants of thresholding—direct thresholding and Otsu thresholding[56]—are by far the most commonly used techniques, and may be extended by simple well-justified filters or comparisons between multiple color channels. Other well-established techniques, such as the Hough and Watershed transformation, are often used to tackle more difficult images with overlapping or difficult to resolve objects[57-59]. These simple approaches have the advantage of being fast and very readily available, with known benefits and downsides. Unfortunately, it is rare for any given method to work immediately out of the box, and most methods require calibration of control parameters. Practical image segmentation of difficult image sets often involves trying multiple techniques, pre- and post-processing, fine-tuning of parameters, and, finally, manual correction.

More sophisticated machine learning-based image segmentation methods attempt to learn to identify objects by using extensive, manually segmented training sets to teach the algorithm how to identify desired objects. Discussion of the details of these methods are far beyond the scope of this review, but it is worth noting that methods like support vector machines (SVM) and shape models have been successfully used to identify synapses and other objects[40,60-63]. Recent computer vision techniques from the machine learning and computer science community, such as Deep Learning, are a substantial potential source of innovation.

1.4.1.2 Image analysis of calcium imaging data

For functional neural imaging, optical interrogation tools such as calcium imaging allow for non-invasive measurement of neural activity. Researchers can examine neuronal activities on cellular and subcellular levels by taking advantage of a variety of genetically encoded calcium indicators (GECIs), such as the GCaMP family, which can target to specific neurons with the appropriate promoters. A typical calcium imaging experiment results in a sequence of fluorescent images that capture the fluorescence intensity of interesting neurons in response to a stimulus. In order to extract fluorescence intensity throughout the recorded images, software is needed to analyze each image to calculate an average intensity value inside a region of interest (ROI) and background. If worms are not fully immobilized during the recording, an algorithm is needed to track individual neurons. Since the fluorescence intensity of calcium indicators changes proportionally to cytoplasmic concentration of calcium rather than universally changing by a constant value, calcium traces are typically plotted as $\Delta F/F_0$, where F_0 is a baseline of the average value of fluorescence prior to stimulus. The fluorescence value (F) can be computed by subtracting the background intensity from the ROI's intensity ($F = I_{ROI} - I_{Background}$). In order to minimize the effect of worm movement, one uses reference fluorescent proteins such as RFP on same target neurons. Thus, in strains where both GCaMP and other fluorescence protein are expressed, the ratio between intensity values were computed $\Delta R/R_0$ ($R = I_{GCaMP}/I_{RFP}$). Several developed image analysis algorithms for the quantitation of functional imaging data or the extraction of behavior modes are discussed in later sections.

1.5 Thesis objective

As discussed previously, there are technical limitations to conventional methods that prevent high-throughput functional imaging and long-term individual animal imaging in large scale with highly controlled environmental conditions. In order to overcome these technical limitations, the purpose of this thesis is to develop automated high-throughput microsystems for functional neuroimaging with controlled mechanical and chemical stimuli to study sensory integration in the nervous system of *C. elegans,* as well as to develop automated microsystems for longitudinal culture and imaging of individual animals with highly controlled environmental conditions, in order to study the process of health and aging in *C. elegans*.

1.6 Thesis outline

The thesis consists of five chapters. Chapters Two and Three present the collection of developed microfluidic devices for high-throughput functional imaging in *C. elegans* and mechanical stimulation across all life stages. This work demonstrates the utilization of these technologies to develop new biological insight about the mechanism of mechanosensation in nervous system. Chapter Four presents an integrated microsystem to address the experimental challenges hindering large-scale, long-term tracking of health and longevity trajectories of individual worms in a variety of controlled environmental conditions. In addition to the validation of the use of these systems for aging study, this

work examines the feasibility of assessing the connection between health metrics in terms of age-related behavior profiles and longevity outputs. Finally, the last chapter provides a conclusion and suggestions for future work.

CHAPTER 2. HIGH-THROUGHPUT CONTROLLED MECHANICAL STIMULATION AND FUNCTIONAL IMAGING *IN VIVO*

2.1 Introduction

Mechanosensation is required for multiple sensory modalities such as touch, hearing, and balance, and is linked to a multitude of disorders including deafness[1,2,64,65]. Molecular mechanisms for mechanotransduction have been partially elucidated using a variety of model organisms, including *Caenorhabditis elegans*[4-9,13,14,19,66-68]. Conventional mechanosensation experiments with *C. elegans* typically involve the manual delivery of a mechanical stimulus to anterior or posterior regions of animals via an eyebrow hair or metal pick[18,19,26,69], and visual scoring of touch avoidance behavior, an assay subject to considerable variability between experimenters. Computer-controlled stimulation methods, for example using a piezo-driven micro stylus, have been used with electrophysiological and functional imaging approaches to deliver more repeatable mechanical stimuli to animals[27,70]. However, recording of neuronal responses by patch clamping or calcium imaging in response to precisely controlled mechanical stimulation requires animals to be immobilized with glue[7,27,70], limiting experimental throughput and disallowing the recovery of animals for screens or further experimentation. Moreover, gluing itself is likely to affect neuronal or circuit response, and differences in the extent of gluing introduce additional experimental variability.

Microfluidics has long been used as a "lab-on-a-chip" technology, allowing for well-controlled and high-throughput experiments with small samples[32]. In addition to enabling precise perturbations on the micron scale, microfluidic devices can easily be designed to work together with optical microscopy, allowing for imaging of fluorescent probes such as calcium indicators. For *C. elegans* experimentation particularly, microfluidics has been a widely adopted technology due to the match in length scale and compatibility with fluid handling[71]. Various devices have been developed for delivering a variety of stimuli, including chemical cues and temperature gradients, while simultaneously recording neuronal responses through calcium imaging[30,36,37,72-78]. In contrast, there are currently no microfluidic devices capable of delivering mechanical stimuli to *C. elegans*, or do so while recording neuronal activities in a controlled manner. In this work we present a microfluidic platform for delivering robust and precise mechanical stimuli to *C. elegans* by using pneumatically actuated structures. The device is fully automated, minimizing human variability and improving experimental throughput; it is fully compatible with fluorescent imaging of calcium dynamics of neurons, which enables mechanistic interrogations as well as high-throughput genetic or drug screens. Furthermore, the mechanical stimulus module of the device can be easily integrated with other microfluidic modalities, allowing for multimodal stimulation for sensory integration studies. Here we demonstrate the design and utility of such a system in the context of high-throughput screening, as well as interrogate circuit dynamics in multimodal sensory behavior.

2.2 Methods

2.2.1 Strains

C. elegans were maintained under standard conditions and fed OP50 bacteria[79]. The following strains were used in this study:

AQ3236 *ljIs142[mec-4::GCaMP6m::SL2TagRFP, unc-119] II; unc-119(ed3) III*

TV17924 *wyls5007[ser2prom3::GCaMP6, egl-17::mCherry] X*

CX10979 *kyEx2865[sra-6::GCaMP3, Pofm-1::GFP]*

GT243 *aEx2[pglr-1::GCaMP6(s), punc-122::GFP]*

RW1596 *stEx30[myo-3p::GFP + rol-6(su1006)]*

To construct AQ3236, we used a single-copy insertion vector containing a GCaMP6M transgene codon-optimized for *C. elegans*, under the control of the *mec-4* promoter (a gift from Doug Kim at HMMI Janelia Research Campus). Single-copy chromosomal integrations were obtained using the MosTic procedure[80]. Unless otherwise specified, all worms imaged in this study are adults.

2.2.2 Chip Design and Fabrication

The device consists of worm inlet/outlet, imaging channel (50~60 μm deep), and four sets of actuated PDMS membranes. Animals loosely fit in the channel, and are trapped (but not held) in the imaging area by two sets of actuated membranes. The width of actuated

PDMS membrane is 150 μm, the distance between the first and second sets of membrane is 200 μm and the second and third sets of membrane is 250 μm.

Since worms were not immobilized using drugs, animals' head or tail can move in the imaging channel of the microfluidic chip. This movement sometimes blurs images. To reduce this effect, a three-step vertical tapering of the imaging channel was used to restrict out-of-plane movement. The thickness of first and second layers was 15 μm and third layer was 20 μm for the 50 μm deep imaging channel; these layers were created by SU-8 2015 negative photoresist (MicroChem) using standard photolithographic techniques[81].

To create the actuated PDMS structure to touch and trap worms, multi-layer soft lithography process[82] was used. For the bottom flow layer of features, 23:1 PDMS was deposited via spin coating to create a thin layer. For the top control layer, 10:1 PDMS was directly poured onto a blank master, which does not have any features, to create a thick and mechanically rigid handle layer. Both layers were then placed into a 90°C oven for 25-30 minutes until the control layer PDMS was rigid but sticky. After they were manually aligned, additional 10:1 PDMS was poured and cured for several hours to create a rigid handling layer for the device.

2.2.3 Calcium Imaging

All imaging experiments were performed on a Leica DMIRB inverted microscope using a 40x air objective (N.A. 0.75). Video sequences were captured using a Hamamatsu EM-CCD camera with 100 ms exposure time. Simultaneous two-color imaging was

performed using a DV2 beamsplitter (Photometrics) containing a GFP/RFP filter set. Excitation light for fluorescent imaging was delivered through a previously developed projector system[83]. In experiments for the measurement of mechanosensory neuronal responses, stimuli were delivered 10 s after recording baseline activity of neurons. In experiment for the measurement of interneuronal recording, stimuli were delivered 30 s after recording baseline activity of neurons. Videos were recorded for 60-180 s following stimulus delivery.

2.2.4 Data Analysis

Fluorescence intensities for each frame were extracted using customized neuron-tracking MATLAB scripts (Supplementary Fig. 7). In strains where both GCaMP6 and RFP are expressed, the ratio between intensity values were computed ($R = \frac{I_{G\_ROI}}{I_{R\_ROI}}$) in order to minimize movement artifacts. When only GCaMP was available, fluorescence values were computed by subtracting background intensity ($F = I_{G\_ROI} - I_{G_{Back}}$). GCaMP and RFP intensities were measured as the mean pixel intensity of the 100 brightest pixels of a circular region of interest (ROI) of 10 pixel radius. Background intensities were subtracted to adjust for variations in lighting conditions, and were measured as the mean pixel intensity of an ROI in a background region (Supplementary Fig. 7). Calcium traces were computed as the change in R or F from the baseline value ($\frac{\Delta R}{R_o} = \frac{R - R_o}{R_o}$) or ($\frac{\Delta F}{F_o} = \frac{F - F_o}{F_o}$) . Baseline values were computed as the mean R or F prior to stimulus delivery.

2.2.5 Drug screening

Worms were roughly synchronized by picking 20-25 L4 worms and allowing them to lay eggs overnight before removing them from the plate. After two days at 20°C, tightly age-synchronized populations of worms were obtained by washing adults and L1s off of these plates and then washing newly hatched L1s from these plates after an hour interval. The 84 compounds of the Screen-Well Orphan library (ENZO) were used for the drug screening. 20-30 tightly-synchronized L4 worms were placed on a 48-well plate (Greiner Bio-One) with 0.5 ml OP50 bacteria (OD 5) for non-treated worms and both 0.495 ml OP50 bacteria and 0.005 ml (100 µM) drugs for drug-treated worms. After 24 hours, worms were imaged. Among 84 compounds in the library, I tested the effect of 13 compounds on AVM neuronal responses at three different ages (from day 1 adult to day 3 adult). These compounds were chosen randomly from the orphan ligand library.

2.3 Developed microfluidic device for the study of mechanosensation in *C. elegans*

2.3.1 Device design and fabrication

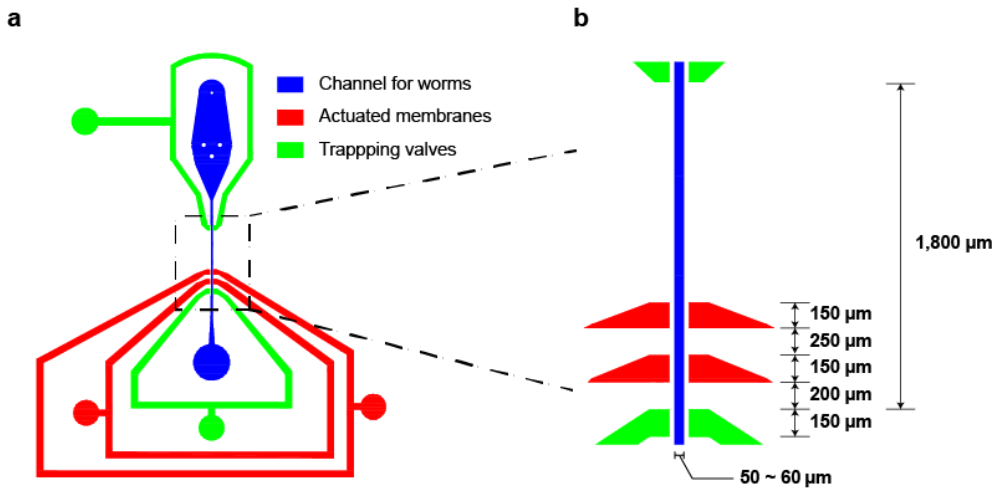

Figure 2. 1 Overview of microfluidic device dimensions. The device is composed of the channel for worms (50-60 µm deep and wide, which allow the animals to fit loosely inside), two sets of actuated membrane, and two sets of trapping valve. The width of both actuated PDMS membrane and trapping valve is 150 µm, the distance between first and second sets of membrane is 200 µm and second and third sets of membrane is 250 µm.

Our microfluidic device is optimized to deliver precise and repeatable mechanical stimuli to different anatomical regions of *C. elegans* (Figure 2.1a). After animals are loaded into an imaging channel (where the animals are not immobilized but their movement is much reduced from freely moving behavior), mechanical stimuli are delivered through two pairs of in-plane PDMS membrane structures (Figure 2.1 and 2.2a). The structures are pressure-actuated, and when deflected, exert a mechanical stimulus on animals trapped in the imaging channel. The deflection and deformation caused by these actuations are in

similar ranges as conventional approaches (Figure 2.3)[27,70]. Two additional actuated structures act as loading and imaging valves (Figure 2.2a). This design retains animals in plane and relatively stationary but not fully immobilized, thus allowing high-quality imaging of calcium transients in cell bodies and subcellular processes (Figure 2.2b). To automatically identify the fluorescently labeled neuron of interest and extract quantitative calcium transients, we developed a neuron tracking algorithm (Figure 2.4). The actuated structures are connected to a pressure source via individually controlled off-chip solenoid valves, allowing for an automated and rapid "load-and-image" routine (Figure 2.2c). Additionally, the duration and pressure of stimuli can be easily controlled, allowing for the study of a variety of behaviors upon mechanical stimuli such as graded response, habituation, and arousal. Furthermore, this design can be easily adapted to allow for sorting and imaging animals of various sizes.

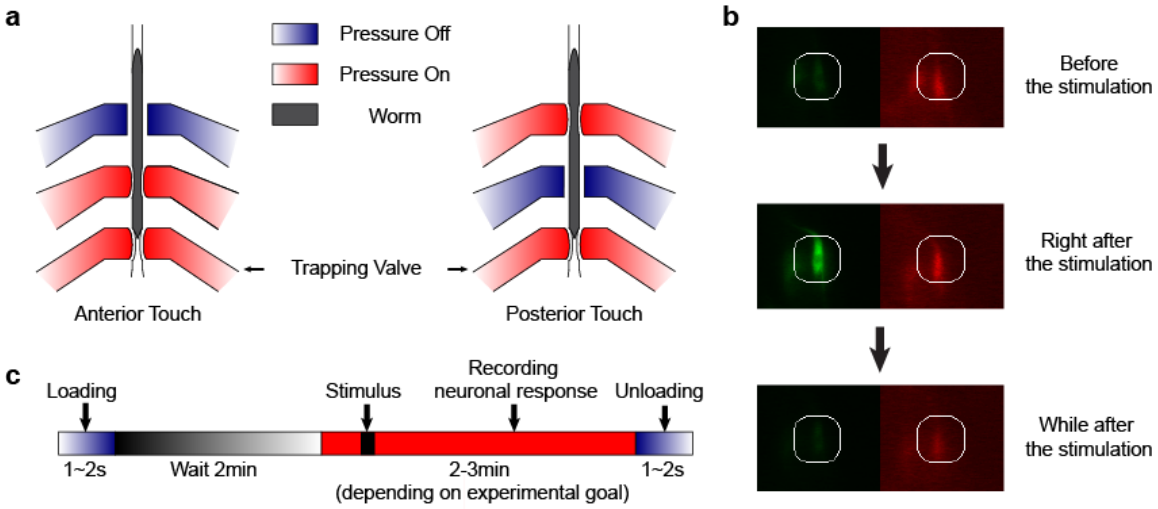

Figure 2. 2 Microfluidic platform to robustly deliver mechanical stimulus and image calcium responses in C. elegans mechanoreceptor neurons. **a**) The device employs multiple sets of actuated structures: valves to trap animals in a reproducible position, and two sets of actuations valves used to deliver mechanical stimuli to the anterior and posterior regions

of the body. **b**) Sample frames from an activated neuron show changes in fluorescence due to mechanical stimulus. Because animals are not fully immobilized, and neurons of interest move during recordings due to the mechanical stimulus and behavioral responses, a tracking algorithm was developed in order to automatically record the GCaMP and RFP intensities of traces from individual trials. **c**) Timeline of on-chip mechano-stimulation and functional imaging of neurons. The loading and unloading of each worm requires only a few seconds. Each animal is given 2 minutes to acclimate to the environment before being stimulated and imaged. Each trial is performed by recording video to track neuronal dynamic responses and applying mechanical stimuli.

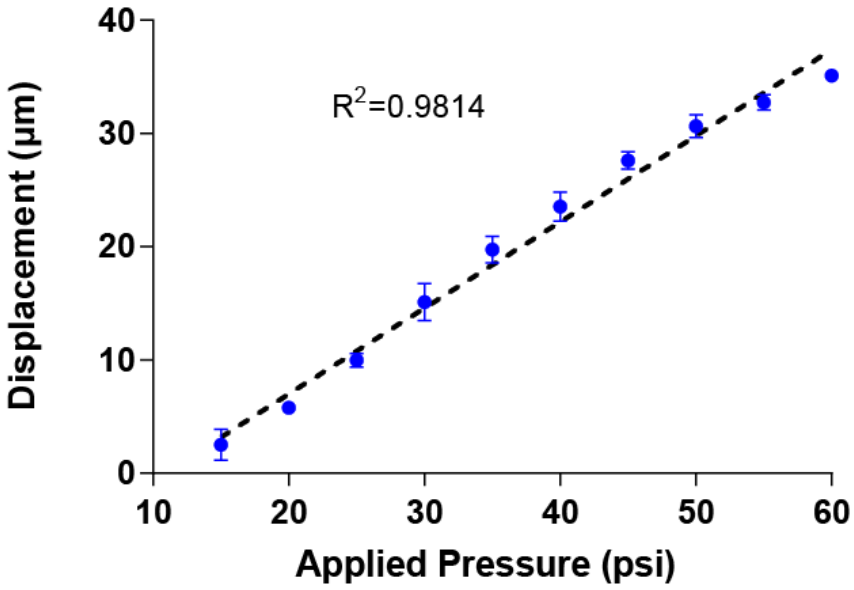

Figure 2. 3 Displacement of the actuated membrane by applying pressure (n=4 worms). It is important to note that the measurements were taken by images from transgenic worms expressing GFP along body-wall muscle (*stEx30[myo-3p::GFP + rol-6(su1006)]*). R-square value is 0.9814.

2.3.2 Examination of the responses of the classic gentle and harsh touch receptor neurons with single pulse stimulus

To demonstrate the utility of the system, we examined the responses of the classic gentle (AVM, ALMR/L, PVM, and PLMR/L) and harsh (PVD) touch receptor neurons[26] (Figure 2.5a). The stimulus is traditionally delivered to moving worms by a metal pick[26], or to immobilized worms by a stiff probe[7,27]. By imaging calcium transients in animals expressing the genetically encoded calcium indicator (GECI) GCaMP6m[84] in these touch receptor neurons, we show that the same device can deliver stimuli capable of exciting both the gentle and harsh touch neurons. Upon delivery of either a 1- or 2-second stimulus, calcium levels in cell bodies as well as in neuronal processes of both the gentle and harsh touch neurons rose as expected (Figure 2.5b - g). Spatially, these responses were consistent with the individual neurons' receptive fields as defined by anatomical and/or calcium imaging data[18,19,27,85]. AVM responded to anterior but not posterior stimuli (Figure 2.5h). In contrast, PVD responded to both anterior and posterior stimuli, as did PVM, with the responses to posterior stimuli being stronger for both of these classes of neurons (Figure 2.5i and j). These results demonstrate that the mechanosensory chip delivers biologically relevant, spatially well-defined stimuli.

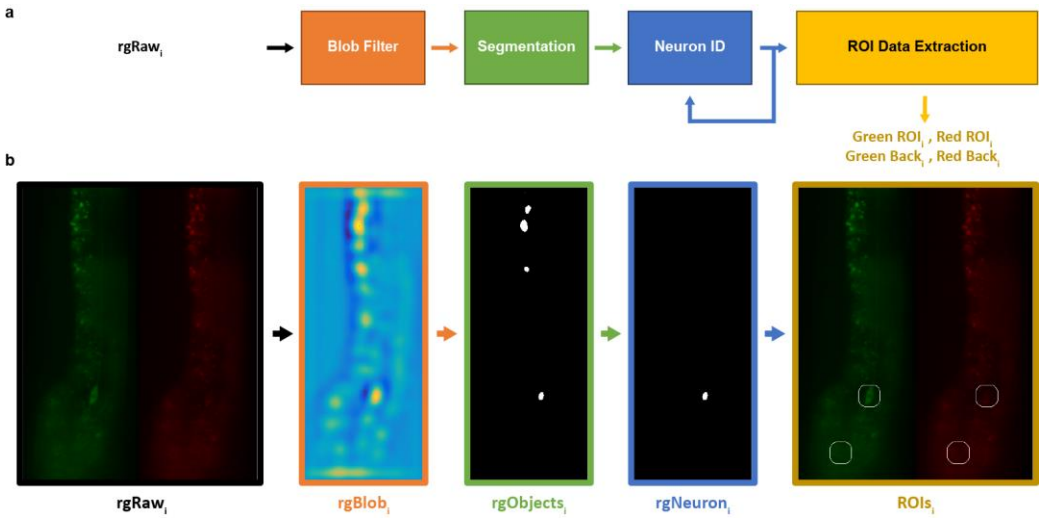

Figure 2. 4 Neuron Tracking Algorithm. In order to extract fluorescence intensities throughout recordings, a neuron tracking algorithm was developed. This was necessary because worms are not fully immobilized in the device, and mechanical stimuli often caused the neuron of interest to move within the field-of-view. **a**) Overall schematic of the neuron tracking algorithm. For each frame *i*, raw images are processed through a blob filter (Laplace of Gaussian filter) in order improve contrast and facilitate segmentation. Blob filtered images are segmented by applying an empirically determined threshold. The neuron of interest is identified by the user in the first frame, and by distance to the neuron in the previous frame. Lastly, once the neuron is detected for each frame, intensity values are extracted (Green ROI, Red ROI, Green Background, and Red Background). **b**) Example of algorithm procedure.

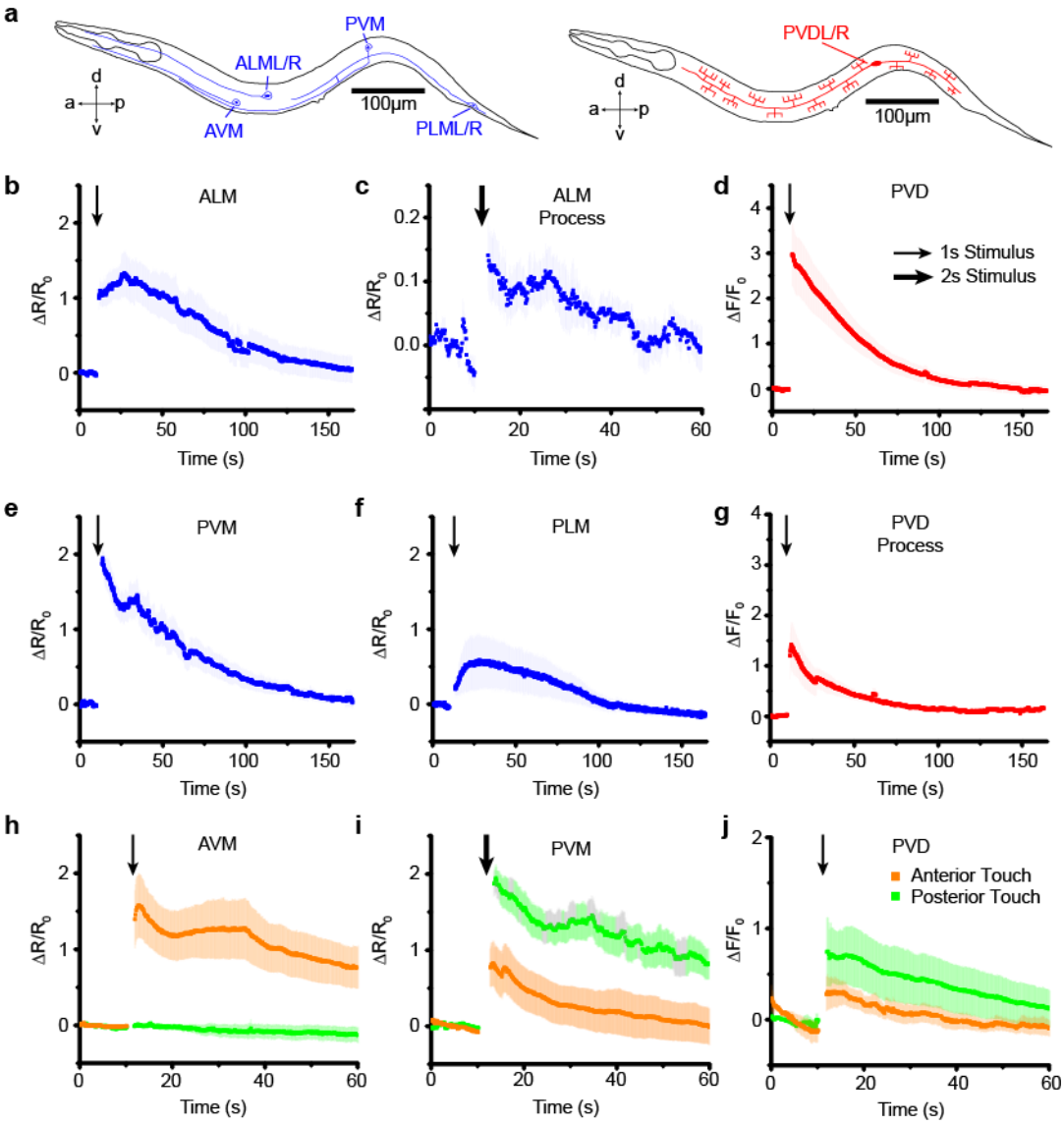

Figure 2. 5 **a**) Schematics of the mechanoreceptor neurons in this study: six gentle touch neurons -AVM, ALML/R, PVM, and PLML/R - and harsh touch PVDL/R neurons. **b - g**) Responses of the *C. elegans* gentle touch and harsh touch neurons to mechanical stimuli. Average traces of GCaMP6 signals in **b**) ALM to 1s stimulus (n=16), **c**) ALM process to 2s stimulus (n=7), **e**) PVM (n=17), **f**) PLM (n=9), **d**) PVD (n=9, 55psi), and **g**) PVD process to 1s stimulus (n=5) at 45psi. Error bars represent SEM. **h - j**) Gentle and harsh touch neurons exhibit reliable calcium responses when the stimulus was delivered to the appropriate regions of animals in our system. **h**) The activity of AVM responses to 1s anterior but not posterior stimuli (anterior: n=10, posterior: n=5) at 45psi. **i, j**) Gentle touch neuron, PVM, (2s stimulation, anterior: n=10, posterior: n=11) and harsh touch neuron, PVD, (2s stimulation, anterior: n=9, posterior: n=3) respond to both anterior and posterior stimuli at 45psi. Error bars represent SEM.

Because our system delivers mechanical stimuli by applying externally controlled pressure to actuated structures, the stimuli can be regulated by the magnitude and duration of applied pressures (Figure 2.6 – 2.10). In the range of stimuli of relevance, the deformation in the animal tissue is roughly linear to the actuation pressure (Figure 2.3). To examine the effects of these two parameters, we applied anterior stimuli of varying levels of pressure and durations, and measured calcium activity in AVM neurons (Figure 2.6a and b, Figure 2.8a and Figure 2.9) or PLM neurons (Figure 2.10). Peak calcium transients were roughly proportional to the pressure applied (Figure 2.6c) and the stimulus duration (Figure 2.6d). We also tested AVM's responses in the well-known *mec-4*/DEG/ENaC channel mutant (Figure 2.6e and f). As expected, the *mec-4* mutant gives negligible response and is insensitive to the magnitude of the stimulation input in the gentle touch regime, but is responsive to harsh touch, perhaps even more so than wild-type (Figure 2.6e and f). Similarly, in the harsh touch regime, we presented posterior stimuli of varying pressure and durations, and observed responses in PVD neurons (Figure 2.6g and h). As expected, compared to gentle touch neurons, PVD required higher pressure (55 psi) or longer duration of stimulus (5s) at low pressure to elicit similar responses. Furthermore, PVD also shows graded response to pressure and duration (Figure 2.6g and h, and Figure 2.8b).

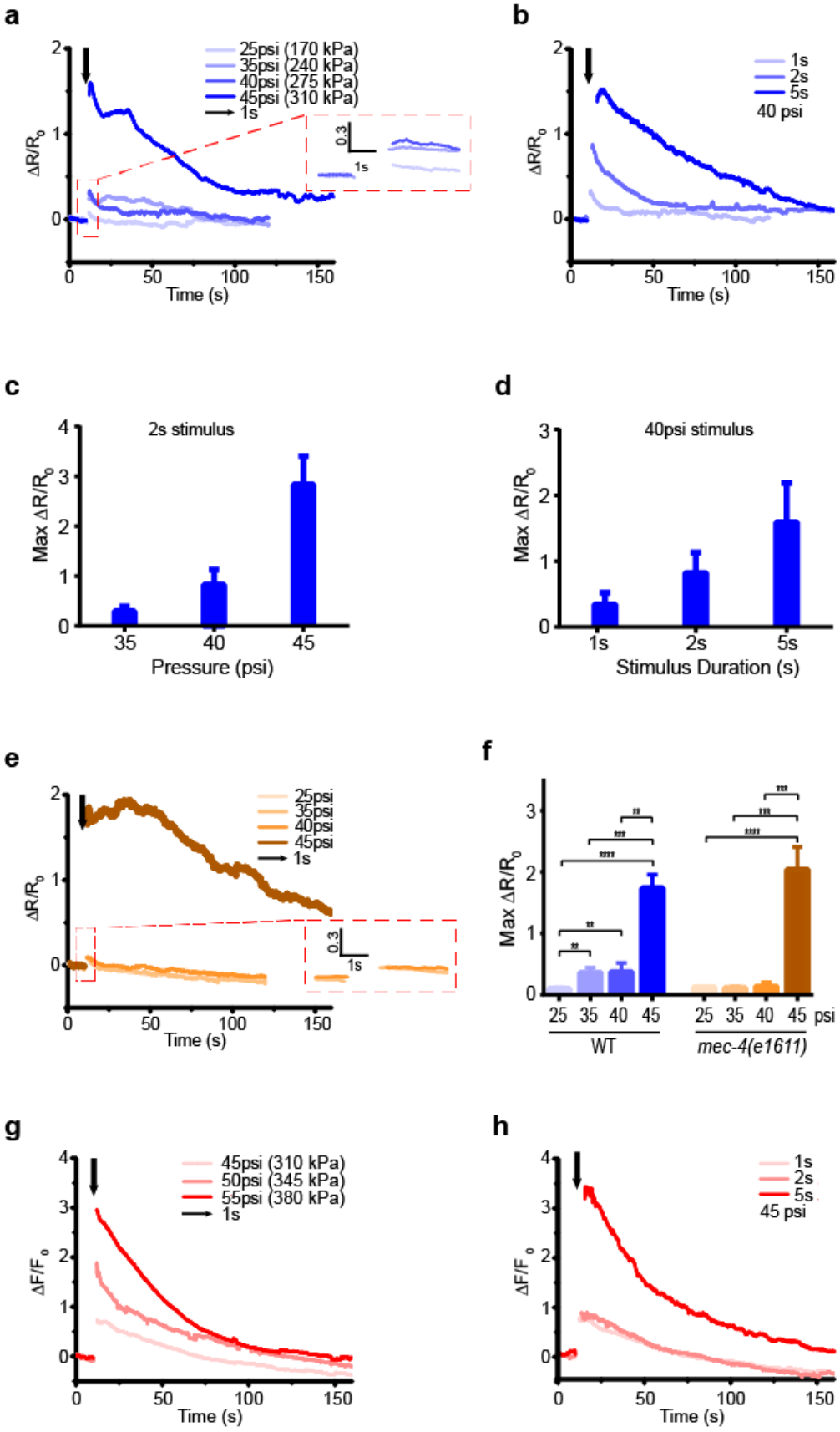
a
25psi (170 kPa)
35psi (240 kPa)
40psi (275 kPa)
45psi (310 kPa)
1s
ΔR/R0
Time (s)
b
1s
2s
5s
40 psi
ΔR/R0
Time (s)
c
2s stimulus
Max ΔR/R0
Pressure (psi)
d
40psi stimulus
Max ΔR/R0
Stimulus Duration (s)
e
25psi
35psi
40psi
45psi
1s
ΔR/R0
Time (s)
f
Max ΔR/R0
25 35 40 45 psi
WT
mec-4(e1611)
g
45psi (310 kPa)
50psi (345 kPa)
55psi (380 kPa)
1s
ΔF/F0
Time (s)
h
1s
2s
5s
45 psi
ΔF/F0
Time (s)

Figure 2. 6 The microfluidic platform delivers mechanical stimuli emulating both gentle and harsh touch by varying the magnitude of applied pressure and duration of the stimuli. **a - b**) Average traces of GCaMP6 signal in AVM neuron in response to diverse pressures and stimulus durations. **a**) Applied 1s stimulation with diverse pressures (25 psi: n=11, 35 psi: n=25, 40 psi: n=8, 45 psi: n=27). **b**) Applied 40 psi stimulation with diverse stimulus durations (1s: n=8, 2s: n=10, 5s: n=10). **c - d**) Maximum responses of calcium transients correlate with **c**) the applied pressure (2s stimulus, 35 to 45 psi) and **d**) the duration of stimuli (1 to 5s stimuli, 40 psi). Error bars represent SEM. **e**) Average calcium responses of *mec-4(e1611)* mutants in AVM neuron to diverse pressures with 1s stimulus (25 psi: n=18, 35 psi: n=10, 40 psi: n=9, 45 psi: n=10). **f**) Maximum responses of calcium responses of wild-type and *mec-4* mutant animals (Mann-Whitney Test, * p<0.05, ** p<0.01, *** p<0.001, **** p<0.0001). **g - h**) Average traces of GCaMP6 signal in PVD neuron in response to diverse pressures and stimulus durations. **g**) Applied 1s stimulation with diverse pressures (45 psi: n=9, 50 psi: n=6, 55 psi: n=9). **h**) Applied 45 psi stimulation with diverse stimulus durations (1s: n=9, 2s: n=4, 5s: n=6).

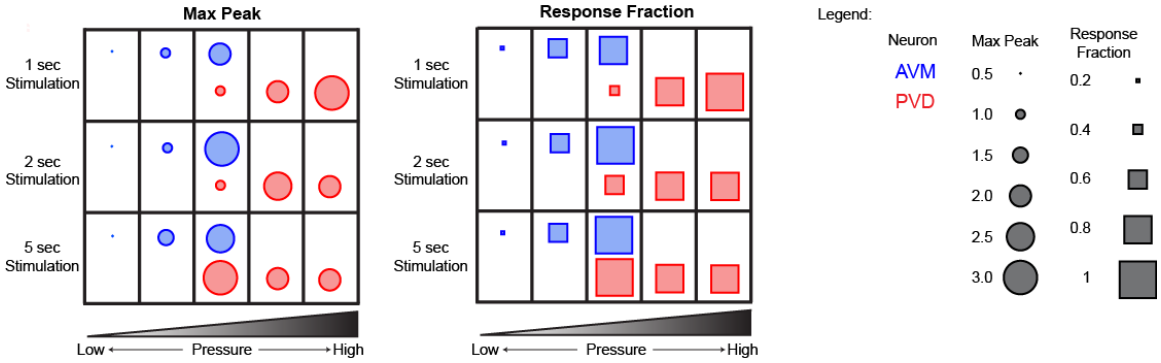

Figure 2. 7 Quantitative responses of AVM and PVD under different stimulation conditions. Both gentle touch AVM neurons and harsh touch sensing PVD neurons can be stimulated using this platform when using the right parameter regime. Each column refers to the applied pressure magnitude and each row refers to the applied durations of stimulation. For each data point, the circle size indicates the max response value from 0 to 3.0 and the rectangle size indicates response fraction from 0 to 1. Response fraction is defined as the percentage of traces that show a max response value of higher than 0.5.

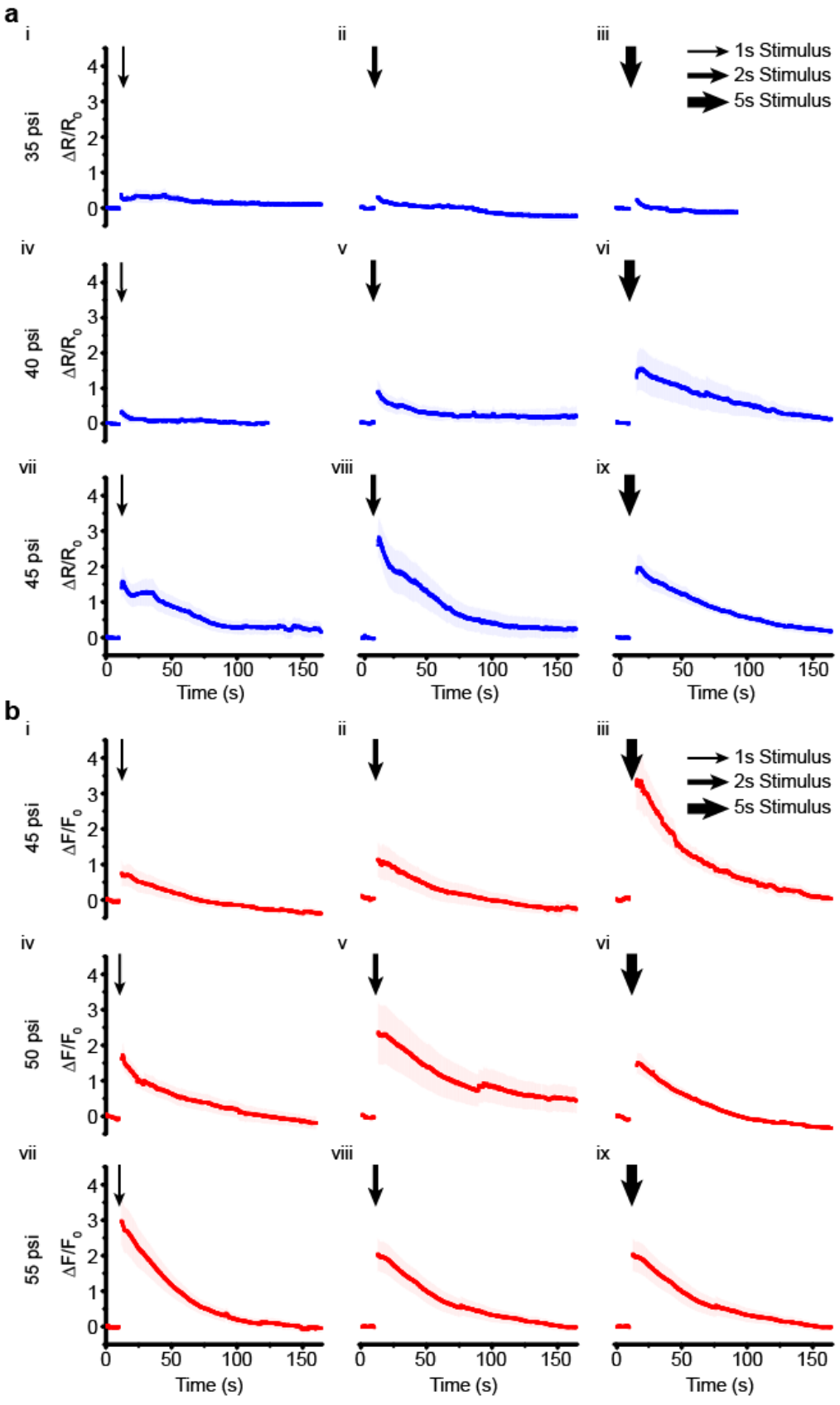
a
i
ii
iii
1s Stimulus
2s Stimulus
5s Stimulus
35 psi
40 psi
45 psi
ΔR/R0
iv
v
vi
vii
viii
ix
0
1
2
3
4
0
50
100
150
Time (s)
b
45 psi
50 psi
55 psi
ΔF/F0

Figure 2. 8 **a**) Average traces of GCaMP6 signal in AVM neuron in response to diverse pressures and stimulus durations (**i-iii**: 35 psi, **iv-vi**: 40 psi, **vii-ix**: 45 psi / **i**, **iv, vii**: 1 s stimulus, **ii, v, viii**: 2 s stimulus, **iii, vi, ix**: 5 s stimulus, **i**: n=25, **ii**: n=10, **iii**: n=8, **iv**: n=8, **v**: n=10, **vi**: n=10, **vii**: n=27, **viii**: n=6, **ix**: n=10). Error bars represent SEM. **b**) Average traces of GCaMP6 signal in PVD neuron in response to diverse pressures and stimulus durations (**i-iii**: 45 psi, **iv-vi**: 50 psi, **vii-ix**: 55 psi / **i**, **iv, vii**: 1 s stimulus, **ii, v, viii**: 2 s stimulus, **iii, vi, ix**: 5 s stimulus, **i**: n=9, **ii**: n=4, **iii**: n=6, **iv**: n=6, **v**: n=9, **vi**: n=10, **vii**: n=9, **viii**: n=10, **ix**: n=10). Error bar represent SEM.

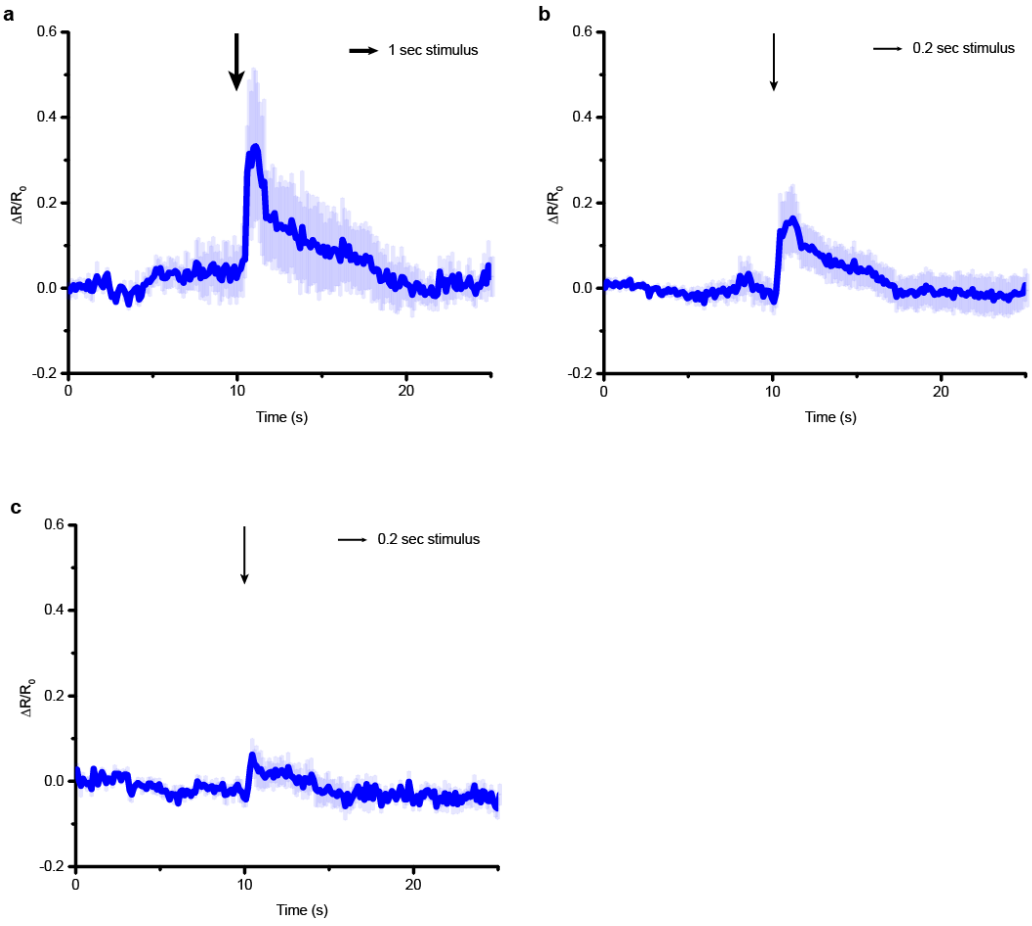

Figure 2. 9 AVM cell body responses to various stimuli with low pressures and durations **a**) 30 psi and 1 s (n=4), **b**) 30 psi and 0.2 s (n=10), **c**) 15 psi and 0.2 s. AVM response is reduced when using lower pressures (compare a to Fig. 2a, a to c). Response is also attenuated when using shorter durations (compare a to b). Error bars represent SEM.

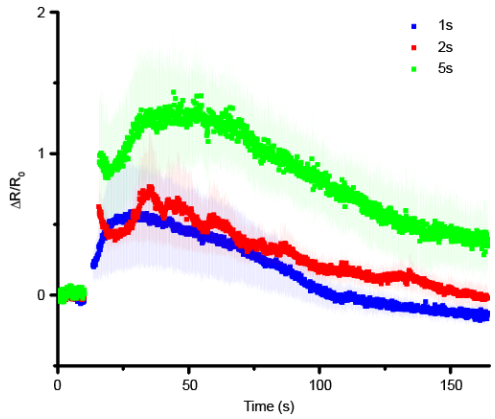

Figure 2. 10 PLM cell body responses to various stimulus durations (1s: n=9, 2s: n=4, 5s: n=4). Similar to those of AVM, maximum responses in PLM were proportional to the stimulus duration.

Interestingly, in addition to response magnitude, the response rates of both the gentle touch and the harsh touch neurons are also functions of the stimulation pressure and duration (Figure 2.7). For AVM, stimuli with actuation pressure higher than 40 psi produce a response rate (fraction of animals responding) of >90%, while below 30 psi the response is more stochastic (<20%) (Figure 2.7 and Figure 2.9). Applying stimuli at lower actuation pressure also elicits a less sustained response or small magnitude of response and shorter stimuli elicits less response.

2.3.3 Repeated pulse stimuli

Besides simple stimulation, our system can also be used to deliver repeated stimuli in order to examine phenomena such as habituation and desensitization. Previous work has shown that presenting repeated mechanical stimuli can cause habituation in mechanosensory neurons[27]. To determine whether this phenomenon can be recapitulated in our system, we delivered repeated stimuli to animals using either short (1s) or long (3 min) inter-stimulus intervals (Figure 2.11 and Figure 2.12). When receiving repeated stimuli with short intervals, the neurons exhibited an incremental increase in response magnitude up to the second stimuli, and then a reduced response in later stimuli (Figure 2.11a and c, Figure 2.12). In contrast, when using long inter-stimulus intervals, the response magnitude was reduced after each stimulus (Figure 2.11b and d). These results are consistent with previous observations that habituation is dependent on inter-stimulus durations[27]. Thus, these experiments demonstrate how simple changes of operational parameters allow us to use the same device for a wider repertoire of the device utility.

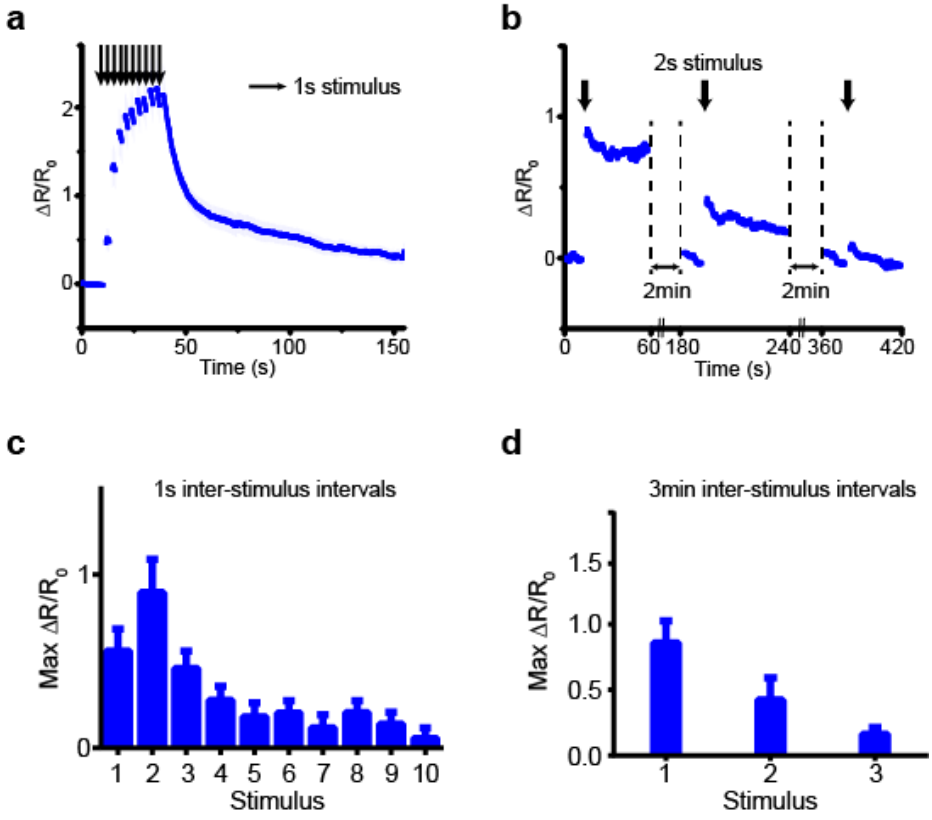

Figure 2. 11 Delivery of precisely repeated stimuli in AVM. **a, c**) When worms are exposed to 1s stimuli with short inter-stimulus intervals (1s), the neurons exhibited an incremental increase in response magnitude up to the second stimulus, and a reduced response in later stimuli (n=19). **b, d**) In contrast, when exposed to 2s stimuli with long inter-stimulus intervals (3 min), the response magnitude was reduced after each stimulus (n=10). Error bars represent SEM.

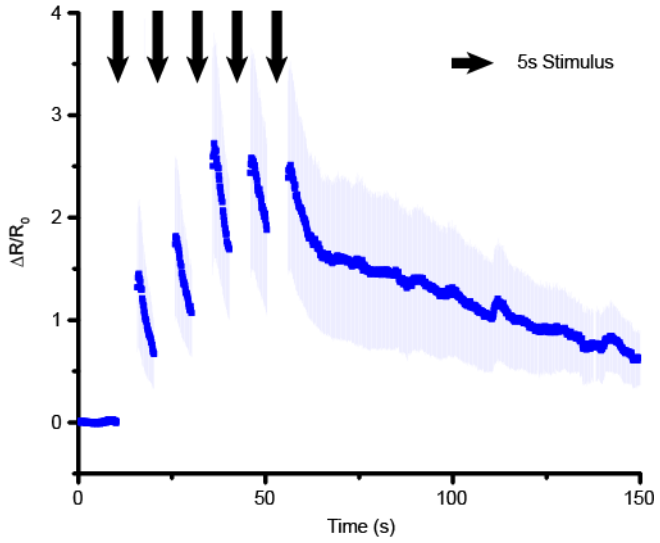

Figure 2. 12 AVM cell body response to delivery of repeated stimuli with long durations (5s). Similar to Figure 2.6j, traces showed incremental increases in the first few stimuli, and showed a decreased response in later stimuli.

2.4 Demonstration of the ability of drug screens based on quantitative mechanosensory phenotypes

In contrast to gluing protocols, our system allows for automated imaging by streamlining the handling of the worms; this in turn allows for high-throughput experiments that were not practical before. To demonstrate the ability to perform rapid screens, we examined the effect of small molecules from an orphan ligand library on mechanosensation. We exposed animals to the compounds in L4 stage, and imaged AVM activity when delivering an anterior stimulus to adult worms (Figure 2.13a). Figure 2.13b shows a typical response of wildtype animals without drug perturbation: calcium traces typically reach a maximum value shortly after the end of stimulus, and then slowly decline back to baseline levels. In order to examine how each drug affects mechanosensation, we

quantitatively compared three metrics (max ΔR/Ro, delay time, and half-life), as well as the fraction of animals responding, between drug-treated animals and untreated animals (Figure 2.13c-h, Figure 2.14, and Figure 2.15). We imaged adult animals exposed to 13 different drugs and quantified the established parameters for the screen criteria (Table 2.1). While most of the drugs screened lowered the number of animals responding to mechanical stimulus, interestingly, a few drugs slightly increased the response fraction (Figure 2.13c). We also analyzed differences in the metrics measure calcium dynamics for the drug treatment conditions, and found that five of the drugs we tested significantly affected mechanosensation response dynamics (Figure 2.13d - f). Specifically, D-Alanine (#5) and D-Arginine (#8) significantly attenuated the max ΔR/Ro while increasing the delay in the responses (Figure 2.13d, e, h). In contrast, D-Lysine (#4) only attenuated the max response (Figure 2.13d and g). Two other drugs had effects only in the decay-time of response (Figure 2.13f - h). D-Isoleucine (#3) induced considerably smaller half-life for the calcium transients to return to baseline, much faster than in untreated animals (Figure 2.13f and g). Lastly, β-Alanine (#6) significantly increased the half-life, and calcium transients decreased in a slow linear gradient, instead of a typical exponential decay (Figure 2.13f and h).

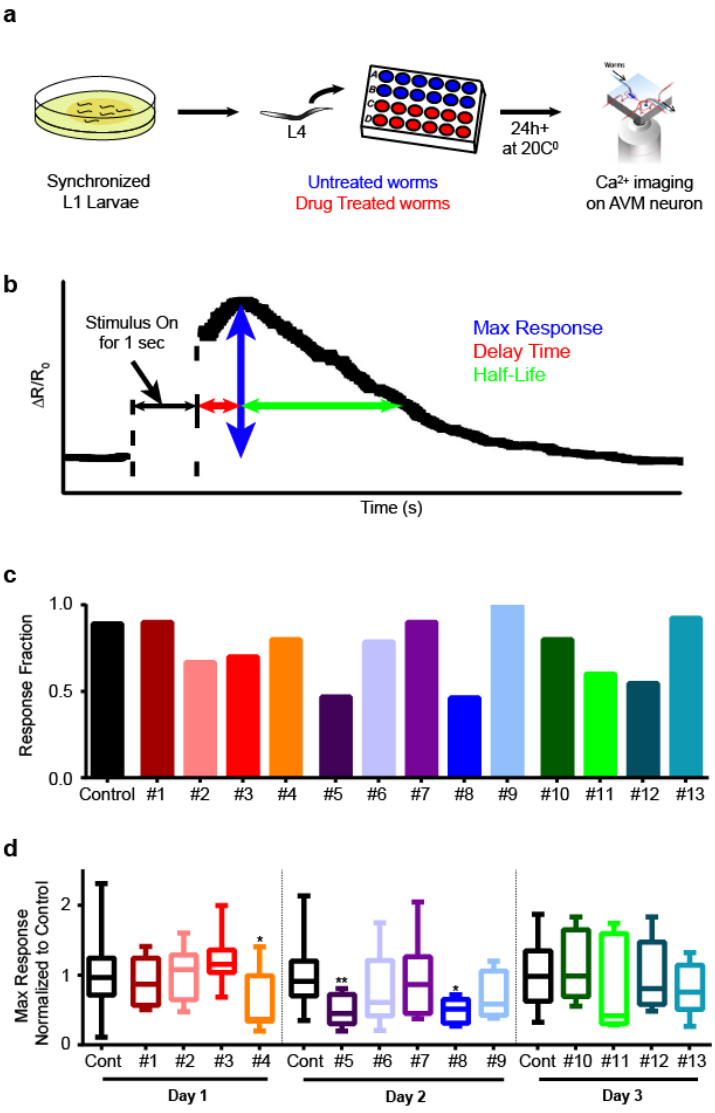
a
L4
24h+
at 20C⁰
Synchronized
L1 Larvae
Untreated worms
Drug Treated worms
Ca²⁺ imaging
on AVM neuron
b
Stimulus On
for 1 sec
ΔR/R0
Max Response
Delay Time
Half-Life
Time (s)
c
Response Fraction
1.0
0.5
0.0
Control #1 #2 #3 #4 #5 #6 #7 #8 #9 #10 #11 #12 #13
d
Max Response
Normalized to Control
2
1
0
Cont #1 #2 #3 #4 Cont #5 #6 #7 #8 #9 Cont #10 #11 #12 #13
Day 1
Day 2
Day 3

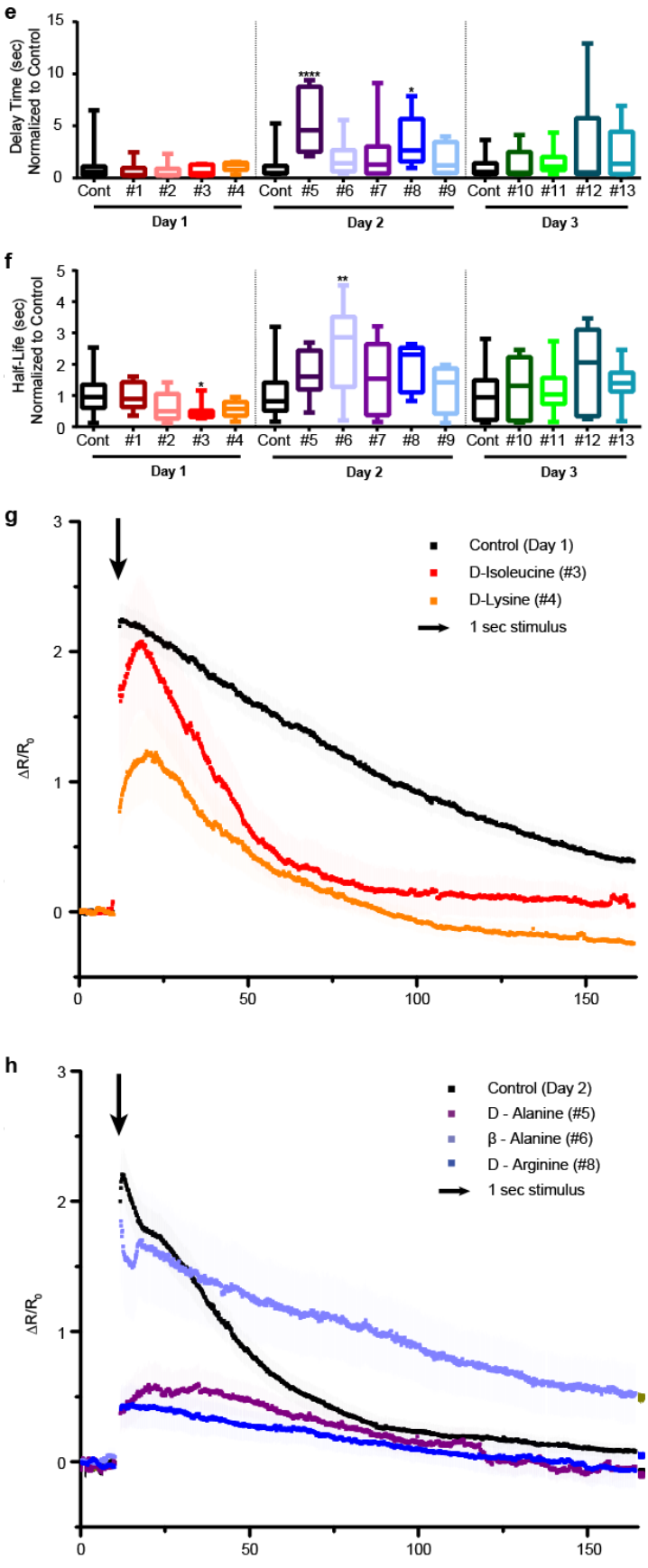
e
Delay Time (sec)
Normalized to Control
15
10
5
0
****
*
Cont #1 #2 #3 #4 Cont #5 #6 #7 #8 #9 Cont #10 #11 #12 #13
Day 1
Day 2
Day 3
f
Half-Life (sec)
Normalized to Control
5
4
3
2
1
0
**
*
Cont #1 #2 #3 #4 Cont #5 #6 #7 #8 #9 Cont #10 #11 #12 #13
Day 1
Day 2
Day 3
g
ΔR/R0
3
2
1
0
0
50
100
150
Control (Day 1)
D-Isoleucine (#3)
D-Lysine (#4)
1 sec stimulus
h
ΔR/R0
3
2
1
0
0
50
100
150
Control (Day 2)
D - Alanine (#5)
β - Alanine (#6)
D - Arginine (#8)
1 sec stimulus

Figure 2. 13 The microfluidic platform enables screens to examine compounds that may affect neuronal responses to mechanical stimuli. **a**) Experimental procedure for the drug screen performed. Synchronized L1 worms are grown in NGM plates to the L4 stage and then deposited in a 48-well plate. Drug treated worms are cultured with 0.5 ml OP50 *E. coli* bacteria and 100μM drugs. Control worms are cultured with 0.5 ml OP 50 *E. coli* bacteria (OD 5). Both groups of worms are incubated at 20℃ for at least 24h. Subsequently AVM responses to 1s stimulus were measured on-chip. **b**) Three metrics measured from individual calcium dynamic traces: maximum response, delay time (time between the end of the stimulus and the arrival of maximum response), and half-life (time it takes the response to decay to half of the maximum). **c**) Fraction of animal responses upon compound treatment. Several compounds produced a lowered fraction of responding animals, while a few slightly increased the response fraction. **d - f**) Sample traces showing how compounds affect specific parameters of neuronal response upon mechanical stimulation. Quantification of each response was normalized to that of the control group from the same day. **d**) D-Lysine (#4), D-Alanine (#5), and D-Arginine (#8) were shown to reduce maximum response, **e**) D-Alanine (#5) and D-Arginine (#8) were shown to increase the time to peak, and **f**) D-Isoluecine (#3) was shown to decrease the decay half-life. In contrast, β-Alanine (#6) was shown to increase the half-life. (Kruskal-Wallis Test, * $p<0.05$, ** $p<0.01$, *** $p<0.001$, **** $p<0.0001$). **g - h**) Average traces of GCaMP6 in AVM neuron for drug treated worms that cause significant differences from untreated worms in responses to 1 s mechanical stimulus. **g**) Day 1 adult worms (Control Trial 1: n=53, D-Isoleucine: n=10, D-Lysine: n=12), **h**) Day 2 adult worms (Control Trial 2: n=53, D-Alanine: n=15, β-Alanine: n=14, D-Arginine: n=13). Error bar represent SEM.

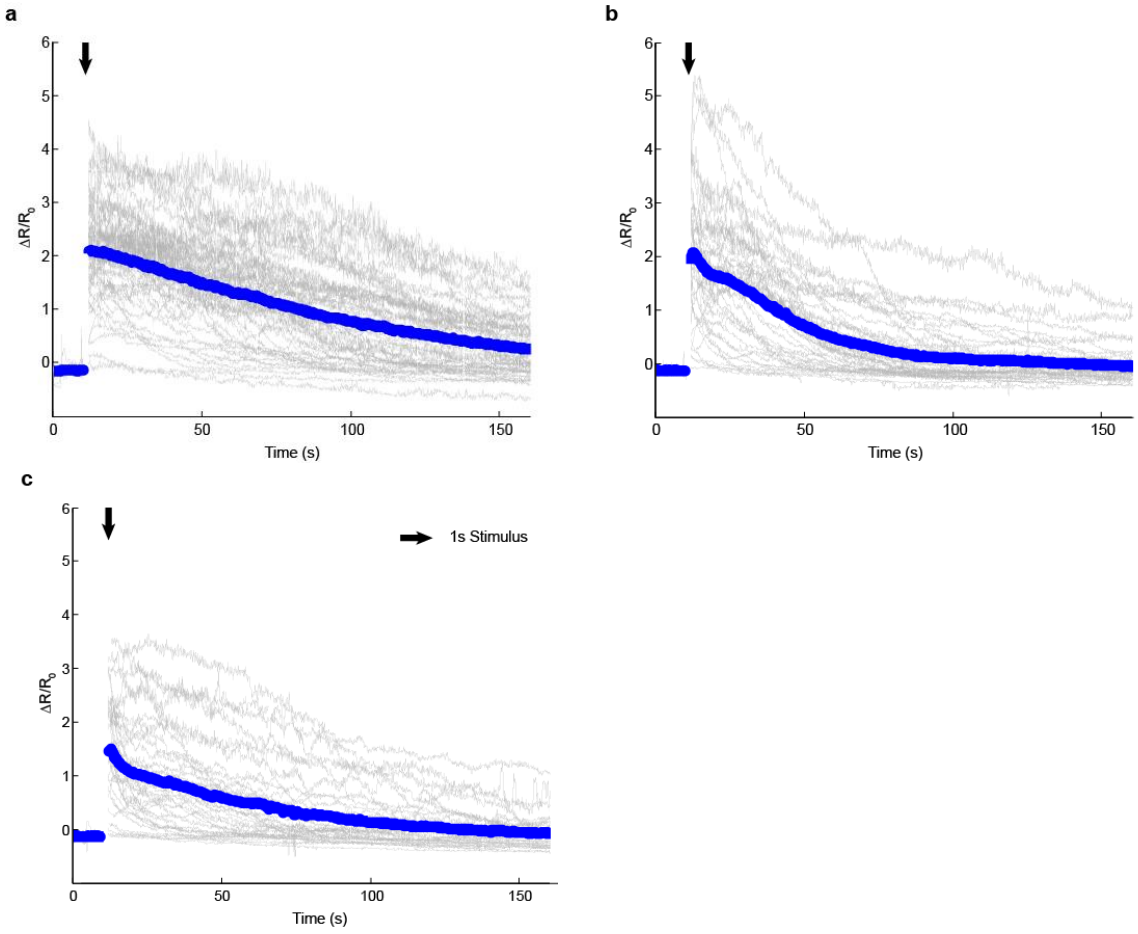

Figure 2. 14 Individual (gray) and average traces (blue) for AVM response in untreated animals for different control groups for drug screen. a) Day 1 (n=53), b) Day 2 (n=53), c) Day 3 (n=35) adult worms.

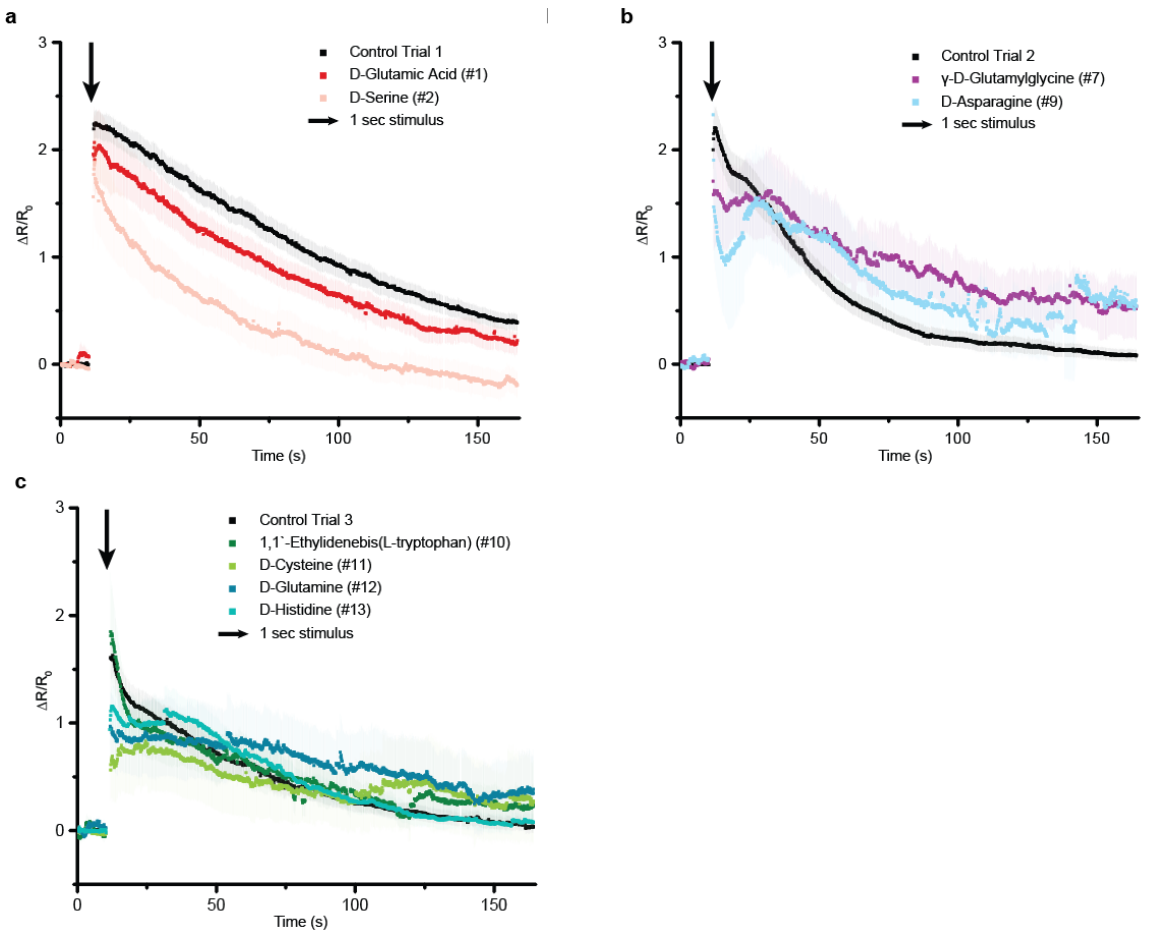

Figure 2. 15 Average traces for AVM response in drug-treated animals that do not show a significant difference from the control groups. **a**) Day 1 adult worms (Control Trial 1: n=53, D-Glutamic acid: n=10, D-Serine: n=12), **b**) Day 2 adult worms (Control Trial 2: n=53, γ-D-Glutamylglycine: n=10, D-Asparagine: n=4), c) Day 3 adult worms (Control Trial 3: n=35, 1,1'-Ethylidene-bis(L-tryptophan): n=10, D-Cysteine: n=10, D-Glutamine: n=11, D-Histidine: n=13).

Number	Name	Rationale	Sample size	# of responding worms
1	D-Glutamic acid	Putative endogenous ligand	10	9
2	D-Serine	Putative endogenous ligand	12	8
3	D-Isoleucine	D-Amino acid	10	7
4	D-Lysine	D-Amino acid	10	8
5	D-Alanine	D-Amino acid	15	7
6	β-Alanine	Endogenous	14	11
7	γ-D-Glutamylglycine	D-Amino acid	10	9
8	D-Arginine	D-Amino acid	13	6
9	D-Asparagine	D-Amino acid	4	4
10	1,1'-Ethylidene-bis(L-tryptophan)	Bioactive tryptophan derivative	10	8
11	D-Cysteine	D-Amino acid	10	6
12	D-Glutamine	D-Amino acid	11	6
13	D-Histidine	D-Amino acid	13	12

Table 2. 1 The 13 compounds of the orphan library were used for the drug screen (Figure 2.11-13). Sample size is the total number of tested worms and if the value of maximum responses is larger than 0.5, it is counted as a responding worm.

2.5 Integrated microfluidic device for the study of multimodal sensory integration

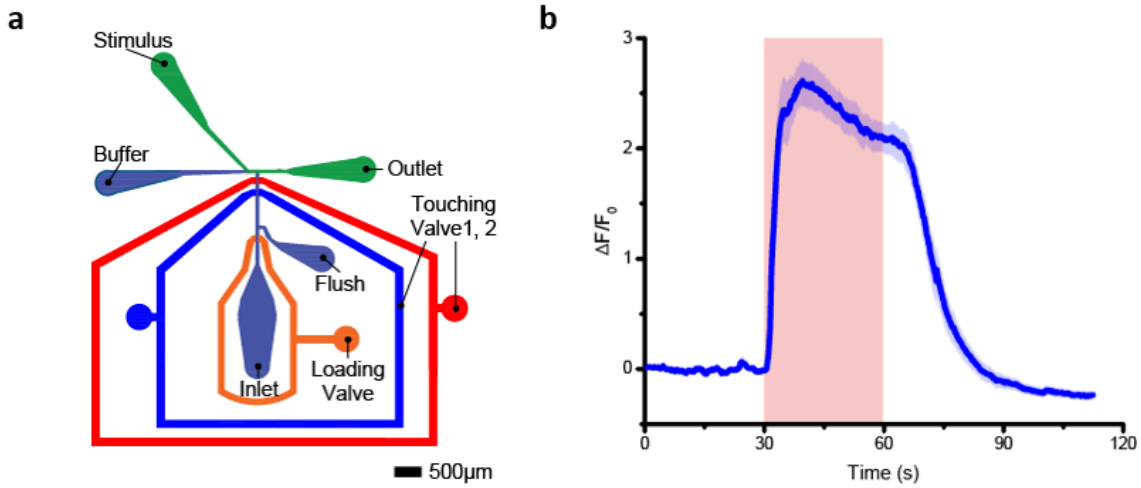

Figure 2. 16 **a**) Overview of microfluidic device for the delivery of multimodal stimuli. The device is composed of a channel for worms (Inlet and Flush channel), two sets of actuated membrane for mechanical stimuli (Touching valve 1,2), one set of trapping valve (Loading valve), two inlets for chemical stimuli (Buffer and Stimulus), and outlet. **b**) Average traces of GCaMP3 signal in ASH neuron in response to 30s 0.1% SDS stimuli (n=13). Error bars represent SEM.

Another advantage of using microfluidics to deliver mechanosensory stimuli is that it is compatible with other microfluidic components to provoke additional sensory responses, e.g. chemosensation[37]. *C. elegans* is a convenient system for studying multimodal sensory integration *in vivo*; worms have distinct sensory modalities such as mechanosensation and chemosensation, which allow them to find food sources and estimate danger. The difficulty to study sensory integration thus far is that there has not been a convenient method to integrate mechanosensory input with the existing tools, including microfluidic and optical methods[37,42,71,83,86]. With our mechanical stimulus device, incorporating chemosensory modules is readily attainable by simply adding channels to deliver chemical stimuli (Figure 2.16a); without mechanical stimulation, the response of a chemosensory neuron to a chemical cue is as expected (Figure 2.16b). To demonstrate the utility of the system for

multimodal sensory integration, we focused on the response of the PVC command interneurons to both mechanical and chemical stimuli. PVC interneurons are postsynaptic to both the posterior mechanoreceptor neurons PLML/R, as well as the posterior chemosensory neurons PHBL/R, that have been shown to respond to 0.1% SDS stimulus[17,19,87,88] (Figure 2.17a and Figure 2.18a). Using our device to deliver multi-modal stimuli, we tested the ability of PVC to respond to stimuli within the same mode and cross-modality. When a single sub-threshold stimulus in either modality is delivered (i.e. 30s SDS stimulation to the tail, or 1s mechanical stimulation to the tail), PVC shows a low probability of response (Figure 2.17b and c). Compared to upstream sensory neurons, PVC also responds with a lower magnitude and the response is more variable (Fig. 4b and c, and Figure 2.18b and c). Perhaps not so surprisingly, PVC's response to subthreshold stimuli in the same modality can be sensitized for subsequent stimulation (Figure 2.18d). More interestingly, when pre-sensitized by cross-modality sub-threshold stimuli (i.e. chemical before mechanical stimulus, or vice versa), PVC shows similar sensitized responses (Figure 2.17d - f). This sensitization is seen both in terms of the magnitude of the individual responses and the fraction of responding animals.

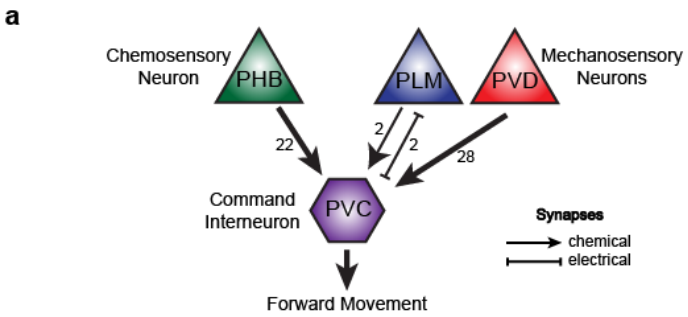

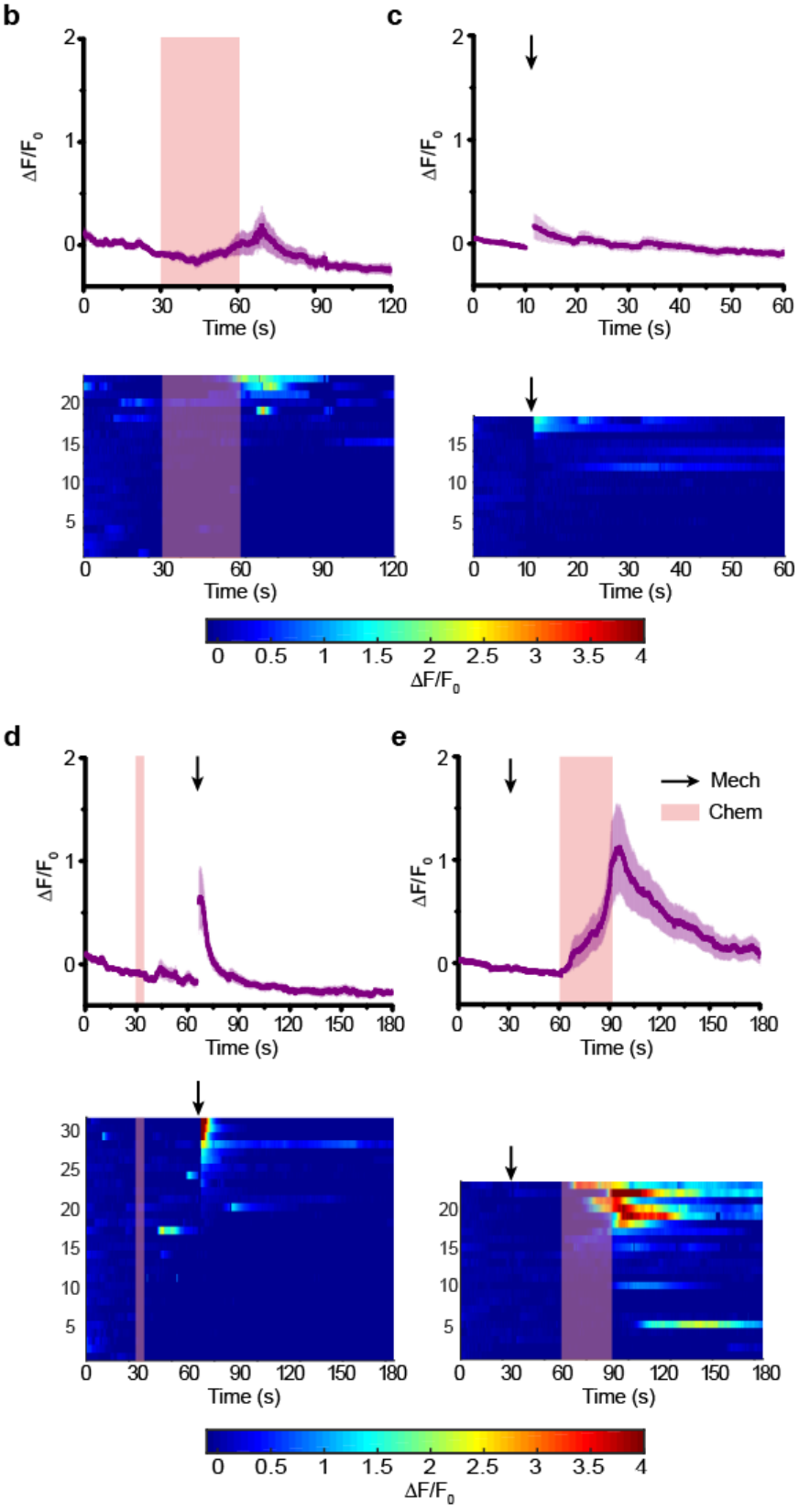
b
c
d
e
ΔF/F0
Time (s)
Mech
Chem

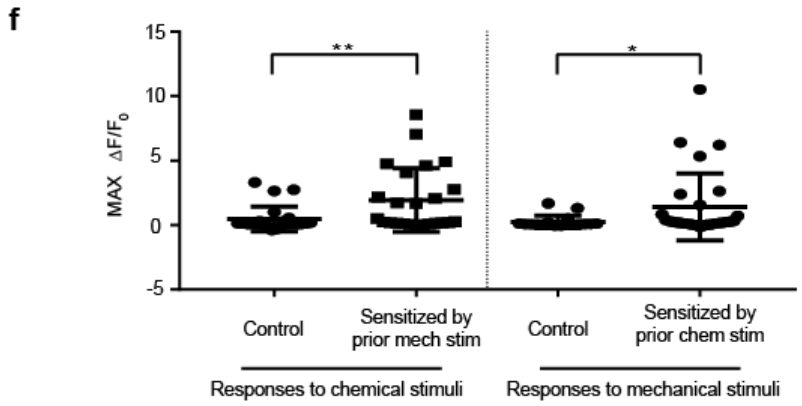

Figure 2. 17 Sensitization of the PVC interneuron responses. **a**) Simplified circuit diagram showing three sensory neurons connecting PVC to forward locomotion behavior. **b**) Maximum responses of calcium transients to either chemical or mechanical stimuli. Sensitization of PVC interneuron responses is produced by applying prior weak mechanical stimuli at 20 psi or 5s 0.1% SDS chemical stimuli (Mann-Whitney Test, * $p<0.05$, ** $p<0.01$). **c - d**) Responses of PVC interneuron to a single pulse of stimulation. **c**) Average of PVC calcium responses to 30s 0.1% SDS stimuli on tail of body (top) and individual traces (bottom, n=23). **d**) Average of PVC calcium responses to 1s weak mechanical stimuli at 20 psi on posterior region (top) and individual traces (bottom, n=18). Error bars represent SEM (top). In individual traces for outliers, if the value of calcium transient is greater than 4 or less than 0, it would be equal to 4 or 0, respectively (bottom). **e - f**) Sensitized PVC interneuron responses. **e**) Applying 5s 0.1% SDS stimuli enhances the responses of PVC interneuron to 1s weak mechanical stimuli at 20 psi (n=31). Averaged calcium responses (top) and individual traces (bottom) **f**) Applying 1s weak mechanical stimuli at 20 psi enhances the responses of PVC interneuron to 30s 0.1% SDS stimuli (n=24). Averaged calcium responses (top) and individual traces (bottom). Error bars represent SEM (top). In individual traces for outliers, if the value of calcium transient is greater than 4 or less than 0, it would be equal to 4 or 0, respectively (bottom).

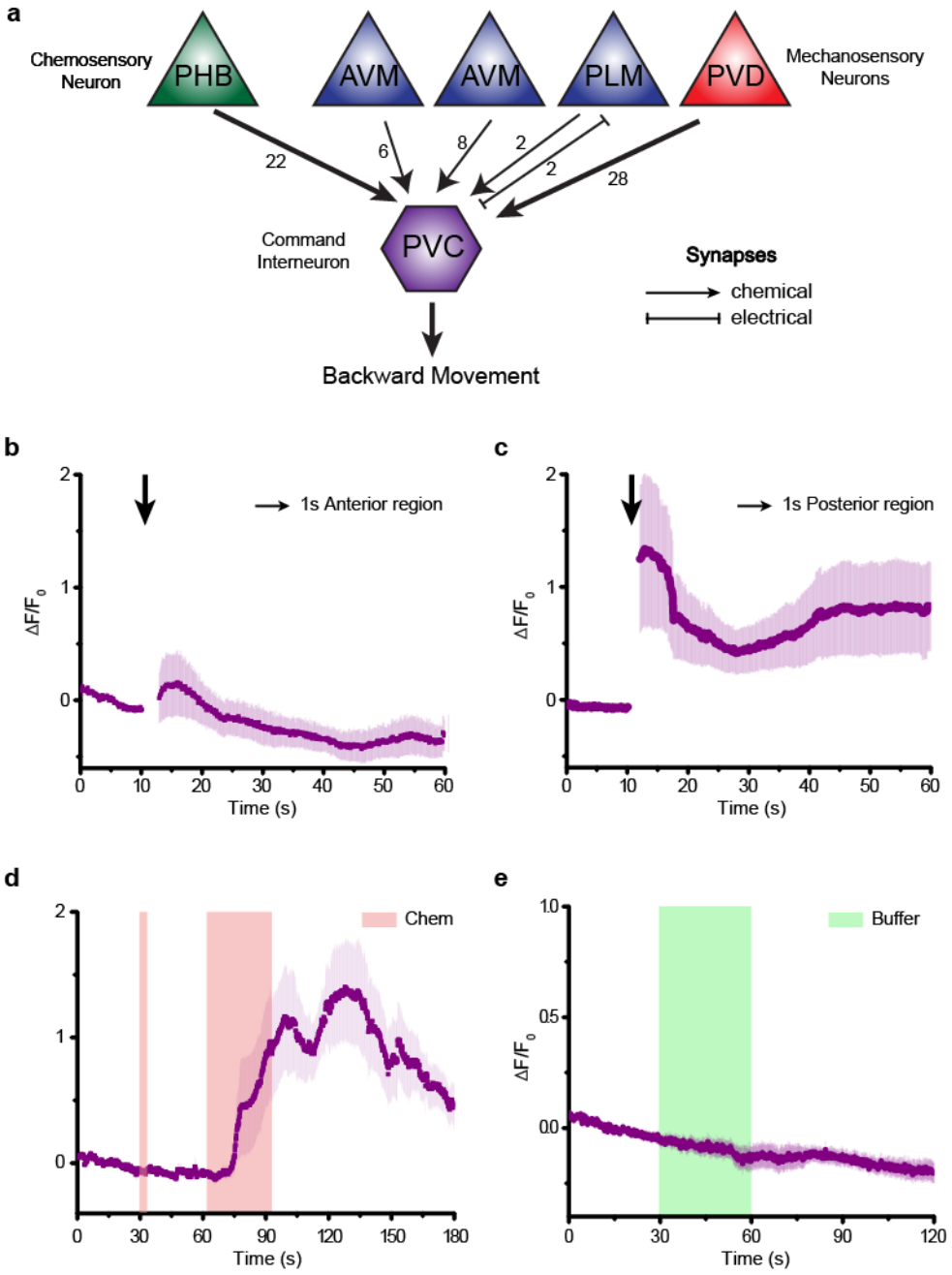

Figure 2. 18 **a**) Neural wiring diagram showing five sensory neurons in a circuit linking PVC to backward behavior, and the number of direct synapses between each pair of neurons. **b-c**) The activity of PVC responses to localized strong mechanical stimuli: **b**) 1s anterior stimuli (n=5) and **c**) 1s posterior stimuli (n=18) at 45psi. **d**) Applying prior 5s 0.1% SDS stimuli enhances the responses of PVC interneuron to next 30s 0.1% SDS stimuli (n=13). e) The activity of PVC responses to buffer to buffer changes (n=10). Error bars represents SEM.

2.6 Discussion

For fundamental studies of mechanosensation, quantitative live imaging is necessary, and to perform screens based on mechanosensory phenotypes requires large sample sizes. Our microfluidic platform allows for studying mechanosensation in *C. elegans* quantitatively and conveniently, allowing for the delivery of a variety of types of mechanical stimuli to live animals while recording neuronal activity. Experimental preparation (mainly washing) can be accomplished for a batch of animals, so the limiting step is imaging (tens of seconds to minutes depending on the experiments). Experimental throughput using our streamlined microfluidic system can be as high as ~100 trials per hour; it is also straightforward to automate and run these systems in parallel to further improve throughput. In contrast, the conventional approach (gluing worms and stimulating with a micro stylus and micromanipulator) generally yields ~10successful trials per day. The integration of hardware and software also allows for automated operations of imaging, stimulation, and quantitative analysis, further reducing potential human error and bias. This important improvement in throughput and standardization over conventional methods allowed us to conduct a novel drug screen based on neuronal dynamics due to mechanical stimuli. By using our system, we identified several candidates that strongly affect dynamics in mechanosensory neurons in a variety of ways. One can envision genetic screens performed in a similar manner to identify mechanosensory mutants. Many worm mechanosensory modalities, such as harsh touch and nose touch, involve multiple partially-redundant cell types, making behavioral assays ineffective for finding genes affecting these processes. With simple integration of sorting mechanisms on chip[42,52,89], it will be possible to conduct high-throughput forward screens for mutants affecting the responses of

individual neurons, using a GECI-based assay. The genes identified in such screens should provide insight into the underlying mechanisms of mechanosensation, as well as find potential therapies for sensory-loss conditions such as deafness.

Additionally, microfluidic incorporation of fluidic control can easily allow interrogation of other sensory modalities (e.g. olfaction) in combination with mechanosensation. We have shown that our platform is compatible with previous techniques for delivering chemical stimuli, enabling for the interrogation of integration of multimodal stimuli in the interneurons. This feature can greatly expand the repertoire of assay conditions to allow studies of sensory integration, arousal, habituation, and sensitization. For example, it has been previously shown that neural responses to sensory stimuli become more deterministic as information flows from sensory neurons to interneurons; behavioral responses, however, correlate more strongly with interneurons such as PVC[78,90]. We show here that PVC's response can be modulated, by prior sensory inputs, and that this modulation is cross-modal. This may point to an interesting ecologically relevant strategy for animal behavior, such that the reliability of the escape response depends both on the stimulus and on the current state of the circuit, as influenced by experience.

Because our platform employs a simple microfluidic device, it is easily adaptable to study biological systems of various sizes. Scaling the devices to be smaller can allow studies of mechanosensory neurons in worm larvae during development; scaling the devices larger can allow studies of the mechanosensation circuit during aging in *C. elegans*, as well as neurons and circuits in other model organisms such as zebrafish or fly larvae. Lastly, because the microfluidic chip allows unhindered optical access, integrations of

optogenetic methods[83,86,91-95] can also be straightforwardly carried out in this platform, thereby greatly expanding the repertoire of biological problems to be studied.

CHAPTER 3. *IN VIVO* IMAGING OF NEURONAL RESPONSES TO MECHANICAL STIMULATION IN *C. ELEGANS* LARVAE

3.1 Introduction

Developing animal brains undergo significant changes in structure and functional organization, and it is a critical time for the development of cognition, learning, and memory. Despite advances in the fields of neuroimaging, surprisingly little is known regarding the neural basis of cognition in normally developing nervous systems. In order to study the development of brain functions, such as memory and learning, in vivo functional imaging system is needed.

Among sensory modalities, mechanosensation is one of the most important for interacting with the surrounding environment: hearing in mammals involves mechanosensation, and diverse mechanoreceptors in animal skin transduce pressure to give rise to the tactile sensations that constitute our sense of touch[1,2]. Although molecular mechanisms for mechanotransduction have been discovered using a variety of model organisms[4-9,13,14,19,66-68], the mechanisms underlying mechanosensation at the level of neuronal circuitry is not well understood. Because most genes and genetic mechanisms governing development are conserved from relatively simple animals to complex ones, *C. elegans,* a free-living nematode, is a suitable model organism to study developing nervous systems. *C. elegans* have a relatively short developmental period (3 days) and a stereotyped, well-cataloged development, with the development of all 302 neurons mapped

all the way from zygote to adult. The combination of easy genetic manipulation and optical transparency of the worm allows for non-intrusive *in vivo* imaging of neuronal activity. In addition, *C. elegans* exhibits sleep-like states (lethargus) during developmental stages which show delayed or decreased avoidance behavior in response to both mechanical and chemical stimuli[96-98].

While previously developed systems have demonstrated the delivery of mechanical stimuli and observation of neuronal responses using a piezo-driven micro stylus[3,70], we have pioneered a device that can deliver stimuli with higher precision and throughput to adult worms compared than has been recorded using manual methods. To understand how the functional role of the nervous system changes during developmental stages at a single cell-level, we modified our microfluidic platform.

However, designing this device was not as simple as scaling down the existing chip. For instance, developing the highly-deformable actuated membrane structure proved to be difficult due to its low aspect compared to its adult counterpart, its low aspect is necessary to deliver stimuli to smaller, developing worms. Moreover, handling smaller worms is harder than large adult worms. Since the imaging channel of the device is only 10 microns wide for trials involving L2 stage worms to minimize movement, a small particle of dust can clog the device. While this seems insignificant, this is a serious practical problem and the cause of many delays during the course of our study.

In this chapter, we will show a series of automated microfluidic platforms that allow for *in vivo* functional imaging and highly controlled mechanical stimulation in worms, ranging from early larval to adult worms: this was not possible using conventional

methods. Our strategy overcomes the limitation of deformability of PDMS membranes, using a new device fabrication method. It also highly increases the throughput of experiments compared to conventional *in vivo* functional imaging platforms, by coupling it with an automation technique. With these newly developed devices, we were able to observe several phenomena in developing *C. elegans*. First, in comparing the response to mechanical stimuli during sleep and awake stages, worms have highly reduced neuronal activity in the lethargus state. Furthermore, as early as the L2 stage, gentle and harsh touch receptor neurons can distinguish the magnitude of applied stimuli. Lastly, we show that high stimuli frequency evokes larger responses in touch receptor neurons than low frequency producing same or smaller indentation.

3.2 Method

3.2.1 Strains

C. elegans were maintained under standard conditions and fed OP 50 bacteria[79]. The following strains were used in this study:

AQ3236 *ljIs142[mec-4::GCaMP6m::SL2TagRFP, unc-119] II; unc-119(ed3) III*

TV17924 *wyls5007[ser2prom3::GCaMP6, egl-17::mCherry] X*

CX10979 *kyEx2865[sra-6::GCaMP3, Pofm-1::GFP]*

GT243 *aEx2[pglr-1::GCaMP6(s), punc-122::GFP]*

RW1596 *stEx30[myo-3p::GFP + rol-6(su1006)]*

A hatch-off procedure was used to synchronize larvae[99]. Briefly, adult hermaphrodites laid eggs overnight at 20 ℃ on NGM plates. Hatched larvae and adult were washed off three times with M9 and remaining embryos hatched at 20 ℃ for only 1 hour. Hatched L1 larvae were washed off and transferred to new NGM plates.

3.2.2 Chip Design and Fabrication

The device consists of worm inlet/outlet, an imaging channel (10 ~ 25 μm width and deep), and four sets of actuated PDMS membranes. Animals loosely fit in the channel, and are trapped (but not held) in the imaging area by two sets of actuated membranes. The width of the actuated PDMS membrane is 25 μm, the distance between the first and second sets of membrane is 50 ~ 75 μm and the distance between the second and third sets of membrane is 250 μm.

To create the easily actuated PDMS structure to touch and trap worms, a 30:1 ratio of PDMS monomer and curing agent was deposited via spin coating to create a thin layer for the bottom flow layer of features. Separately, 10:1 PDMS was directly poured onto a blank master, which did not have any features, to create a thick and mechanically rigid handle layer. Both layers were then placed into a 90°C oven for 25-30 minutes until both PDMS layers were rigid but sticky. After they were manually aligned, additional 10:1 PDMS was poured and cured for several hours to create a rigid handling layer for the device and then it was placed into a 90°C oven for overnight.

After curing, PDMS devices were cut to size, and features were created by puncturing the cured PDMS with sharpened gauge needles (18 gauge needles were used for worm in/outlet; 19 gauge ones were used for valves). The prepared devices were then cleaned with scotch tape and exposure to air plasma for 15 seconds before being placed and covalently bonded to a glass surface to create closed channels. Right after this bonding procedure, the devices were placed on top of a 150 ℃ hot plate as a treatment method to increase the adhesion between PDMS and the cover glass.

3.2.3 Calcium Imaging

All imaging experiments were performed on a Leica DMIRB inverted microscope using a 40x air objective (N.A. 0.75). Video sequences were captured using a Hamamatsu EM-CCD camera with 100 ms exposure time. Simultaneous two-color imaging was performed using a DV2 beamsplitter (Photometrics) containing a GFP/RFP filter set. Excitation light for fluorescent imaging was delivered through a projector system previously developed[83]. In experiments for the measurement of mechanosensory neuronal responses, stimuli were delivered 10 s after recording baseline activity of neurons. Videos were recorded for 60-180 s following stimulus delivery.

3.2.4 Data Analysis

Fluorescence intensities for each frame were extracted using a customized neuron-tracking MATLAB script (Chapter 2). In strains where both GCaMP6 and RFP are

expressed, the ratio between intensity values were computed ($R = \frac{I_{G\_ROI}}{I_{R\_ROI}}$) in order to minimize movement artifacts. When only GCaMP was available, fluorescence values were computed by subtracting background intensity ($F = I_{G\_ROI} - I_{G_{Back}}$). GCaMP and RFP intensities were measured as the mean pixel intensity of the 25 brightest pixels of a circular region of interest (ROI) of 5 pixel radius. Background intensities were subtracted to adjust for variations in lighting conditions, and were measured as the mean pixel intensity of an ROI in a background region. Calcium traces were computed as the change in R or F from the baseline value ($\frac{\Delta R}{R_o} = \frac{R - R_o}{R_o}$) or ($\frac{\Delta F}{F_o} = \frac{F - F_o}{F_o}$) . Baseline values were computed as the mean R or F prior to stimulus delivery.

3.3 New device design and fabrication method for the study of mechanosensation in *C. elegans* larvae

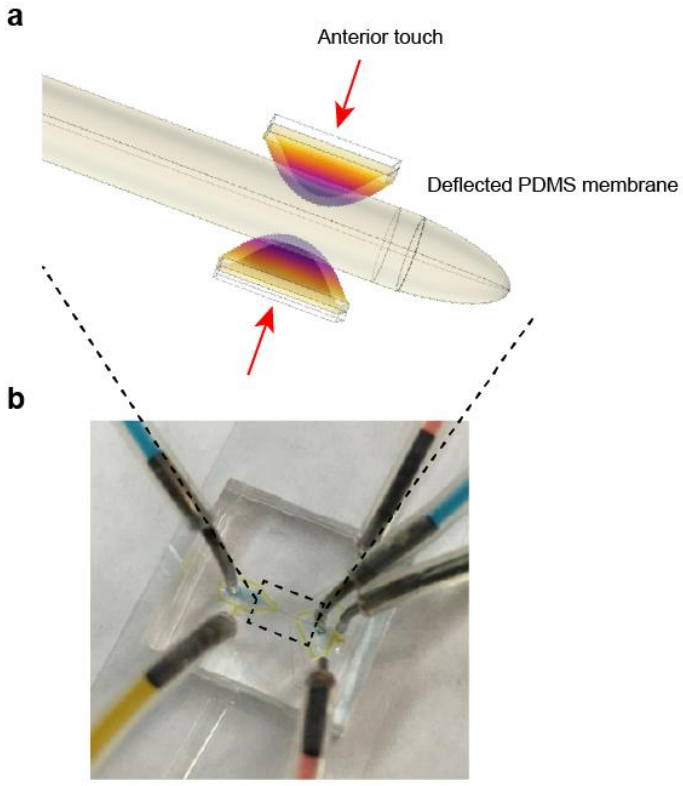

Figure 3. 1 Schematic of microfluidic device for high-throughput *in vivo* functional imaging to mechanical stimulation in developing worms. **a**) In the imaging channel, specific region of worm body (in this case, anterior region) can be stimulated by deflected PDMS membrane. **b**) The device is composed of the imaging channel for worms (which allows the animals to fit loosely inside, blue), two sets of actuated membrane (red), and two sets of trapping valves (yellow). All actuated valves are connected to a pressure source via individually controlled off-chip solenoid valves, allowing for an automated and rapid operation with a custom MATLAB script.

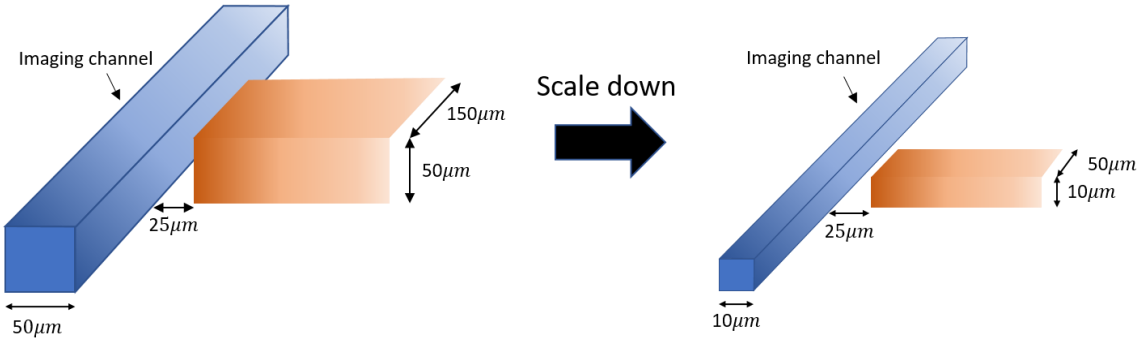

Figure 3. 2 A key engineering challenge is a scaling-down of the developed device from Chapter 2 to match the size of imaging channel to the size of developing worms. All scales have to be scaled down except the thickness of PDMS membrane (25 μm). The dimension of membrane is 10, 50, and 25 μm as height, width, and thickness, respectively.

We developed a series of unique devices that deliver precise and robust mechanical stimuli to different anatomical regions, such as anterior and posterior regions, in various developing stages (Figure 3.1). The overall design is similar to our previous device (Chapter 2), but the dimensions of the structures are optimized for the size of developing worm larvae (Figure 3.1). Scaling down the adult sized platform for L2 stage worms has complications. For adult worms, the channel width is about 50 - 60 μm, while for L2 it is 10 μm wide. Since each mechanosensory neuron has distinct receptive fields, it is important to deliver accurate and precise mechanical stimulation to specific region of the body to activate target neurons. For example, the receptive field of the AVM and ALML/R corresponds roughly to the anterior part of the body between the pharynx and the vulva[19,27]. For the delivery of a more precise stimulation to small worms, the width of actuated PDMS valves was reduced to 50 μm (from 150 μm for adult worms). However, the thickness of the membrane had to be kept the same as the device for adult worms to maintain a high success rate in bonding. As a result, the aspect ratio of the width and height to thickness of

the actuators was dramatically reduced. This made the membranes less deformable (Figure 3.2 and 3.5b).

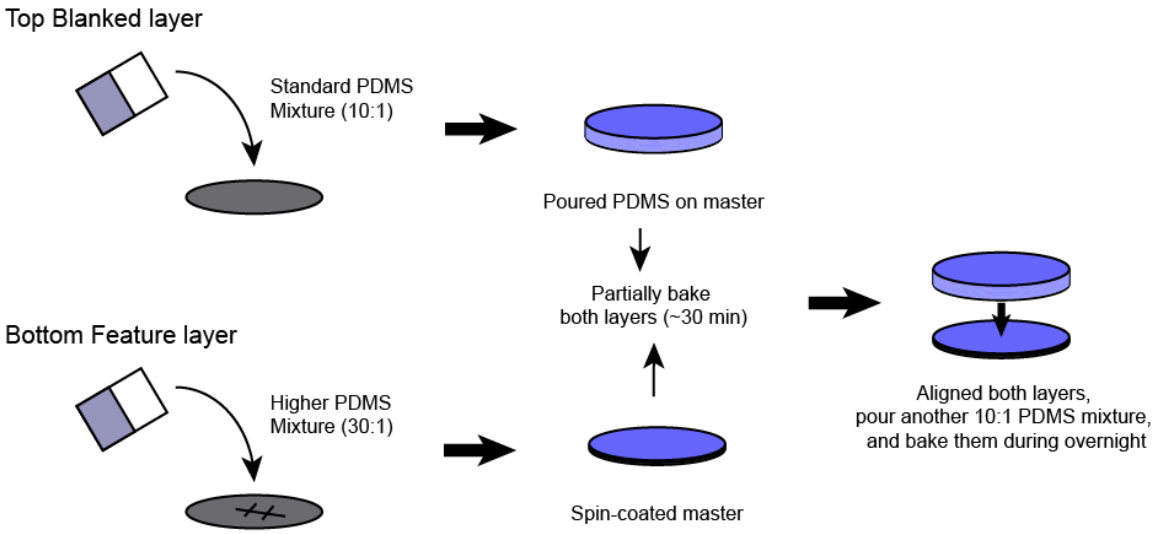

Figure 3. 3 The 30:1 ratio of PDMS monomer and curing agent was deposited via spin coating to create a thin layer for the bottom flow layer of features (5s ramping time and 1000 rpm for 30s). Separately, 10:1 PDMS was poured onto a blank master (Top blank layer), which does not have any features, to create a thick and mechanically rigid handle layer. Both layers were then placed into a 90°C oven for 25-30 minutes until both PDMS layers were rigid but sticky and then the top blank layer was peeled off from the master and then manually aligned to spin-coated layer. Additional 10:1 PDMS was poured and cured for several hours to create a rigid handling layer for the device.

The device requires a large range of possible deformability with low pressure and high reliability of deformation. Therefore, a higher ratio of PDMS to cross-linker, 30:1, is used for the feature layer, and a standard ratio of PDMS to cross-linker, 10:1, is used for the top “blank” layer which rests on top of the feature layer to increase the stability of the devices (Figure 3.3). Specifically, the high ratio PDMS mixture is spin-coated onto the

master wafer for uniform and consistent thickness. Separately, a "blank" layer, less than one centimeter thick, of 10:1 PDMS polymer is poured on a blank wafer, and both are cured for ~30 minutes at 95 °C: enough to make them solid, but not fully baked. The "blank" layer is then cut out and placed on top of the 30:1 PDMS membrane, increasing its stability. Using two separate, solid layers is important in this process, as the cross-linker can permeate from one layer to another in the liquid form, thereby reducing the ratio of PDMS to cross-linker and increasing the rigidity of the device. More 10:1 PDMS mixture is then poured around the "blank" layer to make the device easier to handle (Figure 3.3). The device is then cured, cut, and bonded to a cover glass slide where it is heat-treated at 150 °C for an additional 3 minutes. This procedure works well because the heat treatment can enhance the bonding affinity between PDMS and a cover glass substrate which is important when using such high pressures[70].

In addition, all actuated valves are connected to a pressure source via individually controlled off-chip solenoid valves, allowing for an automated and rapid operation with a custom MATLAB script (Figure 3.4). Because loading our device can be done for a batch of worms with only simple preparation techniques (mainly washing), throughput is mostly dependent on the length of the assay. Experimental times range from several seconds to a few minutes depending on experimental purpose, after which worms can be flushed and a new worm can be loaded in under few seconds easily. Therefore, up to ~100 worms/hour can be assayed in this new platform.

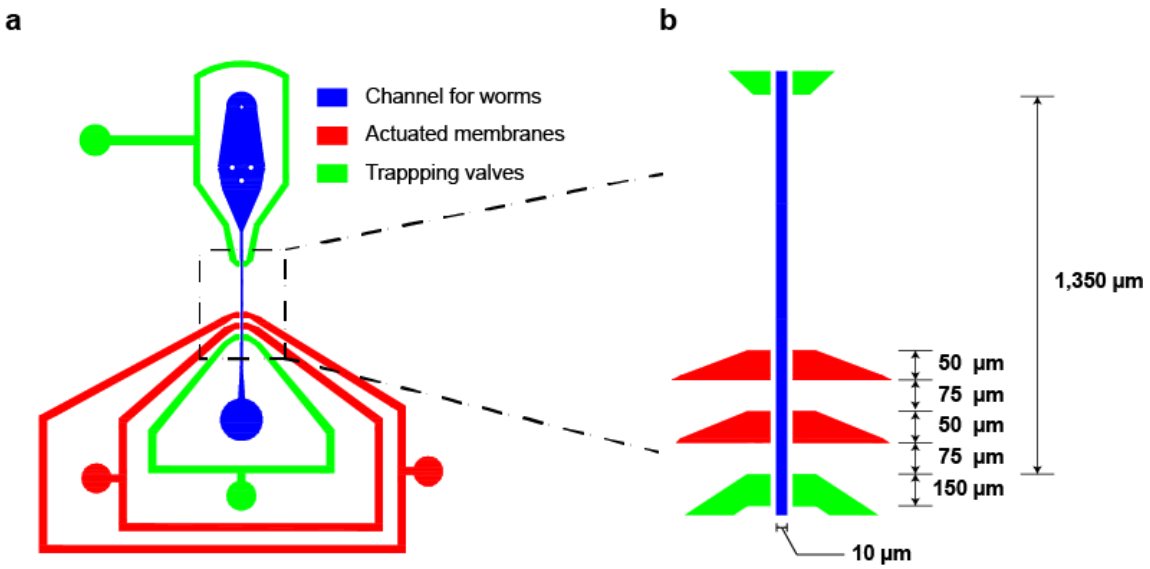

Figure 3. 4 Overview of microfluidic device dimensions for L2 imaging. The overall design of device is similar to device of Chapter 2. The device is composed of the channel for worms (10 µm deep and wide which allow the animals to fit loosely inside), two sets of actuated membrane, and two sets of trapping valve. The width of the both of actuated PDMS membrane (red) is 50 µm. On the other hand, the width of both of trapping valves is 150 µm, the distance between first and second sets of membrane is 75 µm and second and third sets of membrane is also 75 µm.

3.4 Device characterization

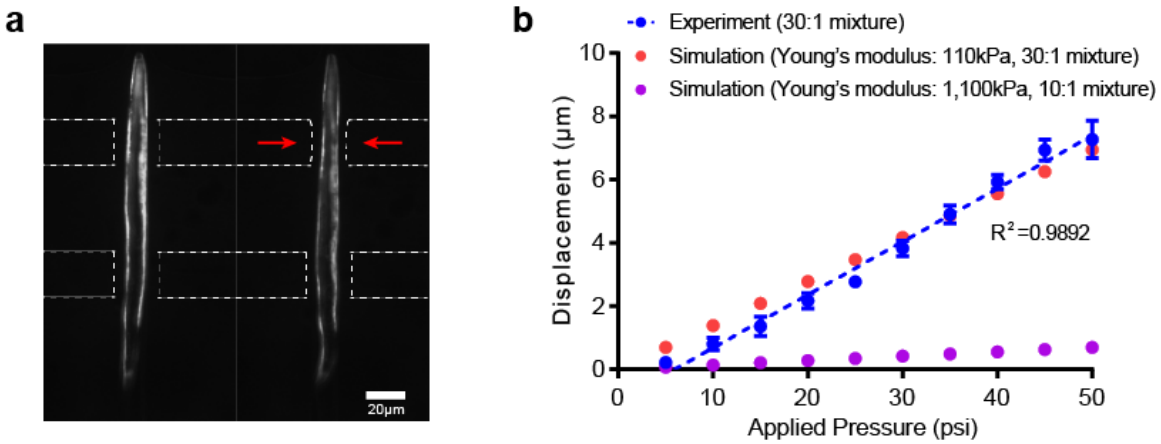

Figure 3. 5 The deformation in *C. elegans* tissue by using pneumatically actuated PDMS structures is linear to the actuation pressure. **a**) Example images of worms in the device. (Left) No pressured applied. (Right) 25 psi applied by using anterior touch valve (Red arrows). White dashed lines indicate the location of PDMS structure. Worms are cultured 20 hours after hatch. 10μm imaging channel device. **b**) Displacement of the actuated membrane by applying pressure. Blue represents experimental measurements. Red and purple represent simulation results by COMSOL Multiphysics. (Young' modulus - Red (30:1 PDMS mixture used in this study: 110kPa) and Purple (10:1 standard PDMS mixture: 1100kPa))[100].

As the results of the new fabrication technique, the PDMS membrane can be extensively deformed in relatively lower pressure range than in the previously discussed platform[101]. To examine the reproducibility and robustness of membrane deformation, we measured its displacement by taking images of transgenic worms expressing GFP along the body-wall muscle in our device with various applied pressure (Figure 3.5a). This means that the displacement measurements were based directly on the deformation in the animal's body, not on membrane deflection; this ensures that the correlations we make from the experiments are between neuronal signals and mechanical deformation/indentations of the body, as traditional mechanosensation assays on glued worms do. For example, compared to an unstimulated worm (left panel of Figure 3.5a), we can observe the indentation of a specific region of the worm body (red arrows in right panel of Figure 3.5a), when 25 psi is applied on the anterior touch valve. The experimental measurement shows that the deformation in the animal tissue is linear with actuation pressure (Figure 3.5b). This was also observed in the finite element analysis (COMSOL Multiphysics) that showed a similar trend between pressure applied and displacement of the PDMS membrane (Figure 3.5b and Figure 3.6). Not surprisingly, in contrast to the soft PDMS, when the standard ratio of PDMS mixture (10:1 ratio, Young's modulus: 1,100kPa[100]) is used, simulations suggest

that the PDMS membrane is not well deformed even in high pressure regime (Figure 3.5b), which is consistent with our experimental observation.

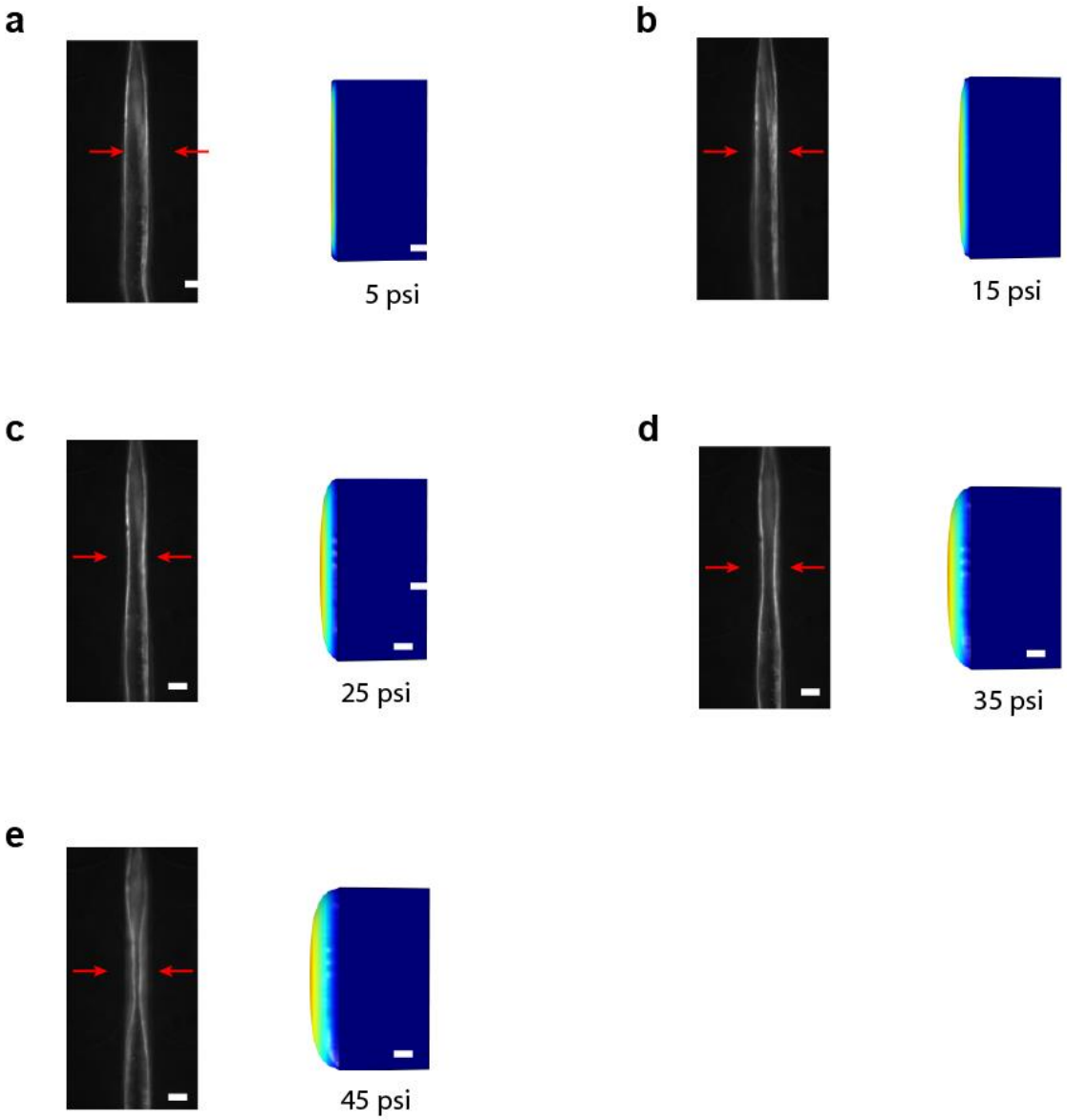

Figure 3. 6 The shape of deflected PDMS membrane by applied various pressure from 5 to 45 psi in experimental measurement (left) and simulation results (right). Scale bar: 5um

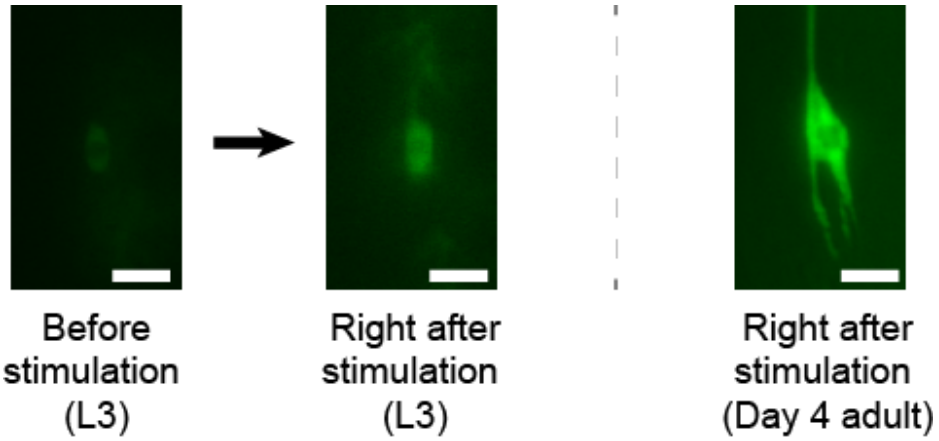

Figure 3. 7 Sample frames from activated neurons at different ages show changes in fluorescence due to mechanical stimulus. (Left) ALM neuron (30h after hatch) before the stimulation. (Middle) Activated ALM neuron (30h after hatch) after the stimulation. (Right) Activated ALM neuron (Day 4 adult) after the stimulation. (Scale bar: 5μm)

Another important advantage of our device is that worms' neurons can be easily imaged and tracked due to the limited movement in the channel (Figure 3.7). The size of the imaging channel and trapping valves can minimize the movement of worms, allowing high-quality calcium imaging without using any immobilization technique (Figure 3.7). However, this requires that we perfect the devices to fit the worms snugly at the specific development times of interest. Because we want to image worms at several major stages of their lives, devices ranging from 10 μm to 25 μm wide were created. Development times were optimized to minimize movement within the channel. These results are in Table 3.1 which shows the ideal developmental time, in hours, for each of our device sizes.

Channel Width	10 μm	15 μm	20 μm	25 μm
After Hatch Time (h)	18 - 24h (20 °C)	28 - 34h (20 °C)	38 - 42h (20 °C)	46 - 50h (20 C)

Table 3. 1 Development times were optimized for minimal movement within the channel. This table shows the ideal developmental time, in hours, for each of our device sizes.

3.5 Modulated neuronal responses between awake and lethargus stages

C. elegans experiences a sleep-like stage called the lethargus state[96]. The expected duration and placement of these states in the worm's life are well documented, which generally last around an hour at the completion of and transition to a new larval stage. Worms in this lethargus state can be observed to have drastically reduced behavioral and neural activity as well as reduced responsiveness to stimulation[96,98,102]. To examine neuronal activities in the lethargus states, we measured the responses of two sensory neurons, ALM and AVM, and the interneuron AVA to mechanical stimuli in L2 (18-22 hours after hatch) and L2 lethargus stages (24-25 hours after hatch). As before, by using a genetically encoded calcium indicator (GECIs), GCaMP6, we can monitor the change of calcium flux in specific neurons. In order to reduce stochastic effects on neuronal responses, we applied strong mechanical stimuli to anterior region and recorded neuronal responses (Figure 3.8a-c). As seen in Figure 3.8, almost no response is elicited in lethargus worms, even at extremely large stimulation; in contrast, the response is clear in awake worms. This behavior is seen in both gentle touch neurons, ALM and AVM, along with the interneuron, AVA (Figure 3.8d). Therefore, the calcium imaging data suggest that there

are fewer calcium channels open, and thus the same stimulus is less able to excite mechanosensory neurons during lethargus.

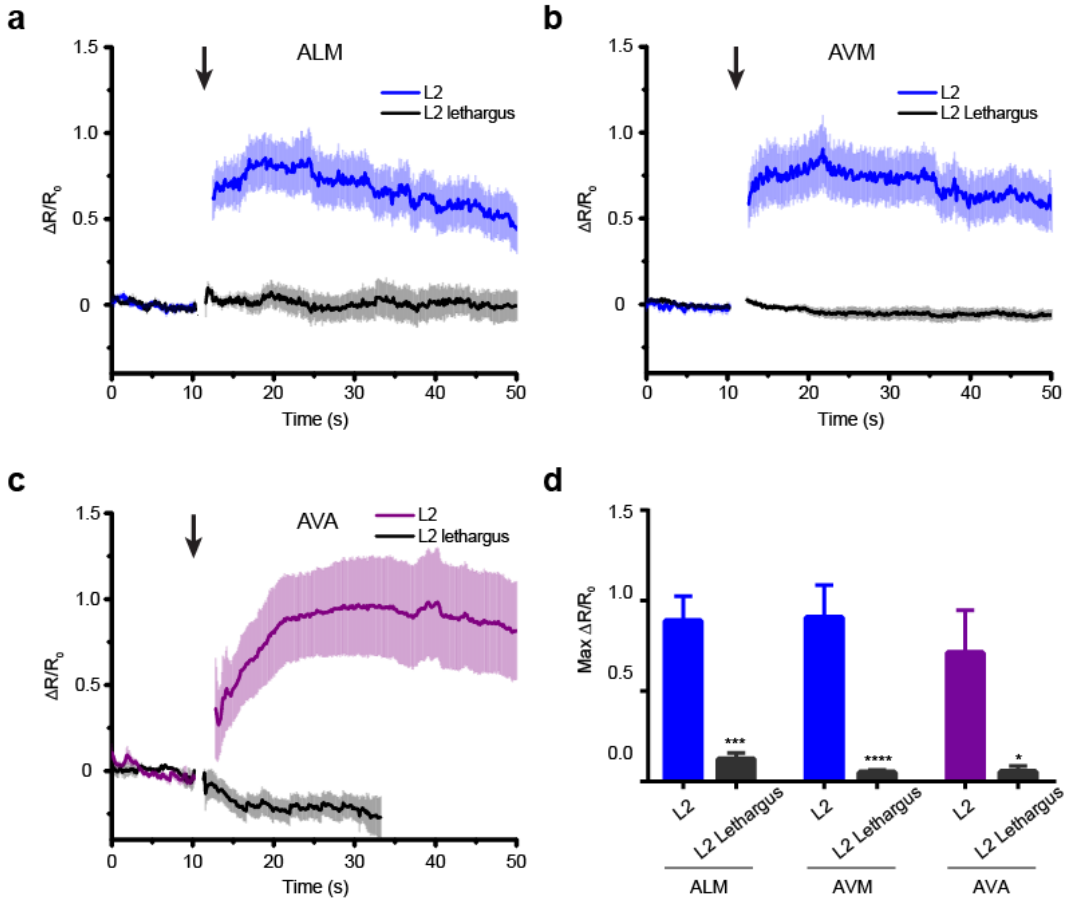

Figure 3. 8 Worms in L2 lethargus state show drastically reduced neural responsiveness to mechanical stimulation. **a**) Average traces of calcium responses of L2 and L2 lethargus worms in ALM to 1s anterior touch with 50 psi. (L2: n=19, L2 lethargus: n=9). **b**) Average traces of calcium responses of L2 and L2 lethargus worms in AVM to 1s anterior touch with 50 psi. (L2: n=19, L2 lethargus: n=15). **c**) Average traces of calcium responses of L2 and L2 lethargus worms in AVA to 1s anterior touch with 50 psi. (L2: n=7, L2 lethargus: n=5). **d**) I: Maximum calcium responses of L2 and L2 lethargus worms (Mann-Whiteny Test, *p<0.05, **p<0.01, ***p<0.001, ****p<0.001). **a-d**) All worms in this experiments are cultured either for 18-20h for L2 or 24-25h for L2 lethargus. Error bars represent SEM.

3.6 Touch receptor neurons in developing stages can distinguish the change of magnitude of applied pressure, like adult worms

We next asked how the functional role of touch receptor neurons changes during development. In a previous study, we observed that both gentle and harsh touch receptor neurons clearly distinguished a change in magnitude of applied mechanical stimulation. To examine whether we can observe this phenomenon in developing worms, we measured the responses of the classic gentle (AVM, ALML/R, PVM, and PLML/R) and harsh touch (PVD) receptor neurons in L2 stage worms (Figure 3.9 and Figure 3.10). Since the critical parameter in mechanosensory stimulation is displacement, not force[70], the linearly controlled displacement of the PDMS membrane by applied pressure in our system can easily distinguish between gentle and harsh touch stimuli (Figure 3.9 and Figure 3.10). We applied anterior stimuli of varying levels of pressure and durations, and measured calcium activity of ALM neuron in L2 stage (18-22 hours after hatch) (Figure 3.9a and Figure 3.10a). The maximum calcium transient peaks in ALM neurons are proportional to the magnitude of applied pressure (Figure 3.9a and C, and Figure 3.10a and c). Similarly, in the harsh touch regime, we delivered posterior stimuli of varying pressure and durations, and observed responses in PVD neurons in L2 larvae stage (Figure 3.9b and Figure 3.10b). As expected, compared to gentle touch neurons, such as ALM, PVD required longer duration of stimulus (1s) at low pressure (35 psi) or high pressure (45 psi) to elicit neuronal responses (Figure 3.9b and c, and Figure 3.10b and c). On the other hand, PVD shows negligible response to stimulation in the gentle touch regime, such as 25 psi (with 1s stimulation) and 35 psi (with 200ms stimulation), which both activate ALM neurons (Figure 3.9b and C, and Figure 3.10b and c). It is consistent with previous observation in

adult worms that gentle and harsh touch neuron can distinguish the magnitude and duration of the applied pressure[102].

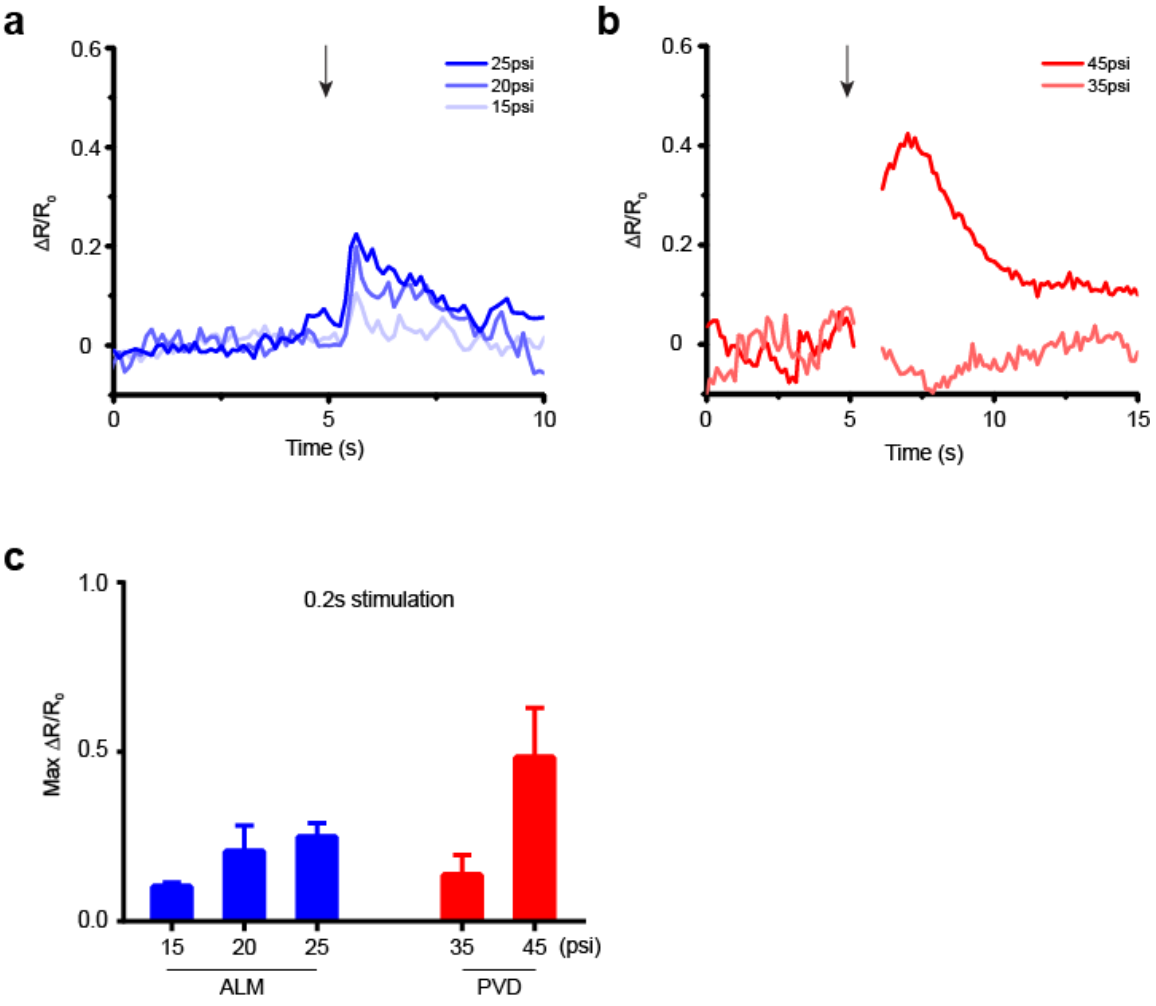

Figure 3. 9 **a**) Average traces of calcium signals in ALM in response to anterior touch with 200ms and diverse pressure. (15 psi: n=6, 20 psi: n=6, 25psi: n=8). **b**) Average traces of calcium signals in PVD in response to posterior touch with 200ms and diverse pressure. (35 psi: n=4, 45 psi: n=5). **c**) Average traces of calcium signals in ALM in response to anterior touch with 1s and diverse pressure. (15 psi: n=9, 20 psi: n=7, 25psi: n=10)

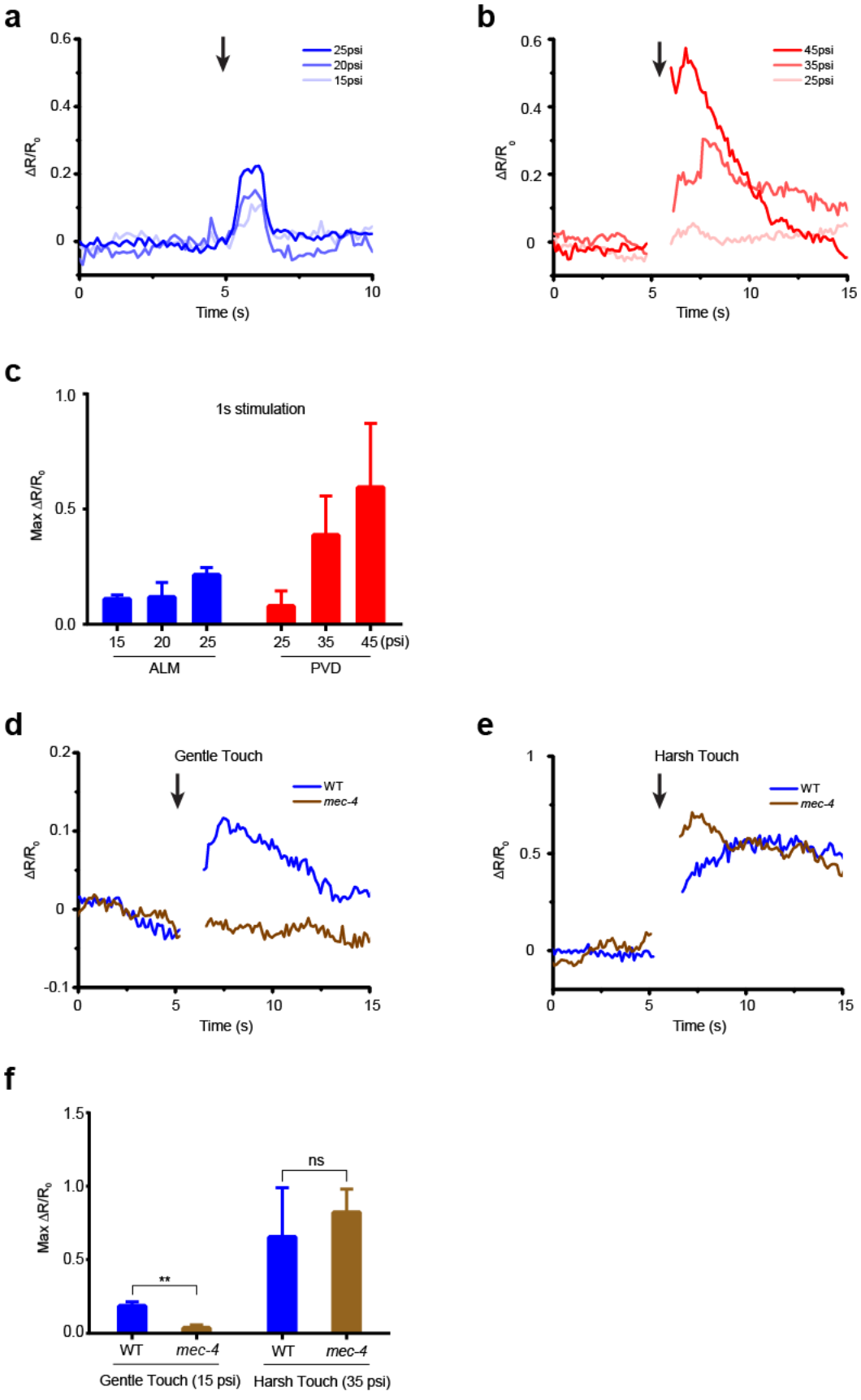
a
25psi
20psi
15psi
ΔR/R0
Time (s)
b
45psi
35psi
25psi
ΔR/R0
Time (s)
c
1s stimulation
Max ΔR/R0
15 20 25 25 35 45 (psi)
ALM
PVD
d
Gentle Touch
WT
mec-4
ΔR/R0
Time (s)
e
Harsh Touch
WT
mec-4
ΔR/R0
Time (s)
f
Max ΔR/R0
**
ns
WT
mec-4
WT
mec-4
Gentle Touch (15 psi)
Harsh Touch (35 psi)

Figure 3. 10 Both gentle and harsh touch receptor neurons can distinguish the change of magnitude of applied mechanical stimulation. **a**) ALM responses to anterior touch with 1s and diverse pressure. (15 psi: n=9, 20 psi: n=7, 25psi: n=10). **b**) PVD responses to posterior touch with 1s and diverse pressure. (25psi: n=5, 35 psi: n=13, 45 psi: n=5). **c**) Maximum calcium responses of ALM and PVD to a variety of applied pressure. **d**) AVM responses of wild-type and *mec-4(e1611)* mutants to anterior gentle touch (1s and 15 psi, WT: n=11, mec-4: n=7). **e**) AVM responses of wild-type and *mec-4(e1611)* mutants to anterior harsh touch (1s and 35psi, WT: n=7, mec-4: n=5). **f**) Maximum calcium responses of wild-type and mec-4 mutant animals (Mann-Whiteny Test, *p<0.05,**p<0.01). (A-F) All worms in these experiments are cultured 28-30h after hatch.

To verify the ability of our device to deliver two distinct types of touch stimuli, gentle and harsh, we also measured the AVM neuron's responses in a gentle touch-insensitive mutant, *mec-4 (e1611)*, to provoke stimulation in both the gentle and harsh touch regimes (Figure 3.10d - f). The mec-4/DEG/ENaC channel mutant affects only gentle touch sensation[3]. As expected, although insensitive to gentle touch stimulation (anterior touch with 1s and 15 psi), the *mec-4* mutant was responsive to harsh touch stimulation (anterior touch with 1s and 35 psi) (Figure 3.10d - f). Compared to the activity of the AVM neuron in wild-type animals, *mec-4* mutants show significantly reduced neuronal responses to gentle touch stimulations, but not harsh touch ones (Figure 3.10f). This demonstrates the ability of our platform to activate distinct types of mechanosensory neurons, gentle and harsh touch neurons, by simply changing the magnitude of applied pressure in our system.

3.7 The activity of GTNs in developing stages are affected by the rate of mechanical stimulation

In a previous study, Eastwood *et al*. found that fast frequency of mechanical stimuli can evoke larger currents of mechanoelectrical transduction channels than slower frequency of stimuli, even though faster stimuli produced the same or smaller indentations[70]. We asked whether this phenomenon occurs during larval stages in our system and how the sensitivity of mechanosensory neurons changes during development. We used a device for L2 stage imaging (10um width channel) and measured the speed of membrane deflection under a high-speed camera, varying the rate of mechanical stimulation. It required 0.03s for full expansion of membrane at 35 psi. We applied various stimulus frequencies from 1 Hz to 15 Hz (50 % duty cycle) for 2s to the anterior region and measured ALM neuronal responses at L2 stages (18-22 hours after hatch). At low frequencies, the membrane can expand fully, displaced the same as at single pulse stimulation; at higher frequency, the membrane did not fully expand (Figure 3.11), similar to how a stylus might work as in Eastwood *et al*[70]. Interestingly, up to a frequency of 5 Hz, ALM neurons show similar magnitude of calcium responses; in contrast, at high frequency (7 or 15 Hz), even with the smaller displacement of membrane, a higher and more robust neuronal responses was evoked (Figure 3.11). These results are consistent with the observation that neuronal sensitivity is increased at high frequency in adult worms. Therefore, this device allows us to explore whether the entire mechanical sensory system behaves more like a high-pass or band-pass mechanical filter.

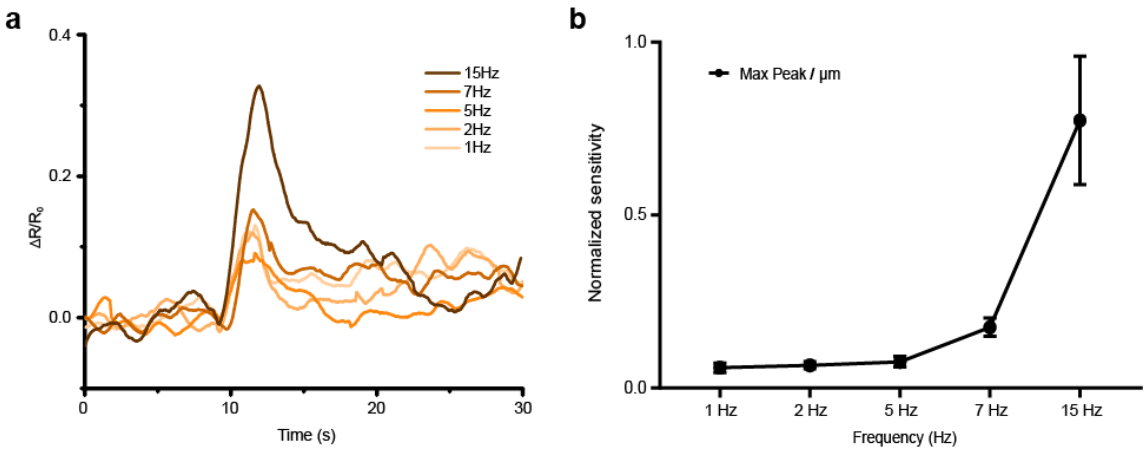

Figure 3. 11 *C. elegans* touch receptor neuron in L2 stage is sensitive to stimulus frequency. **a**) Average traces of calcium responses of L2 worms in ALM to a variety of frequency stimulations. At high frequency (15 Hz), smaller displacement of membrane evoked a higher and robust neuronal responses. **b**) Sensitivity of ALM neuron in L2 stage as a function of stimulus frequency. Sensitivity is defined as the peak amplitude of calcium traces divided by the applied indentation achieved at the frequency. (1Hz: n=9, 2Hz: n=8, 5Hz: n=20, 7Hz: n=10, 15Hz: n=9). **a-b**) All worms in these experiments are cultured 28-30h after hatch.

3.8 Conclusions

High-throughput *in vivo* functional imaging platforms for developing nervous systems will allow for fundamental studies of brain development. However, *in vivo* functional imaging of *C. elegans* in early larval stages is currently impossible, because conventional methods do not allow for the level of functional imaging precision that is needed. We have developed a range of microfluidic platforms that allow for precise, quick interrogation of mechanosensation in *C. elegans*, at several stages of life, ranging from early larval stages to late adult life.

All animals must sleep to survive. The importance of sleep and its effects on development, memory formation, and even neural disease are becoming more and more known. However, much about sleep is still not understood. Studying animals that have sleep like states can be useful in dissecting its impact on neuronal health. *C. elegans* has been shown to experience a state analogous to sleep between each larval stage characterized by reduced physical and neuronal activity. As seen in Figure 3, *C. elegans* has a drastic change in mechanosensory response during these periods. While this phenomenon has been observed before, our data verifies the accuracy with which our device works. Much more detailed and thorough studies can be conducted, including drug screens or molecular level studies, with confidence that our new device obtains accurate data. Beginning to understand the functional activity of the brain during sleep starts with understanding sleep-like states in model organisms.

Our microfluidic platforms facilitate the study of mechanosensation in developing worms quantitatively and conveniently with the ease of delivering a variety of types of mechanical stimuli to different regions of the worm body. Moreover, our immobilization technique is done through physical restriction, rather than glue, which is a permanent and ultimately fatal technique, or immobilizing drugs, which have unknown effects on neuronal responses. These are substantial advantages over traditional techniques. With highly improved throughput and significant standardization compared to conventional methods, it is now possible to develop high-throughput assays that screen genes or drugs for their effects on neuronal activity involved in mechanosensory circuits. In addition, proving the effectiveness of a scaled-down version implies the possibility of scaling up this device to test higher order organisms, such as fruit flies and zebra fish.

CHAPTER 4. AN ANALYSIS TOOL FOR THE ASSESSMENT OF HEALTH AND LONGEVITY OF *C. ELEGANS*

4.1 Introduction

Human are living longer than ever due to the advances of modern medicine. As the population ages, it suffers from age-associated diseases such as cancer, neurodegenerative disorders, and cognitive decline. Aging had traditionally been thought of as the inevitable progress of decay and degeneration. However, this view has changed within the past few decades. Specifically, in 1993, Kenyon *et al*. demonstrated that worms mutant for one gene that encodes the insulin receptor can live two to three times longer than wild type worms[20]. Remarkably, flies and mice that have mutations in the insulin or the insulin like growth factor-1 receptor gene are also long-lived[103-106]. Separately, many researchers have found that a reduction in caloric intake could extend lifespan and delay disease onset in a wide range of species from worms, all the way up to monkeys[23,29,107-113]. These studies indicate that lifespan can be actively regulated by genetic, environmental, and pharmacological factors. In interesting application of this new paradigm, drugs such as rapamycin are being studied for their potential to enhance lifespan in organisms as complex as mice[114]. Yet, much of the molecular mechanisms of aging and regulation of age-related diseases are unknown; major questions such as whether organisms are extending healthy lifetimes or simply prolonging periods of frailty remains elusive.

C. elegans is an important model organism for the investigation of the aging process due to its relatively short lifespan. Furthermore, worms have been shown to have complex metrics of health that strongly resemble human health metrics, and change similarly with age[115]. Nevertheless, the current experimental techniques for aging assays in the worm have limitations: they lack fine control over environmental conditions, longitudinal tracking of individuals, high experimental temporal resolution, and large-scale experimentation. This is because, as described previously, conventional methods for lifespan assay in *C. elegans* have been limited by the available technologies. Conventional assays are conducted using small populations of animals on agar plates and scoring of longevity metrics or characterization of animal behavior is done by hand. Thus, lifespan assays have been labor-intensive, limited in scale, and usually cannot achieve single worm resolution. Moreover, the requirement for hand-annotation significantly limits the frequency of data collection.

In order to overcome technical limitations on frequent single-worm resolution, several specialized culture systems have been developed. For example, Yu *et al*. or Pincus *et al*. developed imaging systems based on multi-well or patterned hydrogels, respectively, that spatially confine individual worms for quantifying long-term behavioral phenotypes[48,50]. While these systems allow longitudinal imaging of individual worms via both spatial confinement and automated imaging, these platforms do not permit food exchange and thus limit the ability to finely control lifetime dietary level, which is a critical determinant of longevity[21,29,107,116]. Moreover, although the platforms lower the requirements of manual labor by automated imaging system, data acquisition still requires manual manipulation of the experimental setup and removal from environmentally controlled chambers such as

incubator. This can have unknown effects on results; for example, lower temperature have been linked to increased longevity in *C. elegans*[11]. Therefore, these systems are limited to infrequent data collection.

To address these time resolution of data collection and environmental control issues, Stroustrup *et al*. developed a scalable imaging platform using commercial scanners that can be integrated into temperature-controlled incubators[49,117]. The system automatically captures a time series of images of plates in sub-hourly resolution for the determination of a general time of death. However, the low spatiotemporal resolution of this system prevents identification of many behavior data that may be used as health indicators. In addition, this system does not support food exchange, so it lacks control over dietary levels.

Several microfluidic platforms have been demonstrated for use in developmental and lifespan assays that allow a high degree of environmental control[46,47,51]. These systems allow liquid culture of worms on device and have the advantage of continuous food exchange. However, these platforms do not have a temperature control system and are difficult to integrate with commercial temperature-controlled incubators. Moreover, these systems' automation has not been validated on a large scale, nor have they been shown to handle multiple simultaneous experiments. Furthermore, they have not shown any tracking of behavior longitudinally or analysis for healthspan assay. As a result, the data derived from these systems have been limited to demonstrating proof-of-concept.

In order to generate a lifetime record of individual behavior on a large scale and address the individual tracking issues, together with an alumna of the Lu Lab (Dr. Mei Zhan), I developed a platform that offers physical isolation of individual animals, high temporal

resolution of behavior tracking, and highly controlled environmental conditions such as temperature and food. In addition, since all modules of this platform are automatically controlled and provides automated data acquisition, this platform can greatly enhance the throughput of experiments and minimize variability compared to conventional assays conducted by hand.

Beyond the development of a platform for a longitudinal study, an important challenge in this work is to automatically analyze behavior and lifespan objectively to increase throughput. By developing an algorithm for automatic and quantitative behavior analysis, I can automatically recognize worms from video images and extract quantitative behavioral information. Moreover, since individual animals can be tracked in this platform, I evaluated the relationships between age-related behavioral changes and lifespan.

4.2 System overview

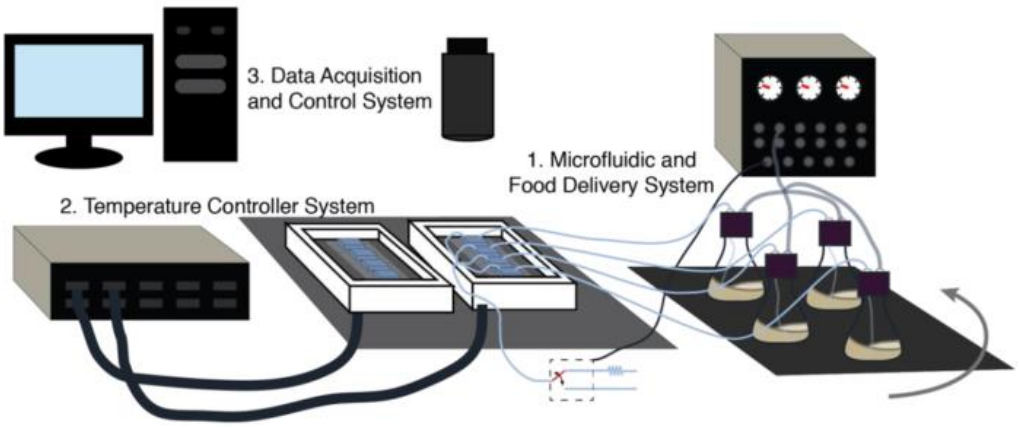

Figure 4. 1 Overview of long-term culture and data acquisition system. The entire system consists of three major submodules that enable control over two critical environmental variables and integrative control over data acquisition. (Image courtesy of Mei Zhan)

Figure 4.1 shows a scalable, high-throughput, automated long-term individual tracking platform integrated based on microfluidics with integrated computer hardware and software. This platform is composed of three major modules: a liquid worm culture system, a temperature controller, and an automated imaging system. The first module is the liquid worm culture system, which is comprised of both the microfluidic chip and the off-chip support system for food control and delivery (Figure. 4.2). It adapts the capabilities of the previously developed microfluidic device for long-term physical isolation of individual worms cultured on a chip[118] (Figure. 4.2a). This module provides a method for automatically loading, long-term encapsulation, food delivery, and spatially confining otherwise free-moving worms for observation (Figure. 4.2b, c).

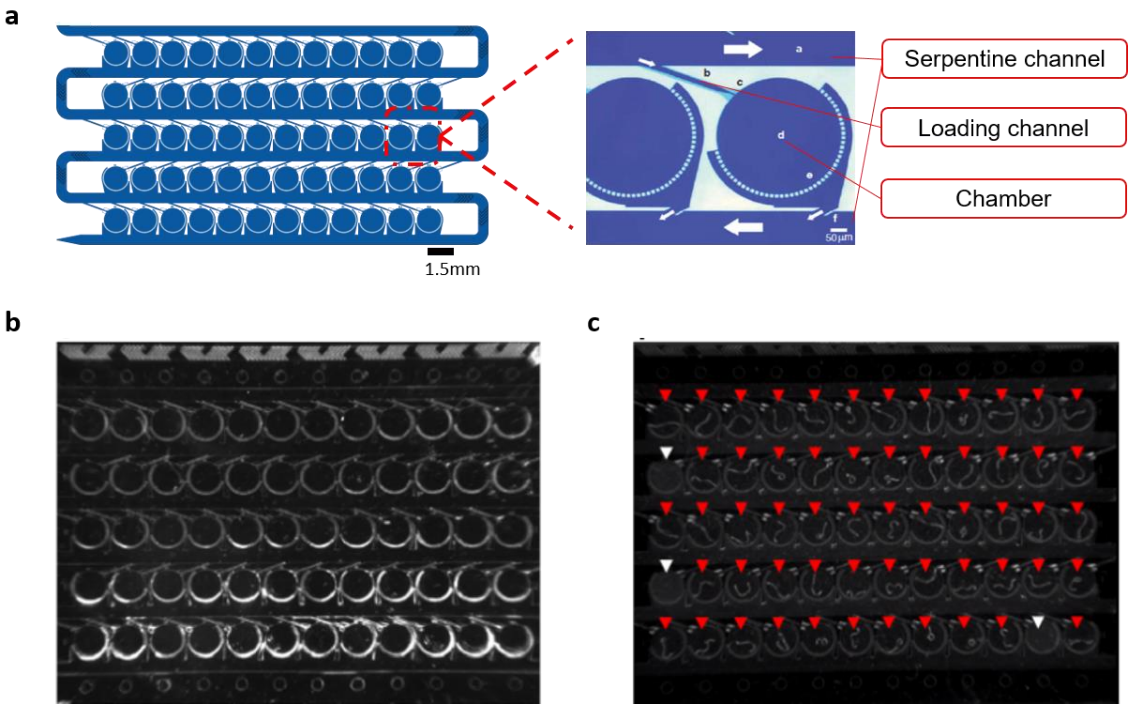

Figure 4. 2 Worm chamber array for long-term culture and observation of *C. elegans*. **a**) Overview of device showing 60 chambers arranged along a serpentine channel with a loading channel. **b**) Optical photographs before *C. elegans* loading in the device and **c**) after *C. elegans* loading in the circular chambers. Red arrows head, successfully loaded a single worm; white arrows head, empty chambers.

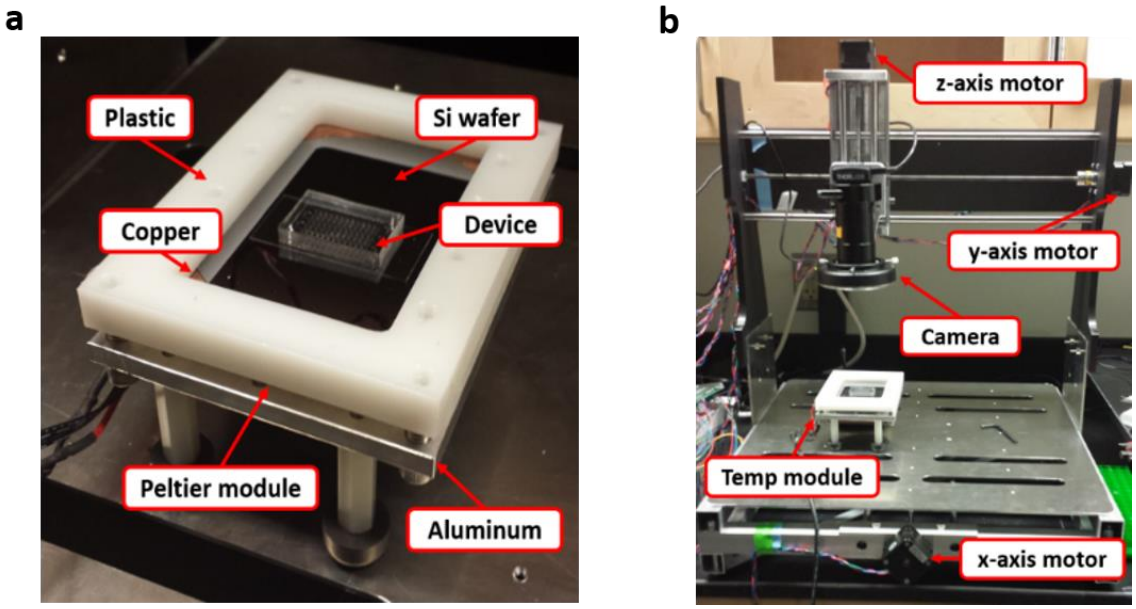

Figure 4. 3 Images for a temperature controller and automatic imaging setup. **a**) The temperature controller consists of a copper temperature distribution platform that is in thermal contact with an underlying Peltier module. The aluminum plate is used at the bottom of a Peltier module as a heat sink. In order to distribute waste heat more efficiently, a cooler is attached at the bottom of the aluminum plate. **b**) The imaging setup consists of three motors to automatically move the camera in the x, y, and z directions . Up to 8 temperature modules can be installed in this setup simultaneously.

The second module controls ambient temperature on a microfluidic chip (Figure 4.3a). When powered, the Peltier element heats or cools a copper platform, whose temperature is monitored by a sensor and reported back to the control unit. With the liquid worm culture system and temperature controllers, this platform can support up to 32 independent microfluidic chips, each housing up to 60 worms. These chips can each be operated via independent food delivery, allowing investigation of different food conditions simultaneously. Furthermore, the system supports 8 different temperature conditions.

The third module enables automated experimental control by interfacing with the first two modules as well as automated data acquisition via camera control and state movement. We modified a commercial kit for a home-build computer numerical control (CNC) machining plat-form to monitor multiple chips positioned atop temperature modules (Figure 4.3b). Together, these capabilities permit the tracking of behavioral health metrics and allows multidimensional and longitudinal assessment of health and longevity trajectories. For more detail information of the components of the platform and the protocol of experiment, I refer to Mei Zhan's Ph.D dissertation[119].

4.3 Validation of this platform for lifespan assay

Individual longevity of animals can be automatically monitored with sub-hourly experimental time resolution, i.e. system can capture two 10 second videos every hour. To validate the feasibility of life-long maintenance of *C. elegans* on our platform, the results of lifespan assays on chip were compared to previous studies[20,29]. Figure 4.4 shows example images of worms at a variety of food and health conditions. As worms died in the microfluidic device, they straightened out (left figure in Figure 4.4), making it easy to conduct live-dead assays by observing body postures. Thus, I counted the death of each worm when its body posture is straight and does not move through several sequential videos.

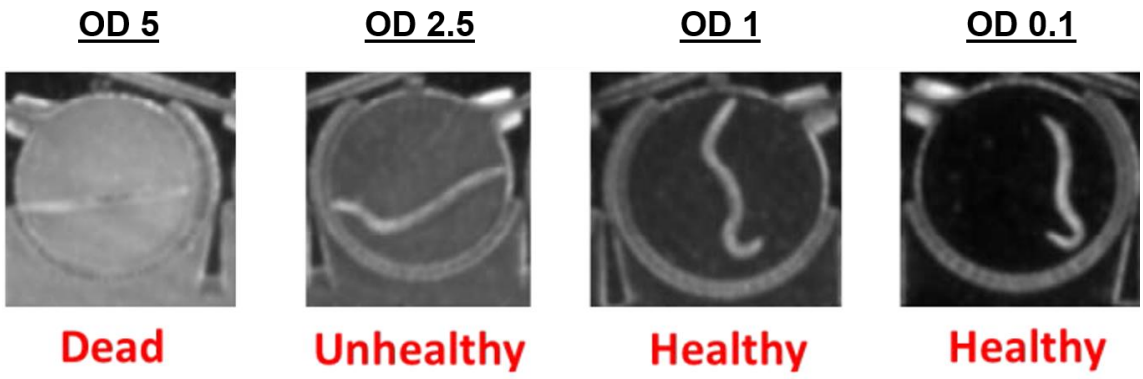

Figure 4. 4 Sample images of worms at day 23 with various food conditions (from left OD5, 2.5, 1, 0.1; unhealthy worm died next day).

4.3.1 Survival analysis: Kaplan-Meier Estimator

The Kaplan-Meier estimator is a useful method for determining how a treatment affects lifespan. The effect of an intervention is measured by assessing the number of subjects that survive over a given period of time[120,121]. It can provide an estimate of the survival function, S(t). It describes the fraction of individuals remaining alive at time t. I used the Kaplan-Meier estimator to measure the length of time that animals were surviving across different environmental conditions.

Figure 4.5 and 4.6 show the survival fraction of populations of worms on this platform at different food concentrations and temperature conditions. The results show that the platform is capable of sustaining worms throughout their lifespans and replicating well-documented longevity effects. For example, worms on the platform live longer in low temperature conditions than high temperature over various food conditions from OD5 to

OD0.1 (Figure 4.5). In addition, robust diet-induced lifespan extension can be observed on this platform (Figure 4.6). These observations are consistent with previous literature[29,49,122].

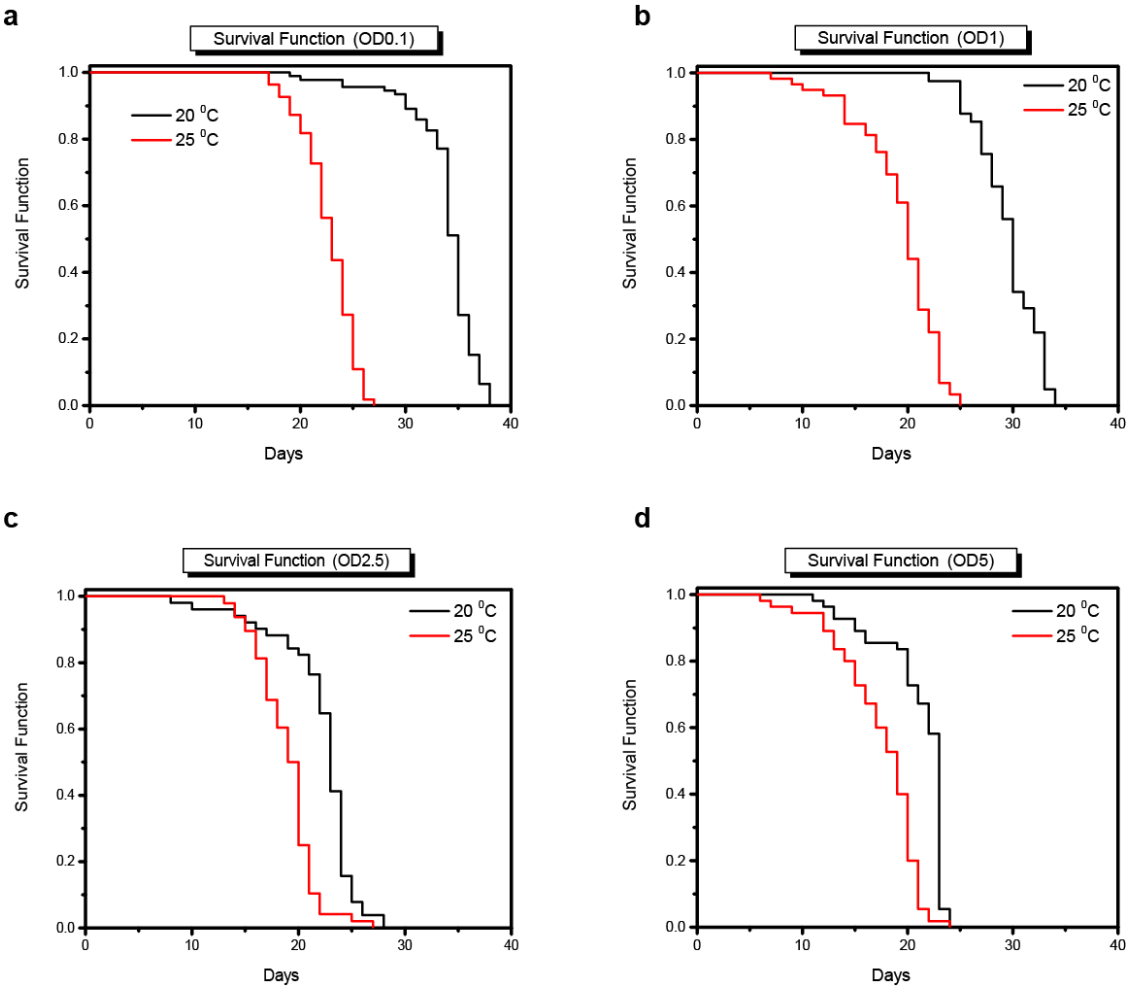

Figure 4. 5 Survival curves via Kaplan-Meier estimator at different food and temperature conditions. Survival curves show the surviving fraction of animals at different ages. Each condition is labeled in both the title and legends of figures. At an equivalent food level, worms at high temperature (25 ℃) died earlier than ones at low temperature (20 ℃).

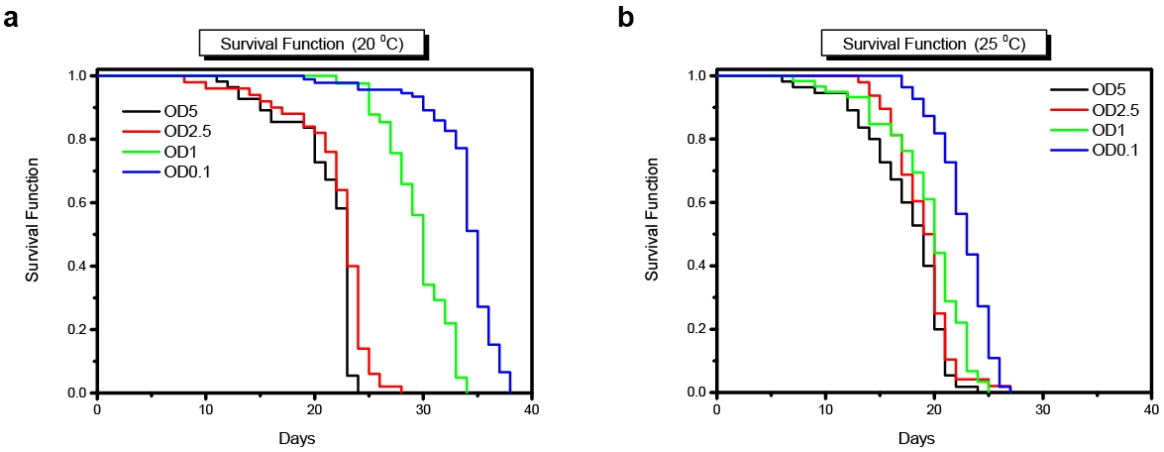

Figure 4. 6 Survival curves via the Kaplan-Meier estimator at different food and temperature conditions. Survival curves show the surviving fraction of animals at different ages. Each condition is labeled in both the title and legends of figures. At same temperature level, worms at high food condition (OD5) were dead earlier than ones at low food condition (OD0.1).

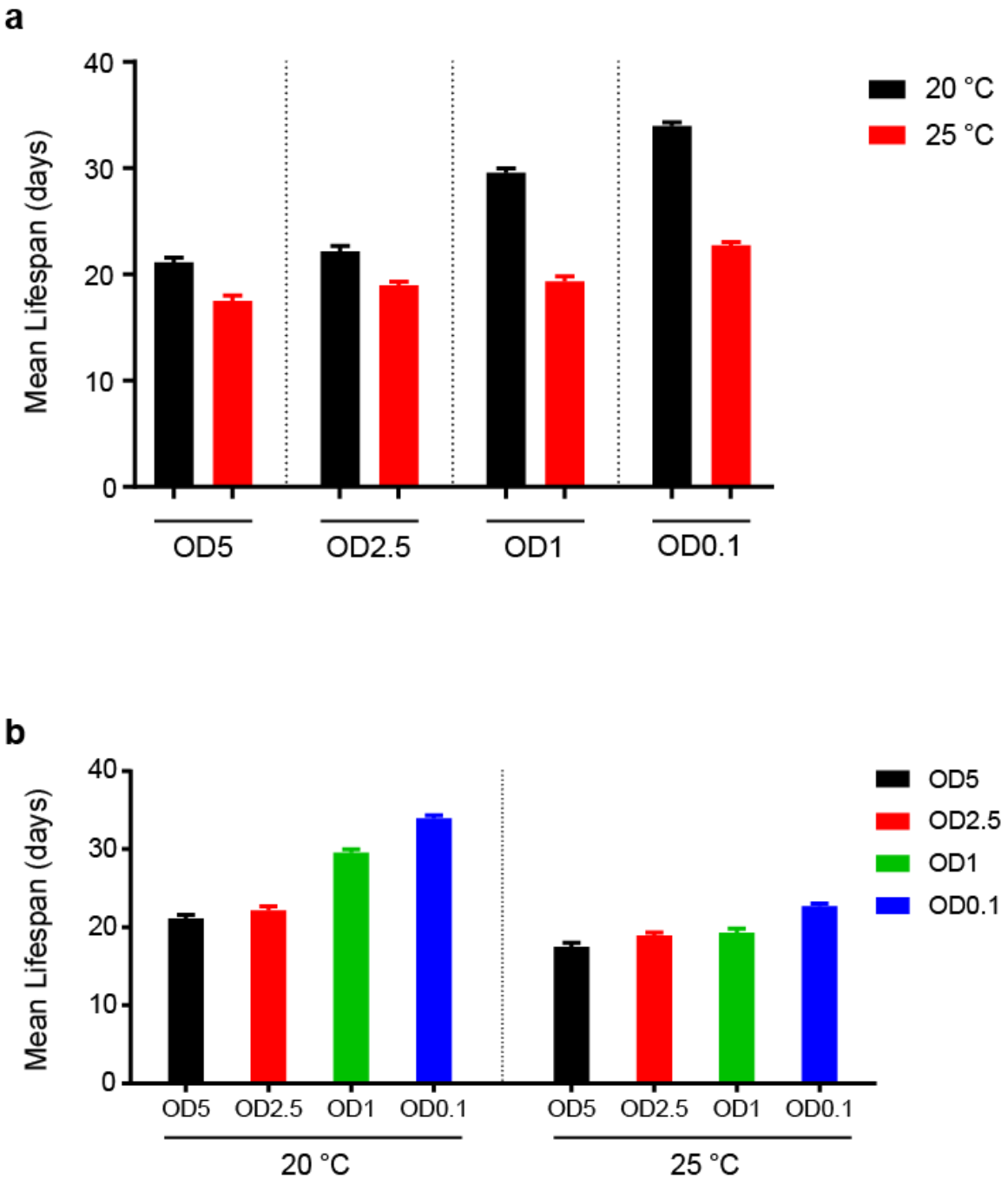

Figure 4. 7 Mean lifespan (days) and standard error of the mean (days) at different culture conditions. Plots show the effect of a) temperature levels and b) food concentrations on lifespan. Error bars indicate SEM.

4.3.2 Test of reproducibility of lifespan assay

To test the reproducibility of lifespan assays conducted on our platform, I recorded two worm populations over the worms' lifetime at the same conditions (20 ℃ and OD0.1). Figure 4.8 shows the results of these observations. The mean lifespan of population 1 is 33.60 ± 0.45 days and population 2 is 34.30 ± 0.56 days. Comparisons and P-value calculations were made between the two trials using the Breslow test (p=0.1363). This result suggests a good reproducibility and a high level of control over environmental conditions for lifespan experiments on our platform.

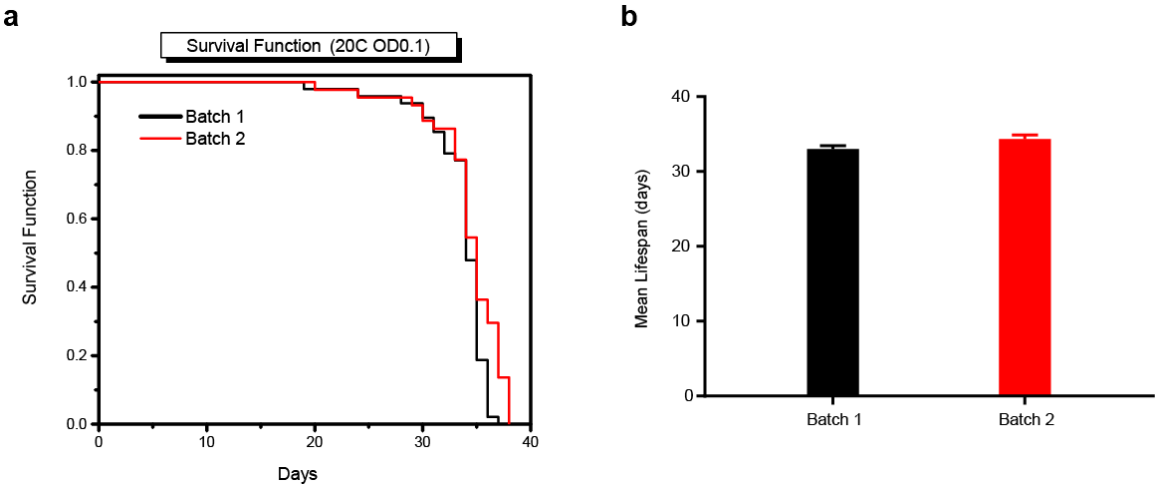

Figure 4. 8 Survival curves via Kaplan-Meier estimator at same culture condition (20 ℃ and OD0.1). a) Survival curves show the surviving fraction of animals at different ages. b) Mean lifespan (days) and standard error of mean (days) of different trials at the same culture condition. (Batch 1: 33.6 ± 0.46 days, Batch 2: 34.3 ± 0.53 days).

4.4 Quantitative measurements of age-related changes of physiological functions

As previously described, the aging process is characterized by progressive degenerative changes in tissue and function that increase the probability of mortality. A major element of aging research is to identify and measure the series of events that cause these changes and analyze environmental, genetic, and stochastic factors that affect them. Thus, the basis of these studies is to accurately identify and measure the aging phenotype.

In addition to the assessment of longevity, the system is capable of assessing more detailed behavior profiles due to the high temporal resolution of the platform. The Thorlabs camera (DCC1545M) has a sensor area of 6.66 mm by 5.32 mm divided into 1280 x 1024 pixels. In combination with the low magnifications ranges of the zoom lens (<0.8X, Edmund Optics #54-363), all of the chambers on a single microfluidic device can be captured within a single field of view at a resolution of roughly 17.5 μm per pixel[119]. This display resolution and frame rate of recorded videos (14 frames per second) are sufficient for quantitative analysis of behaviors (Figure 4.9). In order to elucidate the relationships between different age-dependent variables at any given age, I developed methods to measure age-related changes quantitatively and analyzed correlations among these changes over a worm's lifespan. I chose to measure three physiological processes that can be observed in liquid culture: body bending cycle, centroid velocity, and amplitude of the body wave[123-125]. This is because these parameters well describe the locomotion of worms in liquid[46,123,126].

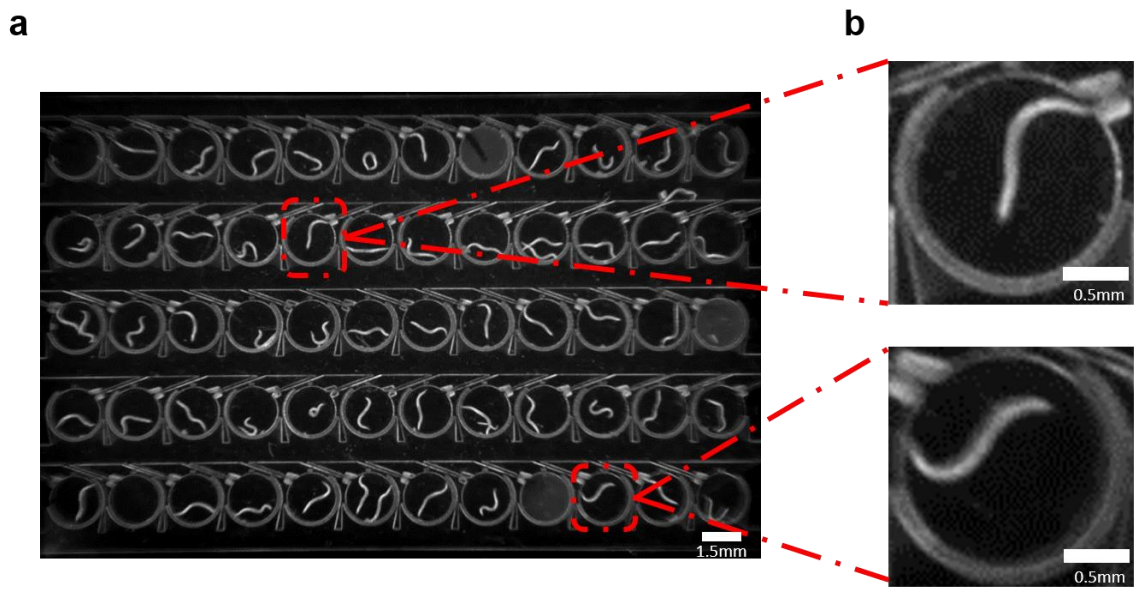

Figure 4. 9 a) Example image of device from the recorded video frame (OD0.1) and b) zoomed-in worms. The spatial resolution of captured images allows worms to be distinguished with greater clarity.

4.4.1 Machine-vision algorithm

To quantify movement during the aging process, I developed a machine-vision algorithm that segments the images and analyzes the posture of each worm in every frame of a video sequence for behaviour extraction (Figure 4. 10). The computer algorithm to define worm the skeleton from the video was implemented in MATLAB. First, the average value of each pixel across all frames was subtracted from every frame to remove the background, and it uses the Niblack algorithm to binarize the greyscale input image[127,128]. Then, user inputs by identifying the center of four chambers' corners in the device are interpolated to identify the centers of chambers, and the binary image of each individual chamber is processed. Noise regions with area smaller than a threshold value (70 pixels) are removed; then the image is thinned using MATLAB's built-in bwmorph 'thin'

functionality, and small branches are removed. The coordinates of the skeleton pixels are recorded in the order they appear on the worm, and the skeleton is smoothed. The smoothed coordinates are then used to find each point's distance along the worm and curvature, which is accomplished with the built-in four quadrant inverse tangent function[123]. The instantaneous shape of the worm can be fully described by defining the curvature of the worm at each point along the body (Figure 4.11). The amplitude of the body wave was calculated relative to the middle 80% of the worm body, to reduce the effects of head and tail thrashing[124]. Then, the distance the centroid traveled since the last frame is recorded, and the average distance calculated by each point is calculated and recorded[124,129].

Figure 4. 10 Result of skeletonizing algorithm. Raw image acquired from a video sequence containing the worm body and structure of microfluidic device (Left). By applying the Niblack binarization algorithm algorithm, thinning, and removing other structure and redundant pixels, the algorithm can generate worm skeletons.

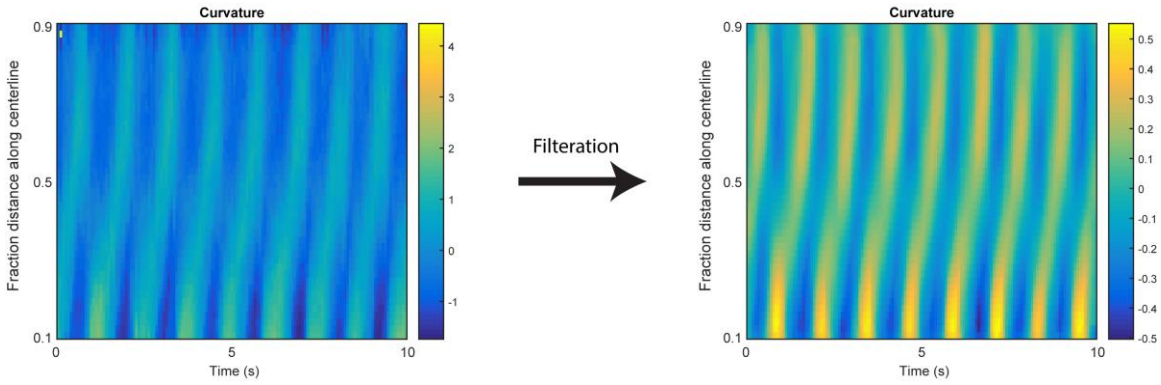

Figure 4. 11 Contour plot of the spatiotemporal dynamics of about nine cycles of the swimming behavior represented as the curvature measured at each point along the body centerline over 10 seconds. By using a filteration method, curvature is cleaned up. Values of curvature are scaled by color. I show the body coordinate as the fractional distance along the body centerline and display data corresponding to 0.1 - 0.9 to avoid showing the hyperflexible movements of the worm head and tail.

To demonstrate the effectiveness of behavior measurement algorithms, I compared the number of bending cycles calculated by hand-annotation and algorithm-derived annotations (Figure 4.12). Three 10 seconds videos were randomly chosen at different time points. I calculated the number of body bends of 53 individual worms for 10 seconds and also ran the algorithm to get those values. There was no significant different between data from hand-annotation and automated annotation, indicating the efficacy of the developed algorithm for annotating worm behaviors (Figure 4.12).

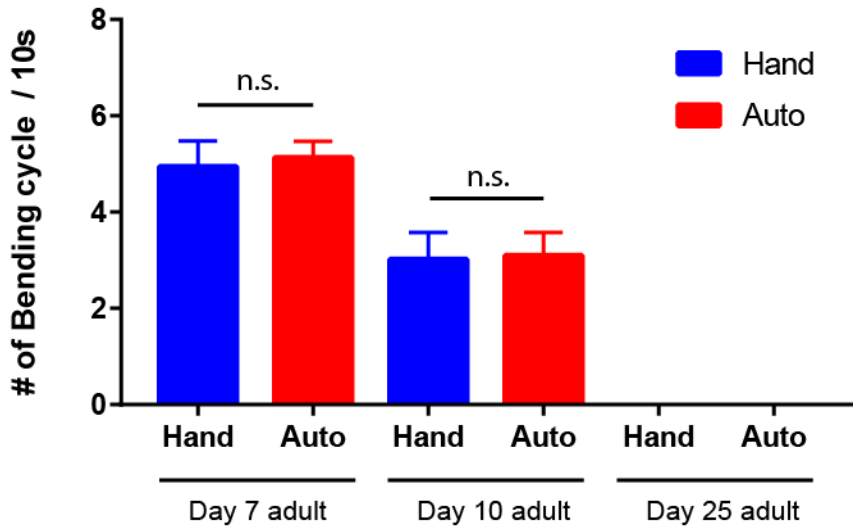

Figure 4. 12 A comparison of the bending cycle data from randomly chosen three videos obtained from hand annotations and software-derived annotations shows no significant different.

4.5 Longitudinal assessment of behavior-based health metrics

Relationships between the decline of body movement and several other age-related changes have been characterized. For example, the sinusoidal body movement characteristic of young adults becomes progressively slower and less coordinated, before ceasing altogether in old worms[130,131]. Huang *et al*. showed that the duration of fast body movement was positively correlated with lifespan in wild-type animals and several mutants[130,132]. To examine the relationships between age and locomotion, I used the algorithm to extract behavior information such as the frequency of body bends, centroid velocity, and amplitude over worms' lifetime. Fourty-eight 10-second videos were recorded on each day to monitor spontaneous behavior. I used the data sets from four experimental conditions (20 ℃ OD 0.1, 25 ℃ OD 0.1, 20 ℃ OD 0.1, and 20 ℃ OD 1) in this assessment.

4.5.1 Age-related behavior changes

I measured body bending frequency, centroid velocity, and body wave amplitude quantitatively using machine-vision algorithm (Section 4.4) for every day of adulthood over worms' lifetimes (Figure 4.13-14). These quantitatively extracted behavior profiles represent the age-related deterioration that occurs in adult worms over their lifetimes. Specifically, the body movement of young adult worms is relatively continuous and well-coordinated, following a sinusoidal pattern. As a worm ages, its body movement becomes progressively less continuous and coordinated and ultimately stops altogether[130,131]. Figure 4.13a shows the age-related decline in body bending frequency across two populations. For example, the bending frequency at 20 ℃ and OD0.1 culture condition declined gradually from day 3 until day 13 to 0.46 $\pm$ 0.03 Hz and rapidly over the next day (day 14 adult) to 0.17 $\pm$ 0.02 Hz. On the other hand, frequency at 25 ℃ and OD0.1 culture condition where worms died earlier than 20 ℃ and OD0.1 population, declined gradually from day 3 until day 8 to 0.65 $\pm$ 0.03 Hz and then rapidly from day 8 until day 11 to 0.19 $\pm$ 0.02 Hz (Figure 4.13a). As shown in Figure 4.5a, at an equivalent food level (OD0.1), the body bending frequency of worms at higher temperature (25 ℃) declined earlier than that of worms at lower temperature (20 ℃). Interestingly, the centroid velocity and amplitude of body wave are decreased gradually over the entire lifetime.

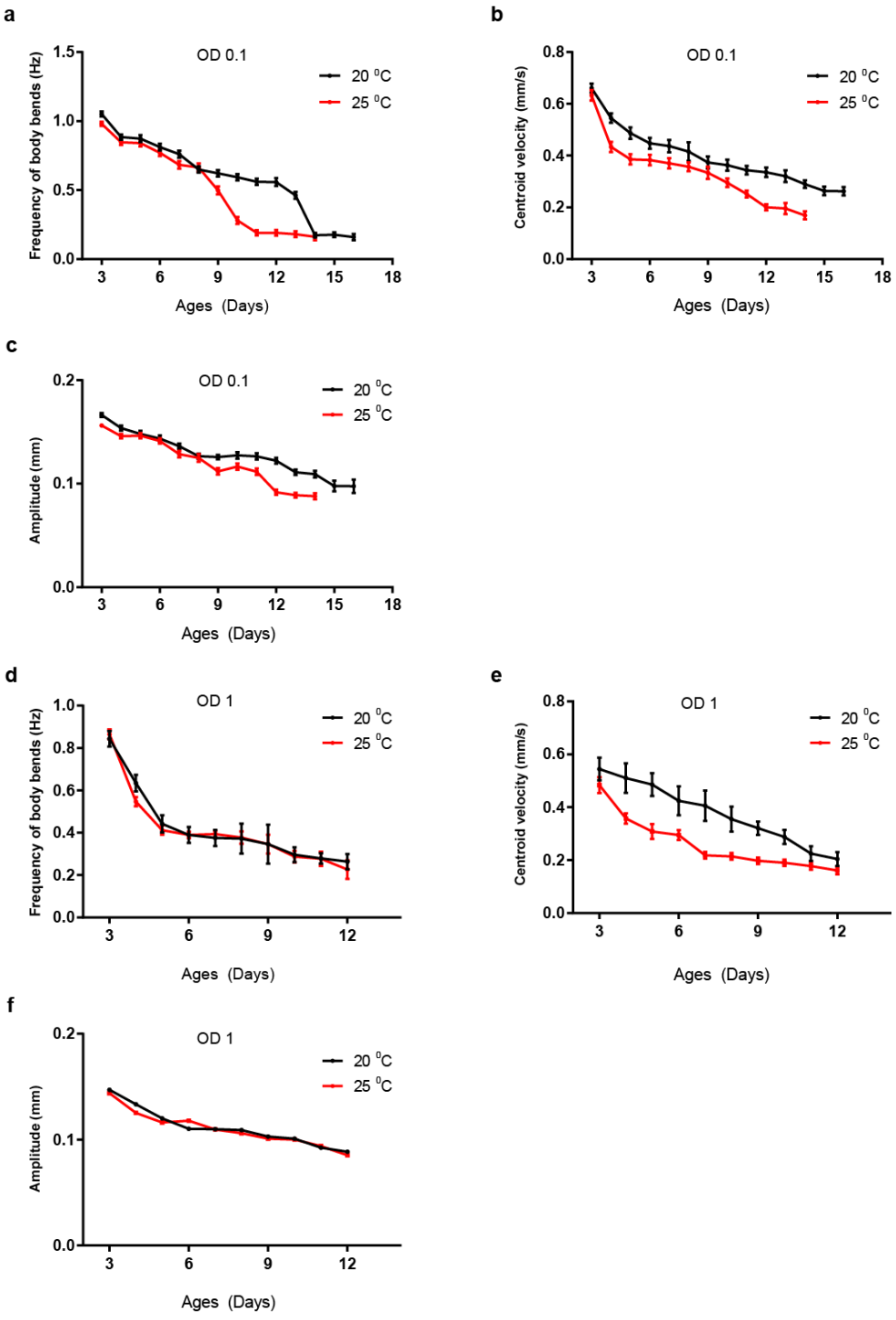

Figure 4. 13 Quantitatively measured behavior profiles at different culture conditions. a-c) OD0.1, 25 ℃ or 20 ℃ and d-f) OD1, 25 ℃ or 20 ℃.
a, d) Frequency of body bends (Hz) b, e) centroid velocity (mm/s) c, f) amplitude of body wave (mm) over worms' lifetime at two different temperature conditions (red: 25 ℃ / black: 20 ℃). Error bars represent S.E.M.

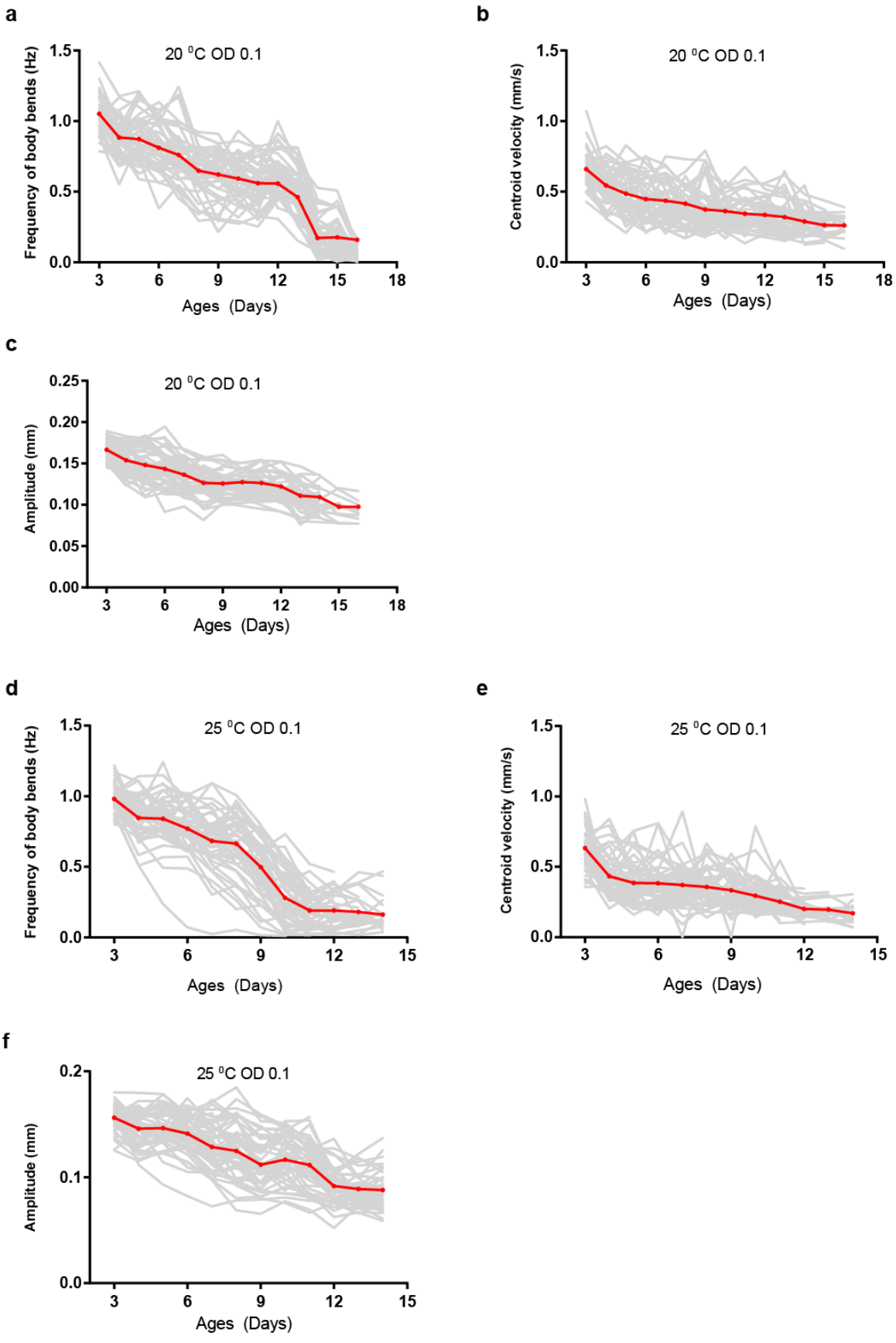
a
20 °C OD 0.1
Frequency of body bends (Hz)
1.5
1.0
0.5
0.0
3
6
9
12
15
18
Ages (Days)
b
20 °C OD 0.1
Centroid velocity (mm/s)
1.5
1.0
0.5
0.0
3
6
9
12
15
18
Ages (Days)
c
20 °C OD 0.1
Amplitude (mm)
0.25
0.20
0.15
0.10
0.05
0.00
3
6
9
12
15
18
Ages (Days)
d
25 °C OD 0.1
Frequency of body bends (Hz)
1.5
1.0
0.5
0.0
3
6
9
12
15
Ages (Days)
e
25 °C OD 0.1
Centroid velocity (mm/s)
1.5
1.0
0.5
0.0
3
6
9
12
15
Ages (Days)
f
25 °C OD 0.1
Amplitude (mm)
0.2
0.1
0.0
3
6
9
12
15
Ages (Days)

Figure 4. 14 Quantitatively measured behavior profiles of individual worms (gray) and average (red) at a-c)20 ℃ OD 0.1 and d-f)25 ℃ OD 0.1 condition. a) Frequency of body bends (Hz) b) centroid velocity (mm/s) c) amplitude of body wave (mm) over worms' lifetime.

Moreover, cross-sectional study that includes an evaluation of each individual can identify correlations among age-related changes that are measured at the same time in the lifespan. Thus, I evaluated how two behavior variables correlated on the individual worm level and then how these correlations change over the worms' lifetime four time points (Figure 4.15). I measured the correlation among age-related changes using a Spearman rank correlation[133]. Its correlation coefficient, ρ, ranges from -1 to +1: ρ values of +1, 0 and -1 indicate total positive, no, and total negative correlation, respectively. Interestingly, the body bending frequency and the body wave amplitude show higher correlation than other pairs (Table 4.1). Generally, these correlation is decreased in old worms (Table 4.1).

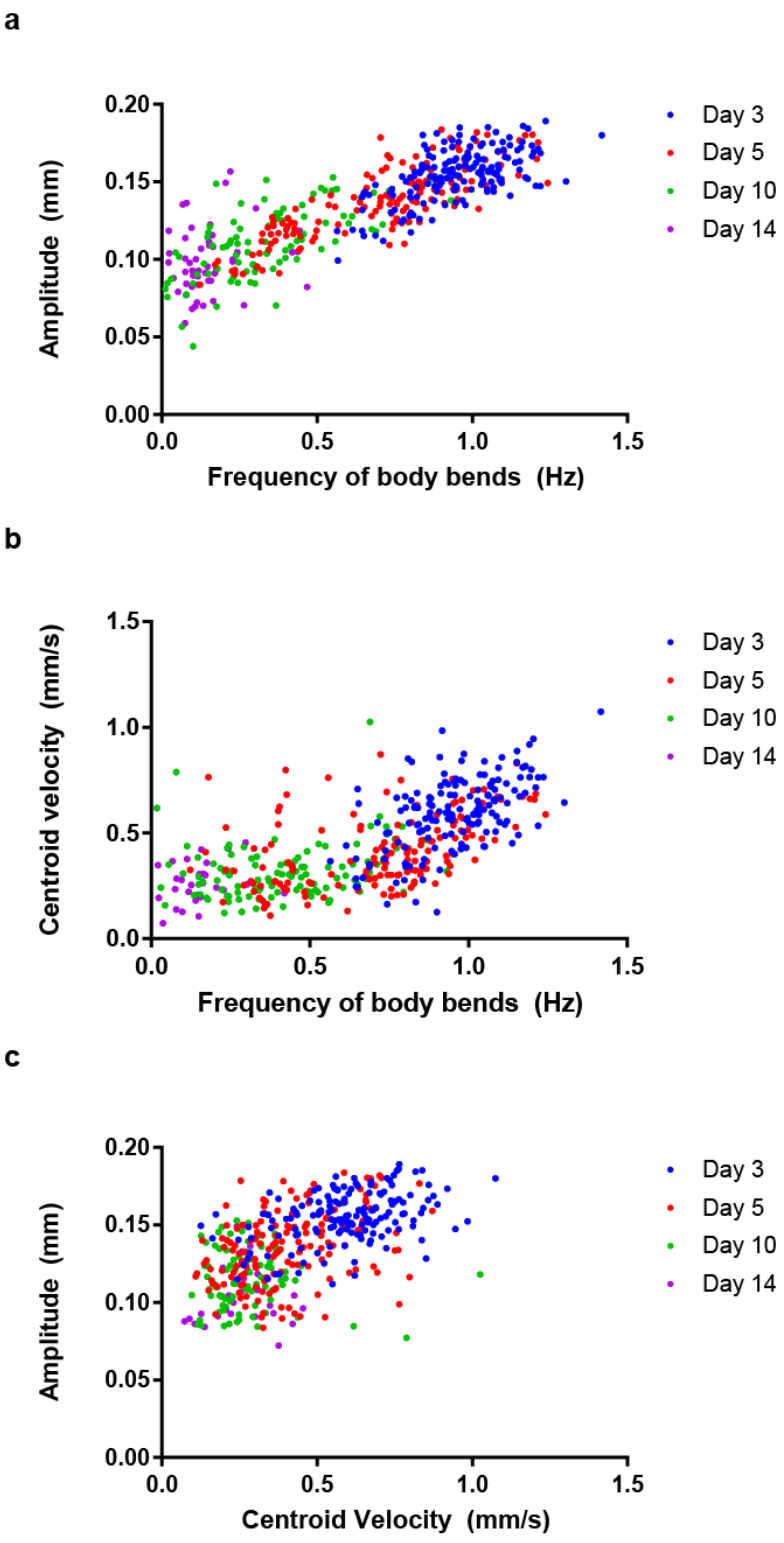

Figure 4. 15 The correlation between a) frequency of body bends and amplitude, b) frequency of body bends and centroid velocity, and c) centroid velocity and amplitude at four different time points. Each point represents one worm (n=162).

Days	Parameters	Body bends vs Amplitude	Body bends vs Velocity	Velocity vs Amplitude
Day 3	Spearman, ρ	0.5463	0.5175	0.3732
	P value	<0.0001	<0.0001	<0.0001
Day 5	Spearman, ρ	0.814	0.4967	0.3875
	P value	<0.0001	<0.0001	<0.0001
Day 10	Spearman, ρ	0.651	0.2833	0.1241
	P value	<0.0001	0.0031	0.2521 (n.s.)
Day 14	Spearman, ρ	0.1698	0.3049	0.2754
	P value	0.2336 (n.s.)	0.1077 (n.s.)	0.1337 (n.s.)

Table 4. 1 Results of Spearman rank correlation analysis.

4.5.2 The age-related changes of evoked behaviors

C. elegans can sense its environment using a variety of modalities, including chemical and mechanical stimulation, and temperature. Several studies have demonstrated age-related loss of some of these sensory abilities such as chemotaxis towards an attractive odorant or isothermal tracking[134,135]. Interestingly, it was connected to the decline in spontaneous movement, indicating that the primary cause may be motor deficits[132,134]. For

the study of sensory perception changes over a worm's lifetime, the platform is designed to deliver mechanical pulse stimuli via off-chip flow control and acquire periodic videos to assess age-related declines in stimulated and spontaneous behaviors. Every hour a pressure-induced mechanical pulse stimulus is delivered. Two minutes after this stimulation, a 10 second video is captured to assess the behavioral response. 45 minutes after the stimulus, another 10 second video is acquired to monitor spontaneous behavior.

With these data sets, I tested the age-dependent changes of evoked behaviors by measuring behavioral information before and after pulse stimulations and then subtracting those values (Figure 4.16 and Figure 4.17). For example, in 20 ℃ OD 0.1, and OD 1 (with 20 ℃ and 25 ℃) culture condition, worms show more active movement after pulse stimulation than before stimulation (Figure 4.16a-c and Figure 4.17). Surprisingly, in 25 ℃ OD 0.1 culture condition, worms show the opposite trend of behavior compared to other culture conditions' data (Figure 4.16d-f). Generally, when they are young, pulse stimulation can evoke worms' fast movements such as body bending frequency and centroid velocity, but this response does not occur in old worms (Subtraction values change to negative one). (Figure 4.16 and Figure 4.17). On the other hand, the amplitude of body wave does not show clear difference between before and after the pulse stimulation. It might be related that the amplitude of the body wave is caused by contraction and relaxation of body muscles, not neuromuscular function. In addition, worms shown slightly slower locomotion in high OD culture condition (OD 1) than OD 0.1 due to the increased viscosity of high OD[123,136].

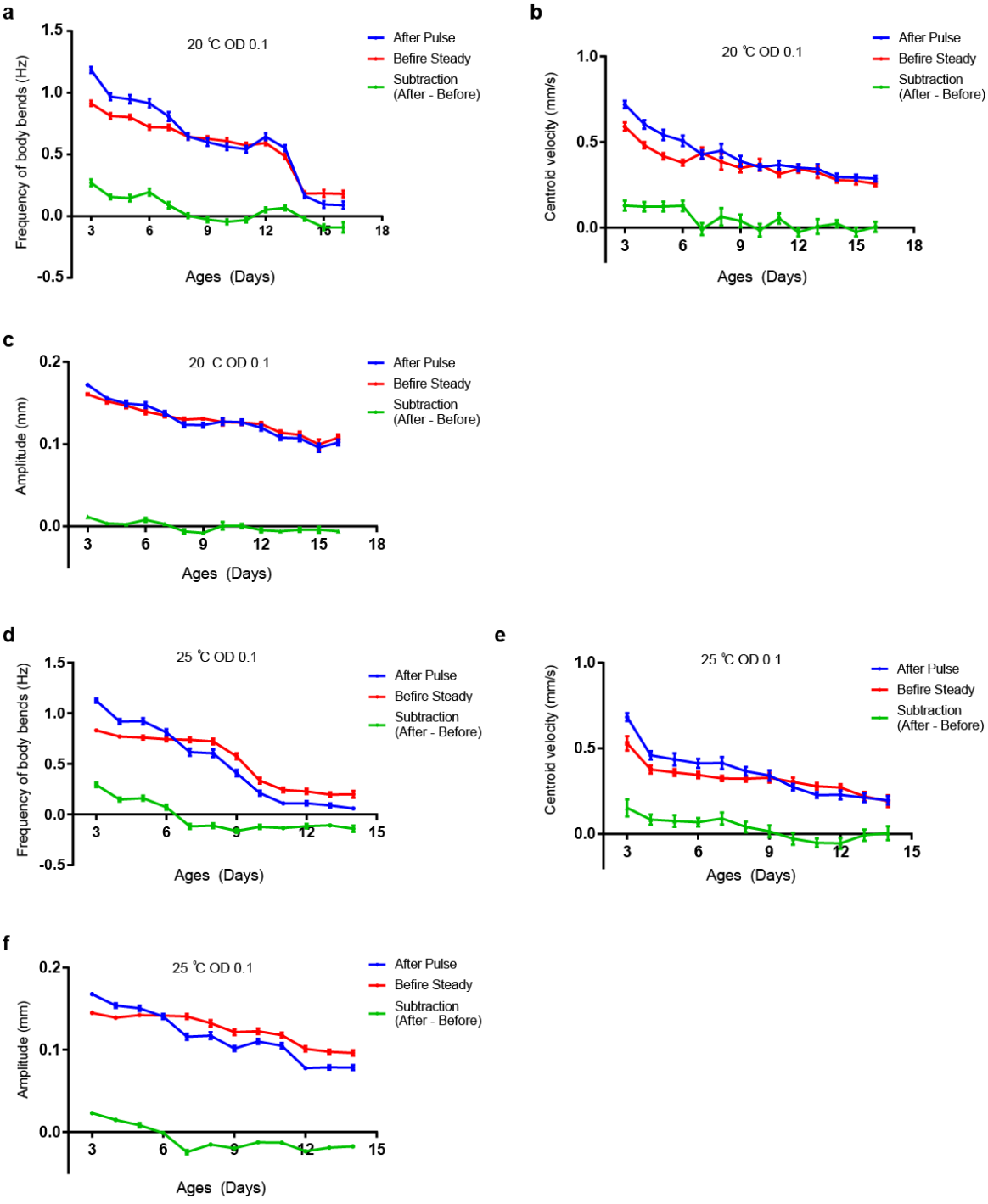

Figure 4. 16 Quantitatively measured behavior profiles before/after delivered pulse stimuli and subtracted values (After pulse – before pulse) at two different culture conditions: a-c) 20 ℃, OD 0.1 and d-f) 25 ℃, OD 0.1.
a, d) Frequency of body bends (Hz) b, e) centroid velocity (mm/s) c, f) amplitude of body wave (mm) over worms' lifetime. Error bars represent S.E.M.

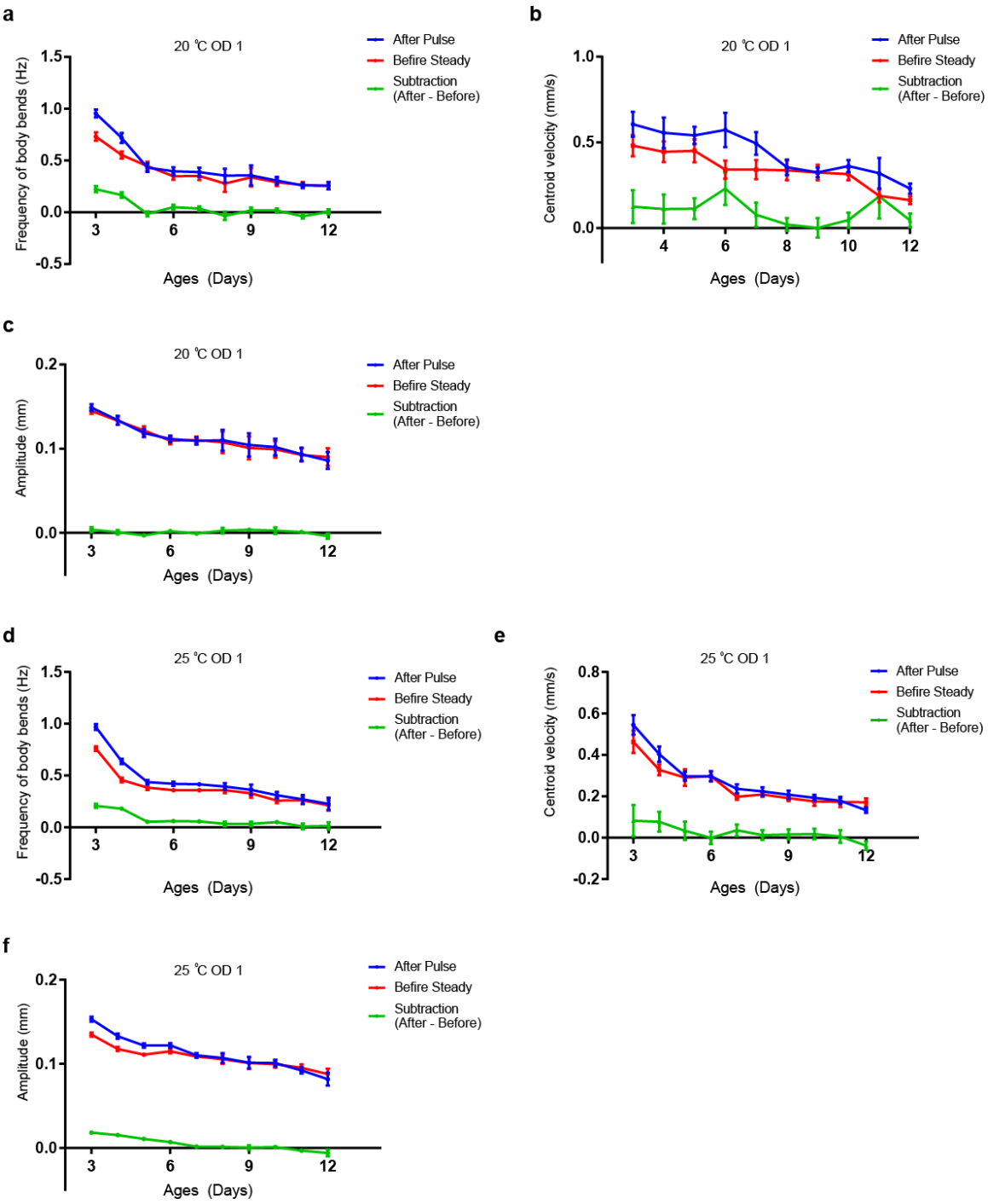

Figure 4. 17 Quantitatively measured behavior profiles before/after delivered pulse stimuli and subtracted values (After pulse – before pulse) at two different culture conditions: a-c) 20 ℃, OD 1 and d-f) 25 ℃, OD 1.
a, d) Frequency of body bends (Hz) b, e) centroid velocity (mm/s) c, f) amplitude of body wave (mm) over worms' lifetime. Error bars represent S.E.M.

4.6 Correlations between the declines of age-related behaviors and lifespan

In order to evaluate a connection between age-related behavior changes and ultimate lifespan, I analyzed quantitative behavior and lifespan data sets by plotting elements of behavior against lifespan for each individual. For this assay, I defined several stages of behaviors: fast bending frequencies were >0.5 Hz, fast centroid velocities were > 0.3mm/s, and high amplitudes of body waves were >0.1 mm. These values are chosen to approximate 50 % of maximum average value.

I also measured the correlation between age-related changes and lifespan using a Spearman rank correlation (Figure 4.18). Worm's lifespan displayed a positive correlation with the durations of three quantitative behavioral stages; high body bending frequency ($r=0.9145$, $p<0.0001$), high centroid velocity ($r=0.9396$, $p<0.0001$), and high amplitude of body wave duration ($r=0.84$, $p<0.0001$). Not surprisingly, since both body bending frequency and centroid velocity parameters represent motor capacity of worms, these values show very similar correlations with lifespans. The positive correlations between lifespan and these behavior changes indicate that these measurements can be used to predict lifespan in liquid culture.

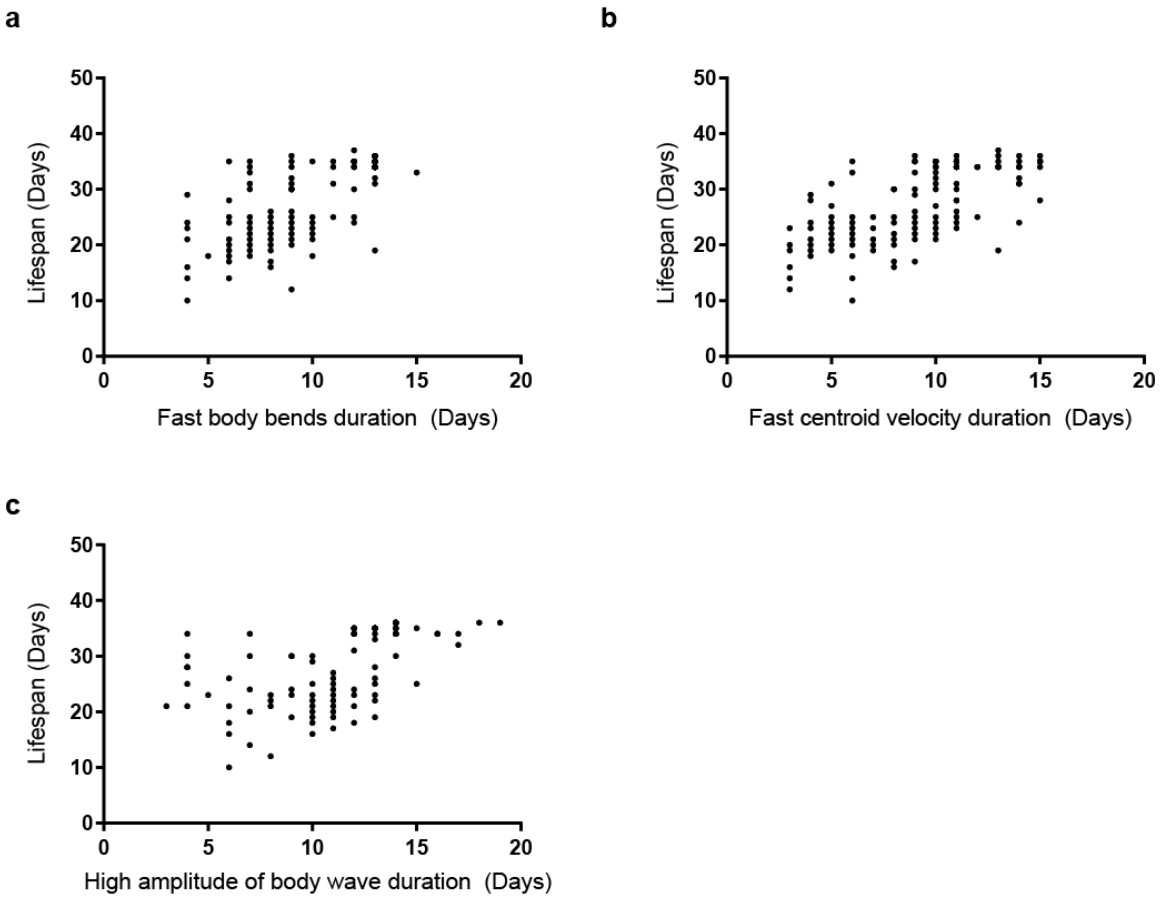

Figure 4. 18 Longitudinal analysis of duration of behavioral stages and lifespan. Each point represents one worm (or more than one worms in cases where multiple animals had identical values, n=162). The lifespan and duration of the stages of a) frequent body bends, b) fast-moving centroids, and c) large body wave amplitude are shown.

4.7 Conclusion

The developed system is capable of accommodating the fine, continuous control of both food and temperature conditions in a scalable manner, such that many different conditions can be assayed in parallel. Additionally, the ability to effectively time-share one acquisition sensor amongst these parallel assays permits the use of a single high-quality sensor to acquire detailed behavioral outputs at high frame rates and spatial resolution. Therefore, this platform enables high-throughput, high-content, long-term analysis of individual health outcomes with fine control of environmental variables. The quantity of data generated from this platform allows for high-quality investigation and statistical analysis of the aging process.

In order to identify and measure the series of events that cause degenerative changes during the aging process, I developed a machine-vision algorithm that can extract several quantitative behavioral information sets. With these extracted behavior data, I conducted longitudinal studies that involved serial measurements of behavior traits in each individual to investigate the relationships among age-related changes and between age-related changes and lifespan. The correlation between two behavior variables on an individual worm is lowered as it ages. Moreover, the animals which were cultured with dietary restriction or at low temperature experienced an increased number of healthy days based on quantitative descriptions of behavior. This analysis revealed that depending on the culture conditions, each behavior parameter declines with age at a different rate. Second, I demonstrated age-related loss of sensory perception. By measuring the age-dependent changes of evoked behaviors before and after stimulations, I observed when animals are young, pulse stimulation can evoke worms' fast movement, but this movement does not

occur in old worms. Lastly, three behavioral information that can describe the locomotion of worm in liquid such as frequency of body bends, centroid velocity, and amplitude of body bends shows high correlation with lifespan which can be used as lifespan predictors. Therefore, my analysis allows us to know the length of time that an individual can expect to live, and how healthy that individual can expect to be as it ages.

CHAPTER 5. CONCLUSIONS AND FUTURE DIRECTIONS

5.1 Thesis contributions

The objective of this thesis is to develop automated high-throughput microsystems for functional neuroimaging, with controlled external stimuli including mechanical, chemical, or both simultaneously, and to study sensory integration in the nervous system of *C. elegans*; secondarily, my thesis aimed to develop an automated microsystem for longitudinal culture and imaging of individual animals with highly controlled environmental conditions to study the process of aging, healthspan, and lifespan in *C. elegans*. The microsystems I engineered take advantage of microfluidic technology to precisely handle animals, deliver controlled stimulations, and control environmental conditionss as well as use computer-aided automation for high-throughput processing.

In the first aim, I developed a microfluidic platform for high-throughput controlled mechanical stimulation and functional neuroimaging in adult stages of *C. elegans*. Compared to conventional systems, the newly developed platform delivers quantitative stimuli and is fully automated, minimizing the variability introduced by human handling, thereby improving experimental throughput by using sets of pneumatically actuated PDMS membrane structures. These platforms can fully recapitulate the known neuronal dynamics in both gentle and harsh touch neurons, upon various types of stimulations while being faster and more standardized. To demonstrate a high-throughput screen application, I performed a pilot-scale screens of ligand molecules that may perturb calcium dynamics,

which is at present nearly impossible manually. Furthermore, by integrating with other microfluidic components to provoke additional sensory responses such as chemosensation, I developed another platform which can deliver the combinations of mechanical and chemical stimuli to worms in a high-throughput manner. By using this device, I observed cross-modal sensitization in interneuron activities for the first time in *C. elegans*, which one could imagine to be extended to other studies of sensory integration.

In chapter 3, I extended the mechanosensing device to monitor neural responses to mechanical stimuli in developing *C. elegans* larvae. The largest challenge was to develop easily deformable actuated membrane structures, which have low aspect ratio in order to deliver mechanical stimuli to smaller worms. For example, the width and height of deformable membrane are 50 μm and 10 μm, respectively, in order to touch specific regions of L2 stage of worms. However, the limitation of membrane thickness is 25 μm due to bonding issues. Thus, the thickness of membrane is big compared to height of it, which prevents stimuli from being delivered as consistently. With a new device fabrication method, a series of devices can deliver robust and precise mechanical stimuli in developmental stages of worms.

I applied this device to three applications. The first application is to observe the differences in neuronal responses to mechanical stimuli during sleep and awake states in developing *C. elegans*. In sleep-like states, neuronal activity to mechanical stimuli is highly reduced, while the neuronal responses are much clearer in awake worms. This demonstrates that my device can be used for the study of neuronal responses in C. elegans lethargus states, which is difficult to do using conventional methods. Second, like the previous device, the platforms also fully replicate known neuronal dynamics in both gentle

and harsh touch neurons, upon various types of stimulus. This demonstrates that my system for smaller larvae can also deliver quantitatively controlled stimuli, even though it is scaled down. Lastly, I used the device to test the effect of the rate of mechanical stimulation on gentle touch neurons and observed that higher and more robust neuronal response can be evoked at higher frequencies of stimulation. Therefore, the device allows us to explore whether the entire mechanical sensory system behaves similarly to a high-pass or band-pass filter.

In chapter 4, together with an alumna of the Lu lab (Dr. Mei Zhan), I developed a long-term individual animal tracking platform integrated with microfluidics and hardware and software technologies. This platform is easily scalable and operated automatically. With this platform, I monitored both individual longevity and behavior of *C. elegans* with sub-hourly experimental time resolution at a variety of temperature and food levels. I validated this platform for lifespan assays with diverse environmental conditions. This platform can sustain animals throughout their entire lifespan and replicate well-documented environmental longevity effects.

To assess behavior-based metrics of health and the relationship between age-related changes and lifespan, I developed automatic behavior analysis algorithms and statistical methods. With quantitative behavior data, I observed that the body movement of young adult worms is relatively continuous and active. However, as a worm ages, its movement becomes less frequent, and the correlations between behavior metrics are decreased. Moreover, I demonstrated the effect of age on sensory perceptions and the relationship between age-related behavior changes and lifespan. Therefore, the set of new platforms has the potential to address many important questions in aging including investigating the

environmental determinants of aging, the cause of individual variability, the course of age-related decline and the effects of interventional strategies to improve health outcomes.

As a whole, the platforms developed in my projects allow for the investigation of the functional activity and connectivity of the nervous system, as well as long-term behavior and physiology in a wide range of developmental and aging stages. These systems will facilitate a broad range of biological and medical research. Beyond work in our own lab, I envision these systems to be instrumental in future investigations in perceptual processing through animal brain and drug discovery for human diseases.

5.2 Future directions

The work presented in this thesis demonstrates the capability of our microsystems to perform high-throughput *in vivo* functional imaging and controlled external stimulation, while tracking longevity and long-term behavior in a highly controlled. In this section, I discuss possible applications of our technologies for future work.

5.2.1 Forward genetic screens to identify mutants related to sensory integration

One possible future work is using the device for mechanical stimulation to discover the genes responsible for mechanosensation. Forward genetics is a technique to discover mutations that result in phenotypes of interest by screening a population of mutagenized animals for particular traits. This method has been widely used for many decades, starting with simple visual assays. With the introduction of fluorescent markers, more subtle

differences in phenotypes, for example, morphologies of cells or genetic expression levels, can be screened for. This allows for the discovery of new roles of genes or signaling pathway. Thus far, very few screens have been done on neuronal dynamic information due to technical limitations (described in Section 2.1).

In Chapter 2, I demonstrated the utility of this system as a high-throughput screening platform using calcium imaging. I fully expect that this will allow us to discover novel genes that affect sensory integration in sensory or interneurons. For example, using calcium dynamics of one of the command interneurons, AVA or PVC (we already have strains which have calcium indicators on those neurons), we can study how sensory information is transmitted in a neural circuit to produce proper behavior. Ultimately, we can discover the details of signaling pathways for mechanotrasduction at a molecular level. Moreover, combined with studies on developing stages, we can understand changes in the functional roles of genes involved in mechanotransduction over a worm's lifespan.

5.2.2 Drug screens for the discovery of potential therapeutics

I demonstrated the feasibility of my platform for drug screens based on neuronal dynamics by performing pilot-scale screens of ligand molecules. With large scale screens, it is possible to identify small molecules from a putative compound library that may affect sensory and interneuronal responses to controlled chemical and mechanical stimuli. For instance, compounds that affect sensory neurons, particularly those that may enhance the activity of neurons, could be promising for potential therapies for human disorders such as deafness. Specifically, one on-going project is using humanized worms to screen

compounds to treat a human hearing disorder (conducted by Sol-Ah Lee in the Lu lab). Again, the discovered candidates from drug screens can be tested on developing worms to know the effect of drugs.

5.2.3 Whole brain calcium imaging with controlled stimulations

Thus far, most studies in neuroscience have been conducted on individual neurons or small groups of neurons, not on how entire brains respond to stimulation and modulate behavior. However, the advent of microscopy, particularly the spinning disk confocal microscope, has finally allowed for the imaging of whole worms with sufficient spatiotemporal resolution to examine neural activity in the whole brain at once. Specifically, a number of research groups have turned to the idea of "Whole Brain" (or "Pan-neuronal") imaging, where as many neurons as possible are imaged at once, either at rest or under deliberate stimulus (Table 5.1)[137-139]. This provides simultaneous information about a large number of neurons in parallel, for instance enabling the direct correlation of neuronal activity with stimulus.

Use of microfluidic devices from Chapters 2 and 3 to deliver controlled mechanical stimuli or combinations of mechanical and chemical stimuli permits the study of sensory integration in the whole brain. By looking through the data using a reverse correlation to find novel neurons responding to the stimulus, we may understand how information sensed by sensory neurons can be transmitted via interneurons, and go on to modulate animals behaviors. Another possibility is to compare whole brain activity after a single stimulus such as mechanical or chemical stimulation, or combinations of stimuli. In this way, we

may find new roles of neurons and understand the functional role of interneurons in the context of sensory integration.

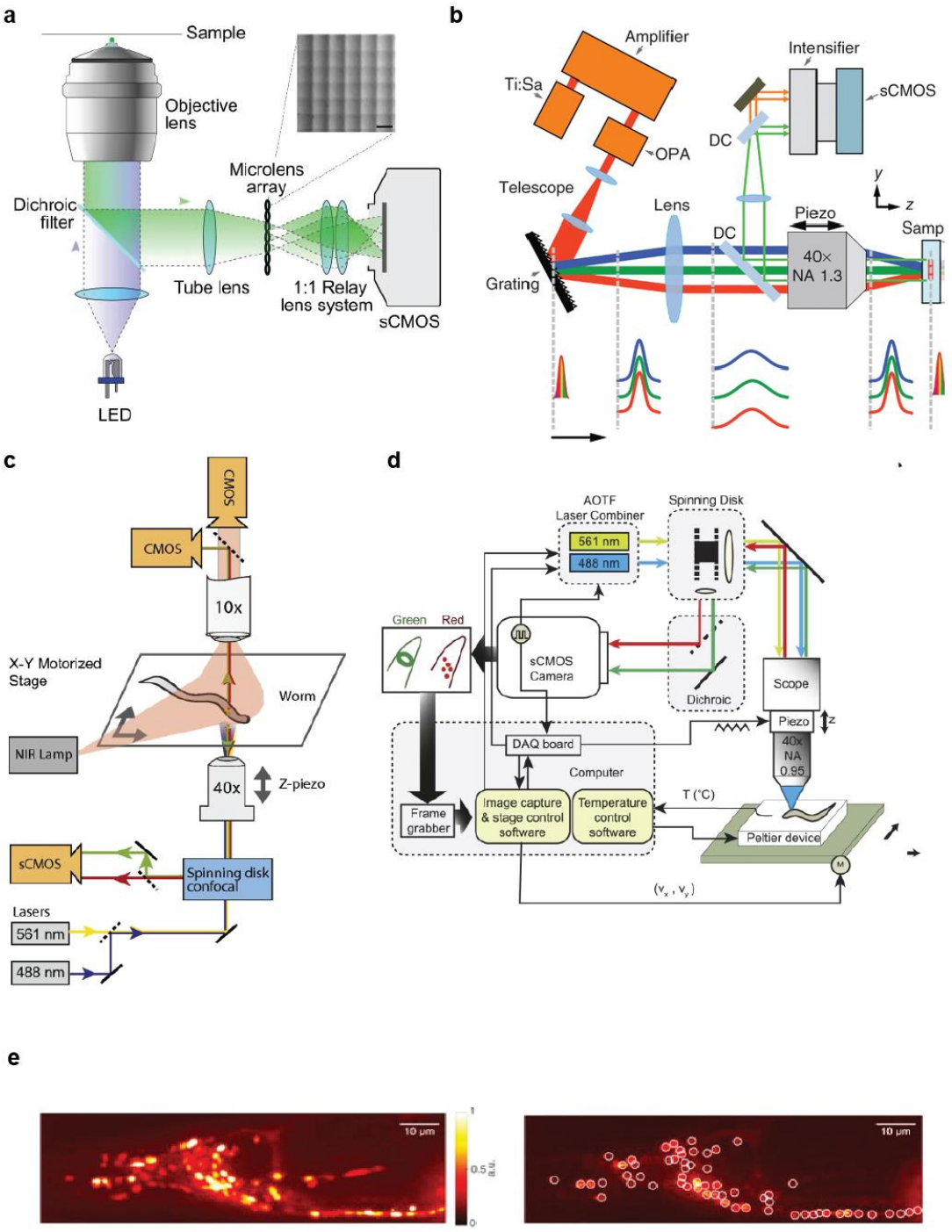

Figure 5. 1 Imaging Setups Used for Whole Brain Imaging. **a**) Light-field Deconvolution Microscopy.[138] **b**) Two-photon Light Sculpting Microscopy.[39] **c**) A Spinning Disk Confocal Microscopy-based setup for imaging of freely-roaming *C. elegans*[140] **d**) A Separate Spinning Disk Confocal Microscopy-based setup for imaging of freely-roaming *C. elegans*.[59] **e**) Representative frames from whole brain imaging videos. The top panel shows an example maximum intensity projection of one frame. The bottom shows a single *z* plane overlaid with segmented neuronal regions.[139]

First Author(s)	Freely-behaving whole brain?	Microscopy Setup	Worms Anesthetized?	# neurons observed	# worms reported
Boyden, Prevedel[138]	No	Light-field Microscopy	Partial	74	1
Zimmer, Schrödel[39]	No	Two-photon with sculpted light	Partial	~99	5
Kato[139]	No	Spinning-disc confocal	Partial	107-131	5
Nguyen [140]	Yes	Spinning-disc confocal	No	56-77	4
Venkatachalam[59]	Yes	Spinning-disc Confocal	No	26-84	5 (1 control)

Table 5. 1 Publications on whole brain imaging, illustrating the types of microscopy, the diversity in imaging conditions, and the number of neurons and worms imaged.

5.2.4 Further investigation of the relationships between environment, gene, and stochastic factors on life- and healthspan

The integrated microsystem from Chapter 4 enables the tracking of behavior-based health metrics and longitudinal assessment of health and longevity trajectories. It also brings up the essential mechanistic framework for addressing important questions: the study of stochastic factors may link molecular mechanisms to the aging process. By collecting mortality statistics from many genetic background populations, we will observe

how genetic, environment, and stochastic factors orchestrate the aging process, to a level of detail not currently feasible. Furthermore, by using reverse genetic screening or drug screening techniques, we will evaluate the manner and extent to which specific molecular processes contribute to the aspect of aging, health, and lifespan.

In addition, by adding a fluorescent imaging module on our platform, it is possible to measure diverse gene expression levels over a span of several lifetimes at different environmental and genetic conditions in a large population. This will enable the identification of correlations (or lack thereof) between gene expression levels, age-related behavioral changes, and lifespan. Ultimately, this may lead to potential factors that can affect life- and healthspan of animals.

APPENDIX A. RAW DATA FOR SURVIVAL ANALYSIS FROM CHAPTER 4

1: event happens / 0: censored observation

Chamber	Days	Events	Group		Chamber	Days	Events	Group
Estimated mean		**21.12727 ± 0.44499**			**Estimated mean**		**17.49091 ± 0.51566**	
1	15	1	20C, OD5		1	12	1	25C, OD5
2	23	1	20C, OD5		2	13	1	25C, OD5
3	23	1	20C, OD5		3			25C, OD5
4	22	1	20C, OD5		4	21	1	25C, OD5
5			20C, OD5		5	12	1	25C, OD5
6	20	1	20C, OD5		6	15	1	25C, OD5
7	20	1	20C, OD5		7	21	1	25C, OD5
7	23	1	20C, OD5		8	7	1	25C, OD5
8	23	1	20C, OD5		9	9	1	25C, OD5
9	23	1	20C, OD5		9	20	1	25C, OD5
10	20	1	20C, OD5		10	17	1	25C, OD5
11	23	1	20C, OD5		11	17	1	25C, OD5
12	23	1	20C, OD5		12			25C, OD5
13			20C, OD5		13			25C, OD5
14	24	1	20C, OD5		14	19	1	25C, OD5
15	23	1	20C, OD5		15	13	1	25C, OD5
16	23	1	20C, OD5		16	15	1	25C, OD5
17	24	1	20C, OD5		17	21	1	25C, OD5
18	21	1	20C, OD5		18			25C, OD5
19	24	1	20C, OD5		19	19	1	25C, OD5
20	20	1	20C, OD5		20	19	1	25C, OD5
21	19	1	20C, OD5		21	21	1	25C, OD5
21	23	1	20C, OD5		22	13	1	25C, OD5
21	23	1	20C, OD5		22	18	1	25C, OD5
22	21	1	20C, OD5		23	16	1	25C, OD5
22	23	1	20C, OD5		23	17	1	25C, OD5
23	23	1	20C, OD5		24	14	1	25C, OD5
23	23	1	20C, OD5		25	14	1	25C, OD5
23	23	1	20C, OD5		26	20	1	25C, OD5

24	16	1	20C, OD5		27	20	1	25C, OD5
26	23	1	20C, OD5		28	22	1	25C, OD5
27	21	1	20C, OD5		29	19	1	25C, OD5
28	23	1	20C, OD5		30	22	1	25C, OD5
29	12	1	20C, OD5		31	24	1	25C, OD5
30	23	1	20C, OD5		32	20	1	25C, OD5
31	23	1	20C, OD5		33	20	1	25C, OD5
32	23	1	20C, OD5		34	20	1	25C, OD5
33	23	1	20C, OD5		35	20	1	25C, OD5
35	17	0	20C, OD5		36			25C, OD5
36	23	1	20C, OD5		37	18	1	25C, OD5
37			20C, OD5		38			25C, OD5
38	23	1	20C, OD5		39	21	1	25C, OD5
39			20C, OD5		40	16	1	25C, OD5
40	22	1	20C, OD5		41	6	1	25C, OD5
41	23	1	20C, OD5		42	20	1	25C, OD5
42	22	1	20C, OD5		43	20	1	25C, OD5
43			20C, OD5		44	21	1	25C, OD5
44	20	1	20C, OD5		45	20	1	25C, OD5
45	16	1	20C, OD5		46	19	1	25C, OD5
46	23	1	20C, OD5		47	18	1	25C, OD5
47	22	1	20C, OD5		48	21	1	25C, OD5
48			20C, OD5		49	19	1	25C, OD5
49	15	1	20C, OD5		50	15	1	25C, OD5
50	22	1	20C, OD5		51	15	1	25C, OD5
51	23	1	20C, OD5		52	20	1	25C, OD5
52	23	1	20C, OD5		53	18	1	25C, OD5
53	23	1	20C, OD5		54	12	1	25C, OD5
54			20C, OD5		54	16	1	25C, OD5
55			20C, OD5		55	19	1	25C, OD5
56			20C, OD5		56	17	1	25C, OD5
57	20	1	20C, OD5		57			25C, OD5
58	23	1	20C, OD5		58	21	1	25C, OD5
59			20C, OD5		59			25C, OD5
60			20C, OD5		60			25C, OD5

Chamber	Days	Events	Group		Chamber	Days	Events	Group
Estimated mean		**22.13725 ± 0.53955**			**Estimated mean**		**18.9375 ± 0.39321**	
1	23	1	20C OD2.5		1			25C OD2.5
2	22	1	20C OD2.5		2	19	1	25C OD2.5
3	21	1	20C OD2.5		3	17	1	25C OD2.5
4	23	1	20C OD2.5		4	21	1	25C OD2.5
5	19	1	20C OD2.5		5	21	1	25C OD2.5
5	23	1	20C OD2.5		6	20	1	25C OD2.5
6			20C OD2.5		7			25C OD2.5
7	19	1	20C OD2.5		8	18	1	25C OD2.5
8	14	1	20C OD2.5		9	20	1	25C OD2.5
8	23	1	20C OD2.5		10	20	1	25C OD2.5
9	24	1	20C OD2.5		11			25C OD2.5
10	21	1	20C OD2.5		12			25C OD2.5
11	22	1	20C OD2.5		13	21	1	25C OD2.5
12	22	1	20C OD2.5		14	13	1	25C OD2.5
13	22	1	20C OD2.5		15	22	1	25C OD2.5
14	22	1	20C OD2.5		16	14	1	25C OD2.5
15	24	1	20C OD2.5		17	20	1	25C OD2.5
16	8	1	20C OD2.5		18	25	1	25C OD2.5
17	16	1	20C OD2.5		19	16	1	25C OD2.5
18	28	1	20C OD2.5		20	15	1	25C OD2.5
19	22	1	20C OD2.5		21	20	1	25C OD2.5
20	25	1	20C OD2.5		22	17	1	25C OD2.5
21	21	1	20C OD2.5		23	16	1	25C OD2.5
22	17	1	20C OD2.5		23	17	1	25C OD2.5
22	17	1	20C OD2.5		23	17	1	25C OD2.5
22	24	1	20C OD2.5		24	20	1	25C OD2.5
23	23	1	20C OD2.5		25	19	1	25C OD2.5
23	23	1	20C OD2.5		26	16	1	25C OD2.5
23	26	1	20C OD2.5		27	15	1	25C OD2.5
24	24	1	20C OD2.5		28	20	1	25C OD2.5
25	23	1	20C OD2.5		29	20	1	25C OD2.5
26	24	1	20C OD2.5		30	20	1	25C OD2.5
27	26	1	20C OD2.5		31	17	1	25C OD2.5
28	25	1	20C OD2.5		32	19	1	25C OD2.5
29	23	1	20C OD2.5		33	20	1	25C OD2.5
30	23	1	20C OD2.5		34	19	1	25C OD2.5
31	24	1	20C OD2.5		35	20	1	25C OD2.5
32	24	1	20C OD2.5		36			25C OD2.5
33			20C OD2.5		37			25C OD2.5

34			20C OD2.5		38			25C OD2.5
35	25	1	20C OD2.5		39			25C OD2.5
36			20C OD2.5		40			25C OD2.5
37			20C OD2.5		41	14	1	25C OD2.5
38			20C OD2.5		42			25C OD2.5
39			20C OD2.5		43	19	1	25C OD2.5
40	24	1	20C OD2.5		44	22	1	25C OD2.5
41			20C OD2.5		45	27	1	25C OD2.5
42	15	1	20C OD2.5		46	21	1	25C OD2.5
43	24	1	20C OD2.5		47	18	1	25C OD2.5
44			20C OD2.5		48	16	1	25C OD2.5
45	24	1	20C OD2.5		49	18	1	25C OD2.5
46	24	1	20C OD2.5		49	21	1	25C OD2.5
47			20C OD2.5		50	18	1	25C OD2.5
48	24	1	20C OD2.5		51	20	1	25C OD2.5
49	23	1	20C OD2.5		52	21	1	25C OD2.5
50	10	1	20C OD2.5		53	17	1	25C OD2.5
51			20C OD2.5		54	21	1	25C OD2.5
52	23	1	20C OD2.5		55	22	1	25C OD2.5
53	25	1	20C OD2.5		56			25C OD2.5
54			20C OD2.5		57			25C OD2.5
55			20C OD2.5		58			25C OD2.5
56	24	1	20C OD2.5		59			25C OD2.5
57			20C OD2.5		60			25C OD2.5
58	23	1	20C OD2.5					
59			20C OD2.5					
60			20C OD2.5					

Chamber	Days	Events	Group		Chamber	Days	Events	Group
Estimated mean		**29.53659 ± 0.45277**			**Estimated mean**		**19.32203 ± 0.50563**	
1	26	1	20C OD1		1	18	1	25C OD1
2	30	1	20C OD1		2	23	1	25C OD1
3	27	1	20C OD1		3	18	1	25C OD1
3	30	1	20C OD1		3	21	1	25C OD1
4	28	1	20C OD1		4	18	1	25C OD1
5	29	1	20C OD1		5	23	1	25C OD1
5	30	1	20C OD1		6	7	1	25C OD1
6	28	1	20C OD1		6	20	1	25C OD1
6	30	1	20C OD1		7	18	1	25C OD1
7	25	1	20C OD1		7	24	1	25C OD1
7	25	1	20C OD1		8	21	1	25C OD1
7	27	1	20C OD1		9	21	1	25C OD1
8	29	1	20C OD1		10	19	1	25C OD1
9	27	1	20C OD1		11	23	1	25C OD1
10	34	1	20C OD1		12	14	1	25C OD1
11	29	1	20C OD1		13	20	1	25C OD1
12			20C OD1		14	12	1	25C OD1
13			20C OD1		15			25C OD1
14	22	1	20C OD1		16	23	1	25C OD1
14	33	1	20C OD1		17			25C OD1
15	28	1	20C OD1		18	20	1	25C OD1
16	30	1	20C OD1		19	24	1	25C OD1
17	33	1	20C OD1		20	14	1	25C OD1
18			20C OD1		20	14	1	25C OD1
19	27	1	20C OD1		20	14	1	25C OD1
19	30	1	20C OD1		21	20	1	25C OD1
20			20C OD1		22	9	1	25C OD1
21			20C OD1		22	17	1	25C OD1
22			20C OD1		23	17	1	25C OD1
23			20C OD1		23	17	1	25C OD1
24			20C OD1		24	21	1	25C OD1
25	25	1	20C OD1		25	10	1	25C OD1
26	30	1	20C OD1		26	23	1	25C OD1
27	31	1	20C OD1		27	20	1	25C OD1
28	28	1	20C OD1		28	14	1	25C OD1
29			20C OD1		29	21	1	25C OD1
30			20C OD1		30			25C OD1
31	34	1	20C OD1		31	22	1	25C OD1
32	31	1	20C OD1		32	22	1	25C OD1

33			20C OD1		33	22	1	25C OD1
34			20C OD1		34	20	1	25C OD1
35			20C OD1		35			25C OD1
36	30	1	20C OD1		36			25C OD1
37			20C OD1		37			25C OD1
38			20C OD1		38			25C OD1
39	35	0	20C OD1		39			25C OD1
40	35	0	20C OD1		40	21	1	25C OD1
41			20C OD1		41	25	1	25C OD1
42	21	0	20C OD1		42	19	1	25C OD1
43	20	0	20C OD1		43	23	1	25C OD1
44	33	1	20C OD1		44	25	1	25C OD1
44	33	1	20C OD1		45	16	1	25C OD1
45	30	1	20C OD1		46	21	1	25C OD1
46	33	1	20C OD1		47	21	1	25C OD1
47	17	0	20C OD1		48	19	1	25C OD1
48	29	1	20C OD1		49	31	0	25C OD1
48	32	1	20C OD1		50	22	1	25C OD1
49	25	1	20C OD1		50	23	1	25C OD1
50			20C OD1		51	23	1	25C OD1
51	33	1	20C OD1		52	20	1	25C OD1
52	32	1	20C OD1		53	16	1	25C OD1
53	31	1	20C OD1		54	21	1	25C OD1
54			20C OD1		55	23	1	25C OD1
55	32	1	20C OD1		56	20	1	25C OD1
55	33	1	20C OD1		57	20	1	25C OD1
56			20C OD1		58	20	1	25C OD1
57			20C OD1		59	19	1	25C OD1
58			20C OD1		60			25C OD1
59			20C OD1					
60			20C OD1					

Chamber	Days	Events	Group		Chamber	Days	Events	Group
Estimated mean		**33.60417 ± 0.45715**			**Estimated mean**		**22.70909 ± 0.33199**	
1			20C OD0.1		1	17	1	25C OD0.1
2			20C OD0.1		1	19	1	25C OD0.1
3			20C OD0.1		2	22	1	25C OD0.1
4	34	1	20C OD0.1		3	22	1	25C OD0.1
5	31	1	20C OD0.1		4	18	1	25C OD0.1
6	35	1	20C OD0.1		5	25	1	25C OD0.1
7	35	1	20C OD0.1		6	18	1	25C OD0.1
8	34	1	20C OD0.1		7	24	1	25C OD0.1
9	34	1	20C OD0.1		8	23	1	25C OD0.1
10	34	1	20C OD0.1		9	20	1	25C OD0.1
11	35	1	20C OD0.1		9	23	1	25C OD0.1
12	34	1	20C OD0.1		10	23	1	25C OD0.1
13	36	1	20C OD0.1		11	19	1	25C OD0.1
14	35	1	20C OD0.1		12			25C OD0.1
15	35	1	20C OD0.1		13			25C OD0.1
16	35	1	20C OD0.1		14			25C OD0.1
17	34	1	20C OD0.1		15	25	1	25C OD0.1
18	28	1	20C OD0.1		16	25	1	25C OD0.1
19	30	1	20C OD0.1		17			25C OD0.1
20	19	1	20C OD0.1		18	20	1	25C OD0.1
21	35	1	20C OD0.1		19	25	1	25C OD0.1
22	35	1	20C OD0.1		20	17	1	25C OD0.1
23	34	1	20C OD0.1		21	22	1	25C OD0.1
23	36	1	20C OD0.1		22			25C OD0.1
24	34	1	20C OD0.1		23			25C OD0.1
25	35	1	20C OD0.1		24			25C OD0.1
26	35	1	20C OD0.1		25	25	1	25C OD0.1
27	35	1	20C OD0.1		26	21	1	25C OD0.1
28	36	1	20C OD0.1		27	25	1	25C OD0.1
29	37	1	20C OD0.1		28	25	1	25C OD0.1
30	34	1	20C OD0.1		29	23	1	25C OD0.1
31	34	1	20C OD0.1		30	25	1	25C OD0.1
32	34	1	20C OD0.1		31	24	1	25C OD0.1
33	31	1	20C OD0.1		32	22	1	25C OD0.1
34	24	1	20C OD0.1		33	24	1	25C OD0.1
35			20C OD0.1		34	20	1	25C OD0.1
36	34	1	20C OD0.1		35	24	1	25C OD0.1
37			20C OD0.1		36	26	1	25C OD0.1
38	35	1	20C OD0.1		37	24	1	25C OD0.1

39	36	1	20C OD0.1		38	21	1	25C OD0.1
40	35	1	20C OD0.1		39	24	1	25C OD0.1
41			20C OD0.1		40	22	1	25C OD0.1
42	36	1	20C OD0.1		41	26	1	25C OD0.1
43	36	1	20C OD0.1		42	21	1	25C OD0.1
44	32	1	20C OD0.1		43	22	1	25C OD0.1
44	32	1			44	22	1	25C OD0.1
45	30	1	20C OD0.1		45	21	1	25C OD0.1
46			20C OD0.1		46	23	1	25C OD0.1
47			20C OD0.1		47	21	1	25C OD0.1
48	34	1	20C OD0.1		48	22	1	25C OD0.1
49			20C OD0.1		49	23	1	25C OD0.1
50	25	1	20C OD0.1		50	23	1	25C OD0.1
51			20C OD0.1		51	19	1	25C OD0.1
52	34	1	20C OD0.1		51	24	1	25C OD0.1
53	32	1	20C OD0.1		52	24	1	25C OD0.1
54			20C OD0.1		53	27	1	25C OD0.1
55			20C OD0.1		54	26	1	25C OD0.1
56	36	1	20C OD0.1		55	24	1	25C OD0.1
57			20C OD0.1		56	22	1	25C OD0.1
58	35	1	20C OD0.1		57	26	1	25C OD0.1
59	36	1	20C OD0.1		58	26	1	25C OD0.1
60	33	1	20C OD0.1		59	25	1	25C OD0.1
					60			25C OD0.1

Chamber	Days	Events	Group
Estimated mean		**34.30952 ± 0.55529**	
1	37	1	20C OD 0.1
2	34	1	20C OD 0.1
2	35	1	20C OD 0.1
3	33	1	20C OD 0.1
3	38	1	20C OD 0.1
4	37		20C OD 0.1
5	35	1	20C OD 0.1
6	37	1	20C OD 0.1
6	38	1	20C OD 0.1
7			20C OD 0.1
8	35	1	20C OD 0.1
9			20C OD 0.1
10	38	1	20C OD 0.1
11	35	1	20C OD 0.1
12	38	1	20C OD 0.1
13			20C OD 0.1
14			20C OD 0.1
15	30	1	20C OD 0.1
16	30	1	20C OD 0.1
17	31	1	20C OD 0.1
18	37	1	20C OD 0.1
19			20C OD 0.1
20	36	1	20C OD 0.1
20	36	1	20C OD 0.1
20	37	1	20C OD 0.1
21	34	1	20C OD 0.1
22			20C OD 0.1
23			20C OD 0.1
24			20C OD 0.1
25			20C OD 0.1
26	34	1	20C OD 0.1
26	34	1	20C OD 0.1
26	35	1	20C OD 0.1
27	24	1	20C OD 0.1
28	33	1	20C OD 0.1
29	35	1	20C OD 0.1
30	35	1	20C OD 0.1
31			20C OD 0.1
32	34	1	20C OD 0.1

33	33	1	20C OD 0.1
34	36	1	20C OD 0.1
35			20C OD 0.1
36			20C OD 0.1
37			20C OD 0.1
38			20C OD 0.1
39			20C OD 0.1
40			20C OD 0.1
41	34	1	20C OD 0.1
42	38	1	20C OD 0.1
43	35	1	20C OD 0.1
44			20C OD 0.1
45	38	1	20C OD 0.1
46			20C OD 0.1
47			20C OD 0.1
48	34	1	20C OD 0.1
49	37	1	20C OD 0.1
50			20C OD 0.1
51	29	1	20C OD 0.1
51	34	1	20C OD 0.1
51	34	1	20C OD 0.1
52			20C OD 0.1
53			20C OD 0.1
54	20	1	20C OD 0.1
55	37	1	20C OD 0.1
56	34	1	20C OD 0.1
57			20C OD 0.1
58			20C OD 0.1
59			20C OD 0.1
60			20C OD 0.1

APPENDIX B. DETAILED BEHAVIOR ANALYSIS DATA FROM CHAPTER 4

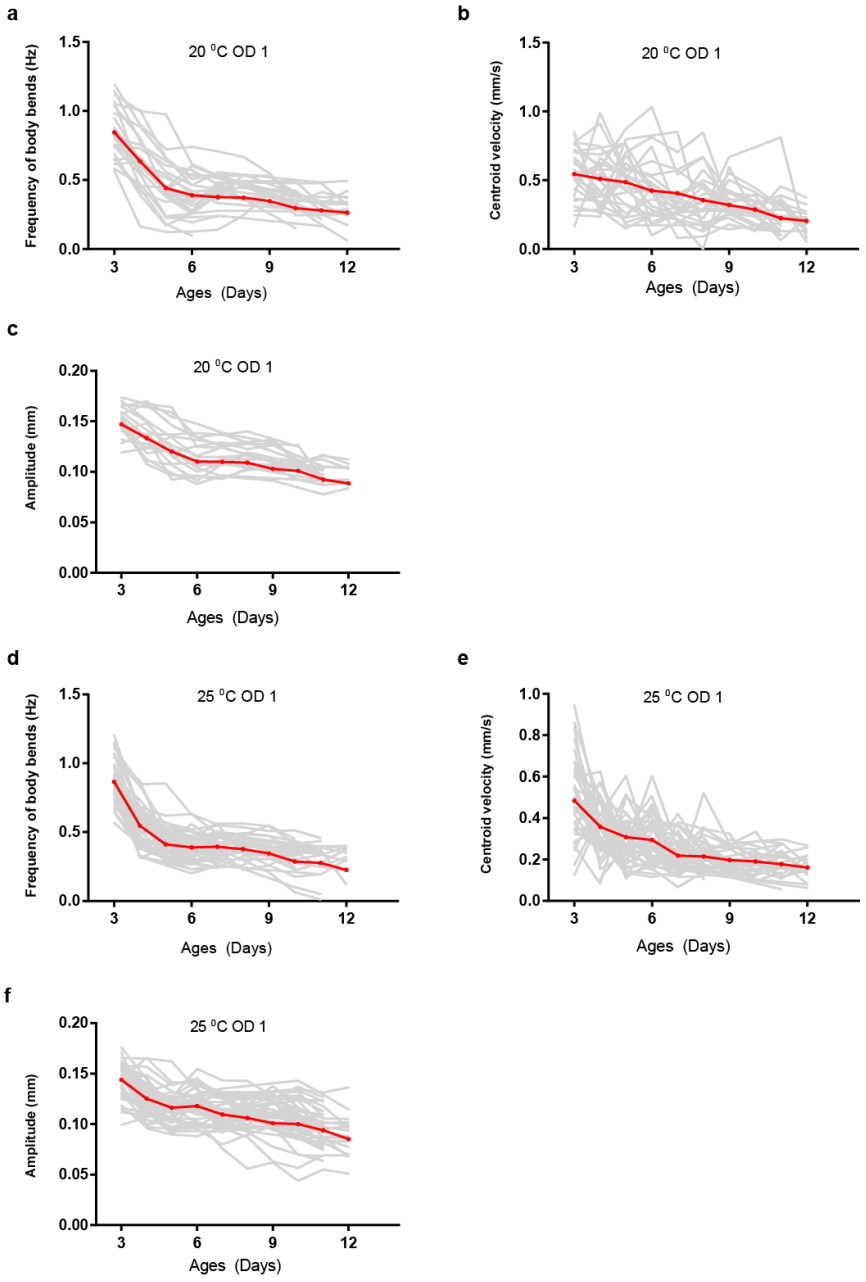

Appendix B. 1 Quantitatively measured behavior profiles of individual worms (gray) and average (red) at a-c)20 ℃ OD 1 and d-f)25 ℃ OD 1 condition. a) Frequency of body bends (Hz) b) centroid velocity (mm/s) c) amplitude of body wave (mm) over worms' lifetime.

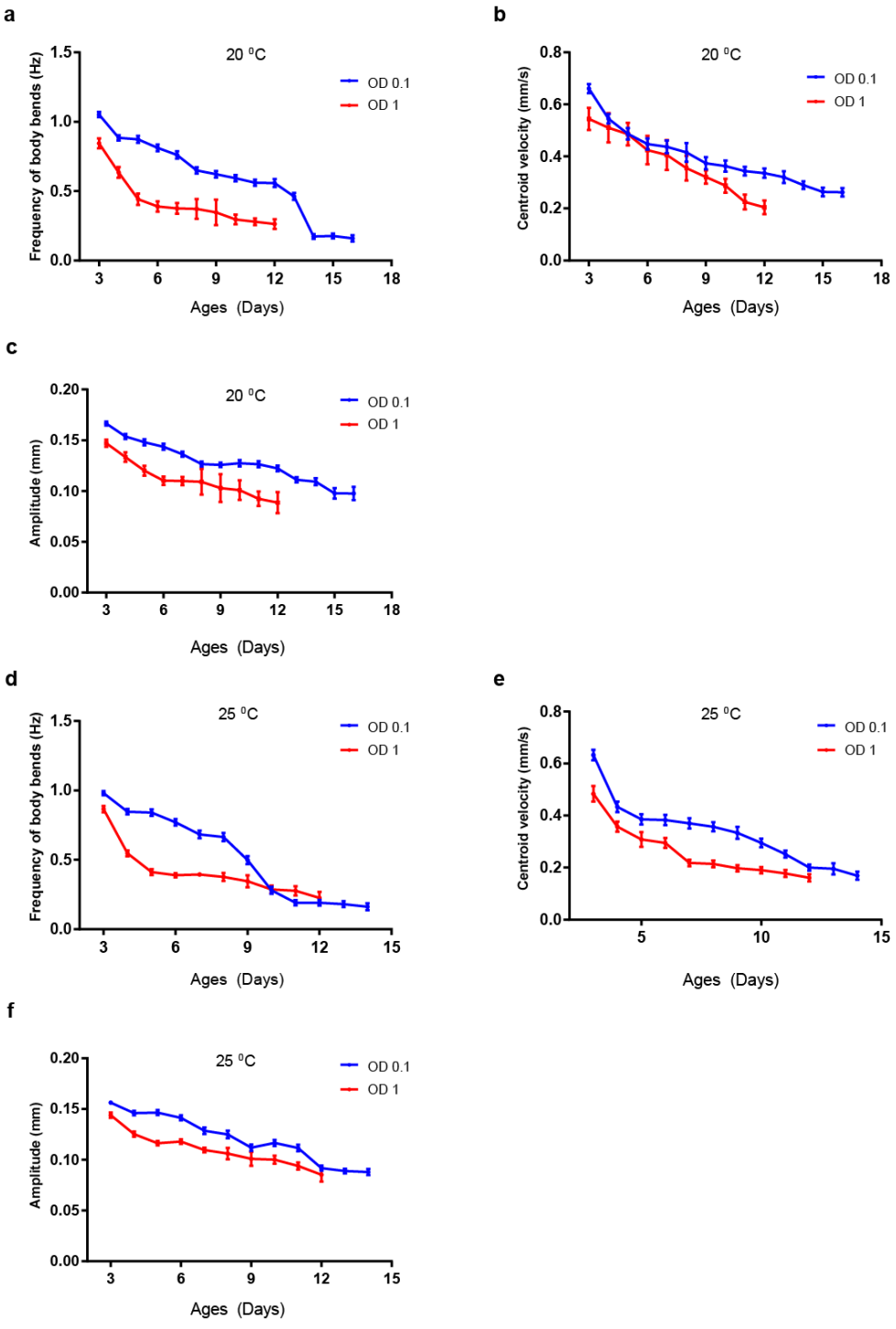

Appendix B. 2 Quantitatively measured behavior profiles at different culture conditions. a-c) 20 ℃, OD 0.1 and OD 1 and d-f) 25 ℃ OD 0.1 and OD 1.
a, d) Frequency of body bends (Hz) b, e) centroid velocity (mm/s) c, f) amplitude of body wave (mm) over worms' lifetime at two different temperature conditions (blue: OD 0.1 / red: OD1). Error bars represent S.E.M.

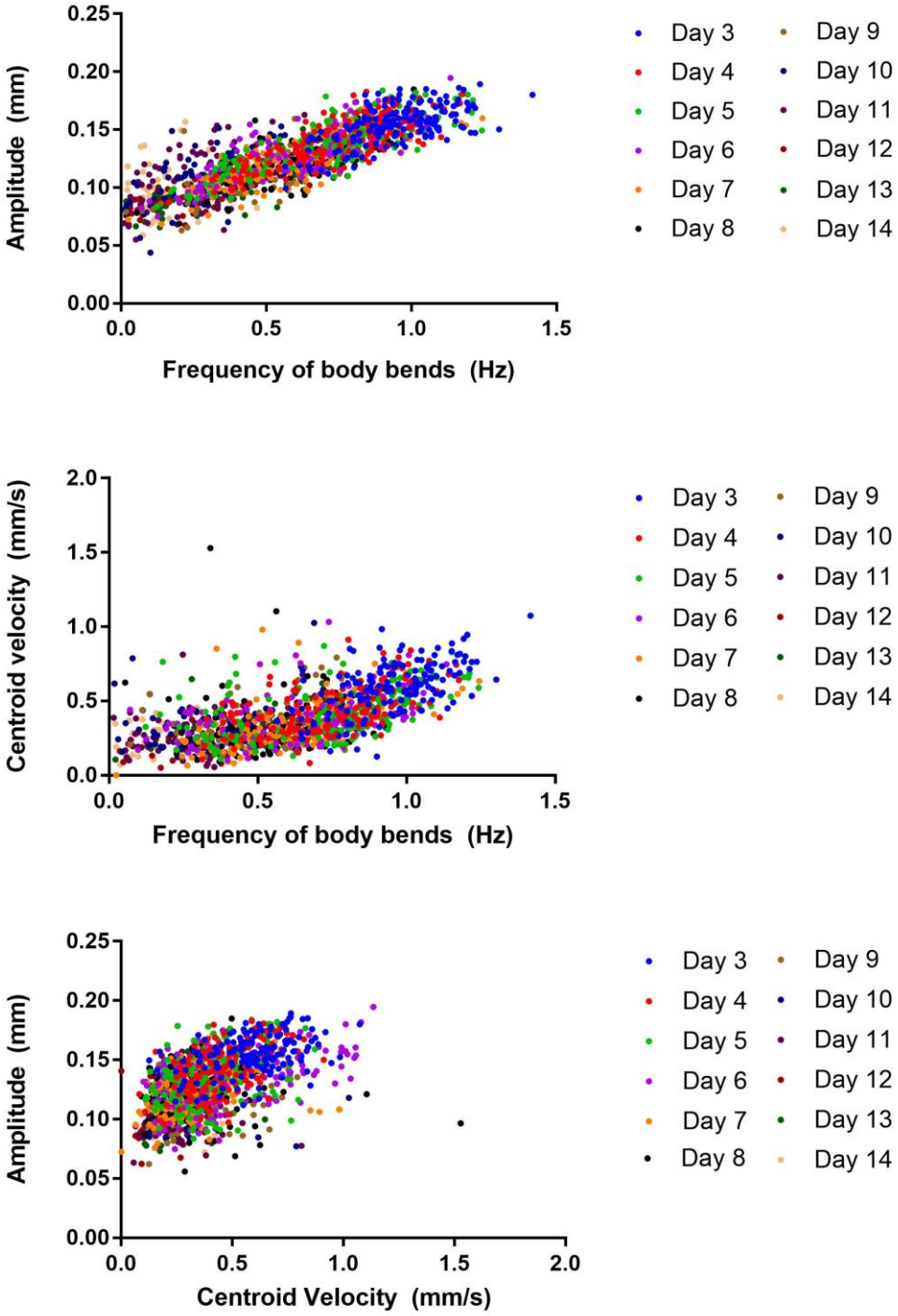

Appendix B. 3 The correlation between a) frequency of body bends and amplitude, b) frequency of body bends and centroid velocity, and c) centroid velocity and from day 3 to 14. Each point represents one worm.

REFERENCES

1 Corey, D. P. New TRP channels in hearing and mechanosensation. *Neuron* **39**, 585-588 (2003).

2 Kung, C. A possible unifying principle for mechanosensation. *Nature* **436**, 647-654 (2005).

3 Suzuki, H. *et al.* In vivo imaging of C. elegans mechanosensory neurons demonstrates a specific role for the MEC-4 channel in the process of gentle touch sensation. *Neuron* **39**, 1005-1017 (2003).

4 Goodman, M. B. *et al.* MEC-2 regulates C. elegans DEG/ENaC channels needed for mechanosensation. *Nature* **415**, 1039-1042 (2002).

5 O'Hagan, R., Chalfie, M. & Goodman, M. B. The MEC-4 DEG/ENaC channel of Caenorhabditis elegans touch receptor neurons transduces mechanical signals. *Nature neuroscience* **8**, 43-50 (2005).

6 Corey, D. P. & Garcia-Anoveros, J. Mechanosensation and the DEG/ENaC ion channels. *Science* **273**, 323 (1996).

7 Chatzigeorgiou, M. *et al.* Specific roles for DEG/ENaC and TRP channels in touch and thermosensation in C. elegans nociceptors. *Nature neuroscience* **13**, 861-868 (2010).

8 Hong, K. & Driscoll, M. A transmembrane domain of the putative channel subunit MEC-4 influences mechanotransduction and neurodegeneration in C. elegans. (1994).

9 Tavernarakis, N., Shreffler, W., Wang, S. & Driscoll, M. unc-8, a DEG/ENaC family member, encodes a subunit of a candidate mechanically gated channel that modulates C. elegans locomotion. *Neuron* **18**, 107-119 (1997).

10 Guarente, L. & Kenyon, C. Genetic pathways that regulate ageing in model organisms. *Nature* **408**, 255-262 (2000).

11 Lee, S.-J. & Kenyon, C. Regulation of the longevity response to temperature by thermosensory neurons in Caenorhabditis elegans. *Current biology* **19**, 715-722 (2009).

12 Kamath, R. S. *et al.* Systematic functional analysis of the Caenorhabditis elegans genome using RNAi. *Nature* **421**, 231-237 (2003).

13 Kindt, K. S. *et al.* Caenorhabditis elegans TRPA-1 functions in mechanosensation. *Nature neuroscience* **10**, 568-577 (2007).

14 Tobin, D. M. *et al.* Combinatorial expression of TRPV channel proteins defines their sensory functions and subcellular localization in C. elegans neurons. *Neuron* **35**, 307-318 (2002).

15 Tian, L. *et al.* Imaging neural activity in worms, flies and mice with improved GCaMP calcium indicators. *Nature methods* **6**, 875-881 (2009).

16 Chen, T.-W. *et al.* Ultrasensitive fluorescent proteins for imaging neuronal activity. *Nature* **499**, 295-300, doi:10.1038/nature12354 (2013).

17 White, J. G., Southgate, E., Thomson, J. N. & Brenner, S. The structure of the nervous system of the nematode Caenorhabditis elegans. *Philos Trans R Soc Lond B Biol Sci* **314**, 1-340 (1986).

18 Chalfie, M. & Sulston, J. Developmental genetics of the mechanosensory neurons of Caenorhabditis elegans. *Developmental biology* **82**, 358-370 (1981).

19 Chalfie, M. *et al.* The neural circuit for touch sensitivity in Caenorhabditis elegans. *The Journal of neuroscience* **5**, 956-964 (1985).

20 Kenyon, C., Chang, J., Gensch, E., Rudner, A. & Tabtiang, R. A C. elegans mutant that lives twice as long as wild type. *Nature* **366**, 461-464 (1993).

21 Bishop, N. A. & Guarente, L. Genetic links between diet and lifespan: shared mechanisms from yeast to humans. *Nature Reviews Genetics* **8**, 835-844 (2007).

22 Lai, C.-H., Chou, C.-Y., Ch'ang, L.-Y., Liu, C.-S. & Lin, W.-c. Identification of novel human genes evolutionarily conserved in Caenorhabditis elegans by comparative proteomics. *Genome research* **10**, 703-713 (2000).

23 Bishop, N. A. & Guarente, L. Two neurons mediate diet-restriction-induced longevity in C. elegans. *Nature* **447**, 545-549 (2007).

24 Gems, D. & Partridge, L. Stress-response hormesis and aging:"that which does not kill us makes us stronger". *Cell metabolism* **7**, 200-203 (2008).

25 Kirkwood, T. B. Understanding the odd science of aging. *Cell* **120**, 437-447 (2005).

26 Way, J. C. & Chalfie, M. The mec-3 gene of Caenorhabditis elegans requires its own product for maintained expression and is expressed in three neuronal cell types. *Genes & development* **3**, 1823-1833 (1989).

27 Suzuki, H. *et al.* In vivo imaging of C. elegans mechanosensory neurons demonstrates a specific role for the MEC-4 channel in the process of gentle touch sensation. *Neuron* **39**, 1005-1017 (2003).

28 Park, S.-J., Goodman, M. B. & Pruitt, B. L. Analysis of nematode mechanics by piezoresistive displacement clamp. *Proceedings of the National Academy of Sciences* **104**, 17376-17381 (2007).

29 Hansen, M. *et al.* A role for autophagy in the extension of lifespan by dietary restriction in C. elegans. *PLoS genet* **4**, e24 (2008).

30 Kuhara, A. *et al.* Temperature sensing by an olfactory neuron in a circuit controlling behavior of C. elegans. *Science* **320**, 803-807 (2008).

31 Anderson, J. R., Chiu, D. T., Wu, H., Schueller, O. & Whitesides, G. M. Fabrication of microfluidic systems in poly (dimethylsiloxane). *Electrophoresis* **21**, 27-40 (2000).

32 Whitesides, G. M. The origins and the future of microfluidics. *Nature* **442**, 368-373 (2006).

33 Duffy, D. C., McDonald, J. C., Schueller, O. J. & Whitesides, G. M. Rapid prototyping of microfluidic systems in poly (dimethylsiloxane). *Analytical chemistry* **70**, 4974-4984 (1998).

34 McDonald, J. C. & Whitesides, G. M. Poly (dimethylsiloxane) as a material for fabricating microfluidic devices. *Accounts of chemical research* **35**, 491-499 (2002).

35 Chung, K., Crane, M. M. & Lu, H. Automated on-chip rapid microscopy, phenotyping and sorting of C. elegans. *Nat Methods* **5**, 637-643, doi:10.1038/nmeth.1227 (2008).

36 Albrecht, D. R. & Bargmann, C. I. High-content behavioral analysis of Caenorhabditis elegans in precise spatiotemporal chemical environments. *Nature methods* **8**, 599-605 (2011).

37 Chronis, N., Zimmer, M. & Bargmann, C. I. Microfluidics for in vivo imaging of neuronal and behavioral activity in Caenorhabditis elegans. *Nature methods* **4**, 727-731 (2007).

38 Larsch, J., Ventimiglia, D., Bargmann, C. I. & Albrecht, D. R. High-throughput imaging of neuronal activity in Caenorhabditis elegans. *Proceedings of the National Academy of Sciences of the United States of America* **110**, E4266-4273, doi:10.1073/pnas.1318325110 (2013).

39 Schrödel, T., Prevedel, R., Aumayr, K., Zimmer, M. & Vaziri, A. Brain-wide 3D imaging of neuronal activity in Caenorhabditis elegans with sculpted light. *Nature methods* **10**, 1013-1020, doi:10.1038/nmeth.2637 (2013).

40 San-Miguel, A. & Lu, H. Microfluidics as a tool for C. elegans research. *WormBook*, 1-19, doi:10.1895/wormbook.1.162.1 (2013).

41 Ben-Yakar, A., Chronis, N. & Lu, H. Microfluidics for the analysis of behavior, nerve regeneration, and neural cell biology in C. elegans. *Current opinion in neurobiology* **19**, 561-567 (2009).

42 Crane, M. M., Chung, K., Stirman, J. & Lu, H. Microfluidics-enabled phenotyping, imaging, and screening of multicellular organisms. *Lab on a Chip* **10**, 1509-1517 (2010).

43 Chalasani, S. H. *et al.* Dissecting a circuit for olfactory behaviour in Caenorhabditis elegans. **450**, doi:10.1038/nature06292 (2007).

44 Chronis, N., Zimmer, M. & Bargmann, C. I. Microfluidics for in vivo imaging of neuronal and behavioral activity in Caenorhabditis elegans. **4**, 727-731, doi:10.1038/NMETH1075 (2007).

45 Crane, M. M., Chung, K. & Lu, H. Computer-enhanced high-throughput genetic screens of C. elegans in a microfluidic system. *Lab on a Chip* **9**, 38-40 (2009).

46 Hulme, S. E. *et al.* Lifespan-on-a-chip: microfluidic chambers for performing lifelong observation of C. elegans. *Lab on a Chip* **10**, 589-597 (2010).

47 Krajniak, J. & Lu, H. Long-term high-resolution imaging and culture of C. elegans in chip-gel hybrid microfluidic device for developmental studies. *Lab on a Chip* **10**, 1862-1868 (2010).

48 Yu, C.-C. J., Raizen, D. M. & Fang-Yen, C. Multi-well imaging of development and behavior in Caenorhabditis elegans. *Journal of neuroscience methods* **223**, 35-39 (2014).

49 Stroustrup, N. *et al.* the Caenorhabditis elegans lifespan machine. *Nature methods* **10**, 665-670 (2013).

50 Pincus, Z., Smith-Vikos, T. & Slack, F. J. MicroRNA predictors of longevity in Caenorhabditis elegans. *PLoS Genet* **7**, e1002306 (2011).

51 Xian, B. *et al.* WormFarm: a quantitative control and measurement device toward automated Caenorhabditis elegans aging analysis. *Aging cell* **12**, 398-409 (2013).

52 Crane, M. M., Chung, K. & Lu, H. Computer-enhanced high-throughput genetic screens of C. elegans in a microfluidic system. *Lab Chip* **9**, 38-40 (2009).

53 Chokshi, T. V., Bazopoulou, D. & Chronis, N. An automated microfluidic platform for calcium imaging of chemosensory neurons in Caenorhabditis elegans. *Lab on a Chip* **10**, 2758-2763 (2010).

54 Crane, M. M. *et al.* Autonomous screening of C. elegans identifies genes implicated in synaptogenesis. *Nature methods* **9**, 977-980 (2012).

55 Cho, Y., Zhao, C. L. & Lu, H. Trends in high-throughput and functional neuroimaging in Caenorhabditis elegans. *Wiley Interdisciplinary Reviews: Systems Biology and Medicine* (2017).

56 Otsu, N. A threshold selection method from gray-level histograms. *Automatica* **11**, 23-27 (1975).

57 Wardill, T. J. *et al.* A neuron-based screening platform for optimizing genetically-encoded calcium indicators. *PLoS One* **8**, e77728, doi:10.1371/journal.pone.0077728 (2013).

58 Swierczek, N. A., Giles, A. C., Rankin, C. H. & Kerr, R. A. High-throughput behavioral analysis in C. elegans. *Nat Methods* **8**, 592-598, doi:10.1038/nmeth.1625 (2011).

59 Venkatachalam, V. *et al.* Pan-neuronal imaging in roaming Caenorhabditis elegans. *Proceedings of the National Academy of Sciences of the United States of America*, 201507109, doi:10.1073/pnas.1507109113 (2015).

60 Crane, M. M. *et al.* Autonomous screening of C. elegans identifies genes implicated in synaptogenesis. *Nat Methods* **9**, 977-980, doi:10.1038/nmeth.2141 (2012).

61 Zhan, M. *et al.* Automated Processing of Imaging Data through Multi-tiered Classification of Biological Structures Illustrated Using Caenorhabditis elegans. *PLoS Comput Biol* **11**, e1004194, doi:10.1371/journal.pcbi.1004194 (2015).

62 Santella, A., Du, Z., Nowotschin, S., Hadjantonakis, A. K. & Bao, Z. A hybrid blob-slice model for accurate and efficient detection of fluorescence labeled nuclei in 3D. *BMC Bioinformatics* **11**, 580, doi:10.1186/1471-2105-11-580 (2010).

63 Qu, L. *et al.* Simultaneous recognition and segmentation of cells: application in C.elegans. *Bioinformatics* **27**, 2895-2902, doi:10.1093/bioinformatics/btr480 (2011).

64 Nicolson, T. The genetics of hearing and balance in zebrafish. *Annu. Rev. Genet.* **39**, 9-22 (2005).

65 Lumpkin, E. A. & Caterina, M. J. Mechanisms of sensory transduction in the skin. *Nature* **445**, 858-865 (2007).

66 Chalfie, M. & Au, M. Genetic control of differentiation of the Caenorhabditis elegans touch receptor neurons. *Science* **243**, 1027-1033 (1989).

67 Huang, M. & Chalfie, M. Gene interactions affecting mechanosensory transduction in Caenorhabditis elegans. *Nature* **367**, 467-470 (1994).

68 Delmas, P. & Coste, B. Mechano-gated ion channels in sensory systems. *Cell* **155**, 278-284 (2013).

69 Sulston, J., Dew, M. & Brenner, S. Dopaminergic neurons in the nematode Caenorhabditis elegans. *Journal of Comparative Neurology* **163**, 215-226 (1975).

70 Eastwood, A. L. *et al.* Tissue mechanics govern the rapidly adapting and symmetrical response to touch. *Proceedings of the National Academy of Sciences* **112**, E6955-E6963 (2015).

71 San-Miguel, A. & Lu, H. Microfluidics as a tool for C. elegans research. (2005).

72 Ryu, W. S. & Samuel, A. D. Thermotaxis in Caenorhabditis elegans analyzed by measuring responses to defined thermal stimuli. *The Journal of neuroscience* **22**, 5727-5733 (2002).

73 Chalasani, S. H. *et al.* Dissecting a circuit for olfactory behaviour in Caenorhabditis elegans. *Nature* **450**, 63-70 (2007).

74 Guo, Z. V., Hart, A. C. & Ramanathan, S. Optical interrogation of neural circuits in Caenorhabditis elegans. *Nature methods* **6**, 891-896 (2009).

75 Macosko, E. Z. *et al.* A hub-and-spoke circuit drives pheromone attraction and social behaviour in C. elegans. *Nature* **458**, 1171-1175 (2009).

76 Ha, H.-i. *et al.* Functional organization of a neural network for aversive olfactory learning in Caenorhabditis elegans. *Neuron* **68**, 1173-1186 (2010).

77 Kato, S., Xu, Y., Cho, C. E., Abbott, L. & Bargmann, C. I. Temporal responses of C. elegans chemosensory neurons are preserved in behavioral dynamics. *Neuron* **81**, 616-628 (2014).

78 Luo, L. *et al.* Dynamic encoding of perception, memory, and movement in a C. elegans chemotaxis circuit. *Neuron* **82**, 1115-1128 (2014).

79 Brenner, S. The genetics of Caenorhabditis elegans. *Genetics* **77**, 71-94 (1974).

80 Frøkjær-Jensen, C. *et al.* Single-copy insertion of transgenes in Caenorhabditis elegans. *Nature genetics* **40**, 1375-1383 (2008).

81 del Campo, A. & Greiner, C. SU-8: a photoresist for high-aspect-ratio and 3D submicron lithography. *Journal of Micromechanics and Microengineering* **17**, R81 (2007).

82 Unger, M. A., Chou, H.-P., Thorsen, T., Scherer, A. & Quake, S. R. Monolithic microfabricated valves and pumps by multilayer soft lithography. *Science* **288**, 113-116 (2000).

83 Stirman, J. N. *et al.* Real-time multimodal optical control of neurons and muscles in freely behaving Caenorhabditis elegans. *Nature methods* **8**, 153-158 (2011).

84 Chen, T.-W. *et al.* Ultrasensitive fluorescent proteins for imaging neuronal activity. *Nature* **499**, 295-300 (2013).

85 Li, W., Kang, L., Piggott, B. J., Feng, Z. & Xu, X. S. The neural circuits and sensory channels mediating harsh touch sensation in C. elegans. *Nature communications* **2**, 315 (2011).

86 Leifer, A. M., Fang-Yen, C., Gershow, M., Alkema, M. J. & Samuel, A. D. Optogenetic manipulation of neural activity in freely moving Caenorhabditis elegans. *Nature methods* **8**, 147-152 (2011).

87 Hilliard, M. A., Bargmann, C. I. & Bazzicalupo, P. C. elegans responds to chemical repellents by integrating sensory inputs from the head and the tail. *Current Biology* **12**, 730-734 (2002).

88 Wicks, S. R. & Rankin, C. H. Integration of mechanosensory stimuli in Caenorhabditis elegans. *The Journal of neuroscience* **15**, 2434-2444 (1995).

89 Chung, K., Crane, M. M. & Lu, H. Automated on-chip rapid microscopy, phenotyping and sorting of C. elegans. *Nature methods* **5**, 637-643 (2008).

90 Gordus, A., Pokala, N., Levy, S., Flavell, S. W. & Bargmann, C. I. Feedback from network states generates variability in a probabilistic olfactory circuit. *Cell* **161**, 215-227 (2015).

91 Boyden, E. S., Zhang, F., Bamberg, E., Nagel, G. & Deisseroth, K. Millisecond-timescale, genetically targeted optical control of neural activity. *Nature neuroscience* **8**, 1263-1268 (2005).

92 Zhang, F. *et al.* Multimodal fast optical interrogation of neural circuitry. *Nature* **446**, 633-639 (2007).

93 Airan, R. D., Thompson, K. R., Fenno, L. E., Bernstein, H. & Deisseroth, K. Temporally precise in vivo control of intracellular signalling. *Nature* **458**, 1025-1029 (2009).

94 Deisseroth, K. Optogenetics. *Nature Methods* **8**, 26-29, doi:10.1038/nmeth.f.324 (2011).

95 Larsch, J. *et al.* A Circuit for Gradient Climbing in C. elegans Chemotaxis. *Cell Rep* **12**, 1748-1760 (2015).

96 Raizen, D. M. *et al.* Lethargus is a Caenorhabditis elegans sleep-like state. *Nature* **451**, 569-572 (2008).

97 Van Buskirk, C. & Sternberg, P. W. Epidermal growth factor signaling induces behavioral quiescence in Caenorhabditis elegans. *Nature neuroscience* **10**, 1300-1307 (2007).

98 Cho, J. Y. & Sternberg, P. W. Multilevel modulation of a sensory motor circuit during C. elegans sleep and arousal. *Cell* **156**, 249-260 (2014).

99 Hope, I. A. *C. elegans: a practical approach*. Vol. 213 (OUP Oxford, 1999).

100 Ochsner, M. *et al.* Micro-well arrays for 3D shape control and high resolution analysis of single cells. *Lab on a Chip* **7**, 1074-1077 (2007).

101 Nekimken, A. L. *et al.* Pneumatic stimulation of C. elegans mechanoreceptor neurons in a microfluidic trap. *Lab on a Chip* (2017).

102 Schwarz, J., Lewandrowski, I. & Bringmann, H. Reduced activity of a sensory neuron during a sleep-like state in Caenorhabditis elegans. *Current Biology* **21**, R983-R984 (2011).

103 Blüher, M., Kahn, B. B. & Kahn, C. R. Extended longevity in mice lacking the insulin receptor in adipose tissue. *Science* **299**, 572-574 (2003).

104 Clancy, D. J. *et al.* Extension of life-span by loss of CHICO, a Drosophila insulin receptor substrate protein. *Science* **292**, 104-106 (2001).

105 Tatar, M. *et al.* A mutant Drosophila insulin receptor homolog that extends life-span and impairs neuroendocrine function. *Science* **292**, 107-110 (2001).

106 Holzenberger, M. *et al.* IGF-1 receptor regulates lifespan and resistance to oxidative stress in mice. *Nature* **421**, 182-187 (2003).

107 Colman, R. J. *et al.* Caloric restriction delays disease onset and mortality in rhesus monkeys. *Science* **325**, 201-204 (2009).

108 Greer, E. L. & Brunet, A. Different dietary restriction regimens extend lifespan by both independent and overlapping genetic pathways in C. elegans. *Aging cell* **8**, 113-127 (2009).

109 Grandison, R. C., Piper, M. D. & Partridge, L. Amino-acid imbalance explains extension of lifespan by dietary restriction in Drosophila. *Nature* **462**, 1061-1064 (2009).

110 Clancy, D. J., Gems, D., Hafen, E., Leevers, S. J. & Partridge, L. Dietary restriction in long-lived dwarf flies. *Science* **296**, 319-319 (2002).

111 Mair, W. & Dillin, A. Aging and survival: the genetics of life span extension by dietary restriction. *Annu. Rev. Biochem.* **77**, 727-754 (2008).

112 Weindruch, R., Walford, R. L., Fligiel, S. & Guthrie, D. The retardation of aging in mice by dietary restriction: longevity, cancer, immunity and lifetime energy intake. *J Nutr* **116**, 641-654 (1986).

113 Zhang, Y. & Mair, W. B. in *Ageing: Lessons from C. elegans* 355-391 (Springer, 2017).

114 Harrison, D. E. *et al.* Rapamycin fed late in life extends lifespan in genetically heterogeneous mice. *nature* **460**, 392-395 (2009).

115 Arey, R. N. & Murphy, C. T. Conserved regulators of cognitive aging: From worms to humans. *Behavioural Brain Research* (2016).

116 Masoro, E. J. Overview of caloric restriction and ageing. *Mechanisms of ageing and development* **126**, 913-922 (2005).

117 Stroustrup, N. *et al.* The temporal scaling of Caenorhabditis elegans ageing. *Nature* (2016).

118 Chung, K. *et al.* Microfluidic chamber arrays for whole-organism behavior-based chemical screening. *Lab on a Chip* **11**, 3689-3697 (2011).

119 Zhan, M. *New toolsets to understand environmental sensation and variability in the aging process*, Georgia Institute of Technology, (2014).

120 Rich, J. T. *et al.* A practical guide to understanding Kaplan-Meier curves. *Otolaryngology-Head and Neck Surgery* **143**, 331-336 (2010).

121 Goel, M., Khanna, P. & Kishore, J. Understanding survival analysis: Kaplan-Meier estimate. *International journal of Ayurveda research* **1**, 274 (2010).

122 Lithgow, G. J. & Walker, G. A. Stress resistance as a determinate of C. elegans lifespan. *Mechanisms of ageing and development* **123**, 765-771 (2002).

123 Korta, J., Clark, D. A., Gabel, C. V., Mahadevan, L. & Samuel, A. D. Mechanosensation and mechanical load modulate the locomotory gait of swimming C. elegans. *Journal of Experimental Biology* **210**, 2383-2389 (2007).

124 Cronin, C. J. *et al.* An automated system for measuring parameters of nematode sinusoidal movement. *BMC genetics* **6**, 5 (2005).

125 Restif, C. *et al.* CeleST: computer vision software for quantitative analysis of C. elegans swim behavior reveals novel features of locomotion. *PLoS Comput Biol* **10**, e1003702 (2014).

126 Pierce-Shimomura, J. T. *et al.* Genetic analysis of crawling and swimming locomotory patterns in C. elegans. *Proceedings of the National Academy of Sciences* **105**, 20982-20987 (2008).

127 Gatos, B., Pratikakis, I. & Perantonis, S. J. Adaptive degraded document image binarization. *Pattern recognition* **39**, 317-327 (2006).

128 Sauvola, J. & Pietikäinen, M. Adaptive document image binarization. *Pattern recognition* **33**, 225-236 (2000).

129 Stephens, G. J., Johnson-Kerner, B., Bialek, W. & Ryu, W. S. Dimensionality and dynamics in the behavior of C. elegans. *PLoS Comput Biol* **4**, e1000028 (2008).

130 Huang, C., Xiong, C. & Kornfeld, K. Measurements of age-related changes of physiological processes that predict lifespan of Caenorhabditis elegans. *Proceedings of the National Academy of Sciences of the United States of America* **101**, 8084-8089 (2004).

131 Bansal, A., Zhu, L. J., Yen, K. & Tissenbaum, H. A. Uncoupling lifespan and healthspan in Caenorhabditis elegans longevity mutants. *Proceedings of the National Academy of Sciences* **112**, E277-E286 (2015).

132 Herndon, L. A. *et al.* Stochastic and genetic factors influence tissue-specific decline in ageing C. elegans. *Nature* **419**, 808-814 (2002).

133 Gibbons, J. D. & Chakraborti, S. *Nonparametric statistical inference*. (Springer, 2011).

134 Glenn, C. F. *et al.* Behavioral deficits during early stages of aging in Caenorhabditis elegans result from locomotory deficits possibly linked to muscle frailty. *The Journals of Gerontology Series A: Biological Sciences and Medical Sciences* **59**, 1251-1260 (2004).

135 Murakami, H., Bessinger, K., Hellmann, J. & Murakami, S. Aging-dependent and-independent modulation of associative learning behavior by insulin/insulin-like growth factor-1 signal in Caenorhabditis elegans. *Journal of Neuroscience* **25**, 10894-10904 (2005).

136 Fang-Yen, C. *et al.* Biomechanical analysis of gait adaptation in the nematode Caenorhabditis elegans. *Proceedings of the National Academy of Sciences* **107**, 20323-20328 (2010).

137 Nguyen, J. P. *et al.* Whole-brain calcium imaging with cellular resolution in freely behaving Caenorhabditis elegans. *Proceedings of the National Academy of Sciences* **113**, E1074-E1081 (2016).

138 Prevedel, R. *et al.* Simultaneous whole-animal 3D imaging of neuronal activity using light-field microscopy. *Nat Methods* **11**, 727-730, doi:10.1038/nmeth.2964 (2014).

139 Kato, S. *et al.* Global Brain Dynamics Embed the Motor Command Sequence of Caenorhabditis elegans. *Cell*, 656-669, doi:10.1016/j.cell.2015.09.034 (2015).

140 Nguyen, J. P. *et al.* Whole-brain calcium imaging with cellular resolution in freely behaving Caenorhabditis elegans. *Proceedings of the National Academy of Sciences of the United States of America*, 33, doi:10.1073/pnas.1507110112 (2015).